

Morphology and dynamics of the Venus atmosphere at the cloud top level as observed by the Venus Monitoring Camera

Von der Fakultät für Elektrotechnik, Informationstechnik, Physik
der Technischen Universität Carolo-Wilhelmina
zu Braunschweig
zur Erlangung des Grades eines
Doktors der Naturwissenschaften
(Dr.rer.nat.)
genehmigte
Dissertation

von Richard Moissl
aus Grünstadt

Bibliografische Information Der Deutschen Bibliothek

Die Deutsche Bibliothek verzeichnet diese Publikation in der Deutschen Nationalbibliografie; detaillierte bibliografische Daten sind im Internet über <http://dnb.ddb.de> abrufbar.

1. Referentin oder Referent: Prof. Dr. Jürgen Blum

2. Referentin oder Referent: Dr. Horst-Uwe Keller

eingereicht am: 24. April 2008

mündliche Prüfung (Disputation) am: 9. Juli 2008

ISBN 978-3-936586-86-2

Copernicus Publications, Katlenburg-Lindau

Druck: Schaltungsdienst Lange, Berlin

Printed in Germany

Contents

Summary	7
1 Introduction	9
1.1 Historical observations of Venus	9
1.2 The atmosphere and climate of Venus	9
1.2.1 Basic composition and structure of the Venus atmosphere	9
1.2.2 The clouds of Venus	11
1.2.3 Atmospheric dynamics at the cloud level	12
1.3 Venus Express	16
1.4 Goals and structure of the thesis	19
2 The Venus Monitoring Camera experiment	21
2.1 Scientific objectives of the VMC in the context of this thesis	21
2.1.1 UV Channel	21
2.1.1.1 Morphology of the unknown UV absorber	21
2.1.1.2 Atmospheric dynamics of the cloud tops	21
2.1.2 The two IR channels	22
2.1.2.1 Water vapor abundance and cloud opacity	22
2.1.2.2 Surface and lower atmosphere	22
2.1.3 Visible channel	23
2.2 The Camera	23
2.2.1 Hardware	23
2.2.2 Software Architecture of the VMC	25
2.2.3 The SingleImage routine	26
2.3 Observations and Planning	28
2.3.1 Artifacts in VMC images and removal procedure	30
2.4 The dataset	32
2.4.1 Statistics	32
2.4.2 Data description	32
3 Results	37
3.1 Cloud top Morphology	37
3.1.1 Overview	37
3.1.2 Cloud morphology from VMC images	39
3.1.2.1 Apocentric observations of the south polar region	39
3.1.2.2 Off-pericenter observations of the southern hemisphere	46

3.1.2.3	Pericenter observations of the northern hemisphere . . .	48
3.2	Dynamics	60
3.2.1	Tracking methods	61
3.2.2	The dataset of wind vectors derived from wind tracking	65
3.2.3	Comparison of results from different methods	67
3.2.4	Error sources and systematic uncertainties	69
3.2.5	Averaged Zonal wind profiles	70
3.2.6	Temporal variability of Zonal wind profiles	72
3.2.7	Local solar time dependency of the Zonal wind field	77
3.2.8	Meridional wind component	80
4	Discussion and Outlook	83
4.1	Morphology	83
4.2	Dynamics	85
A	Artifacts in VMC images (extended)	91
A.1	Dark UV strip	91
A.2	Filament-spot patterns	93
B	Cyclostrophic Balance and cyclostrophic winds	97
	Bibliography	99
	Publications	107
	Acknowledgements	109
	Curriculum Vitae	111

Summary

The upper clouds of Venus have been studied extensively from ground and space borne observations in the past, especially in the ultraviolet part of the spectrum. To date we know that the atmosphere of Venus is in a constant state of super-rotation, reaching speeds around 100 ms^{-1} at the cloud tops and that the cloud markings in the UV are caused by SO_2 and another, yet unknown, UV absorber.

This thesis deals mainly with the observations of the Venus cloud deck at an approximate altitude of 65-70 km above the surface in the UV channel (centered at 365 nm wavelength) of the Venus Monitoring Camera experiment (VMC) on board the European Venus Express mission. One focus of the studies presented here is to improve the knowledge of the spatial and temporal variability of the unknown UV absorber. The other main objective is to learn more about the atmospheric dynamics at the cloud top level inferred from tracking UV cloud markings. The highly elliptical polar orbit of Venus Express allows for observations of the southern hemisphere in nadir perspective, complementing observations from earlier missions like Mariner 10, Pioneer Venus and Galileo. In addition, the VMC was able to acquire image data with high spatial and temporal resolution, thus combining the global observation of the southern hemisphere with close-up insights on morphologic features.

A number of technical preparations have been necessary in order to be able to acquire the data needed for these studies. Those included programming the imaging software for the VMC, planning observation sequences and correcting the VMC images for artifacts. Furthermore high-precision navigation software has been developed and existing software tools have been adapted to conduct manual and automatic tracking of cloud features in the VMC images.

Results on morphology include the identification of all known morphological features, as well as identification of substructures therein and previously undetected small scale phenomena, such as small scale gravity waves in high northern latitudes. Further, cloud features indicative of vigorous convective activity in the equatorial region have been identified on unprecedentedly small scales, likely resolving an ongoing discussion about the dynamics of convection in the sub-solar region of the Venus atmosphere. The VMC long-term observations of the southern hemisphere provided an extensive data set on the highly variable appearance and dynamics of the south polar region, for the first time in the history of the observations of Venus, on a global as well as on intermediate scales.

In addition to the confirmation of results from previous studies on the atmospheric dynamics, the long term observations of the southern hemisphere by the VMC allowed for detailed studies of the strong cloud-level super-rotation phenomenon on Venus and its variability on different timescales ranging from hours to several months. Information on the latitudinal wind speed profiles could be obtained for latitudes up to $\sim 85^\circ \text{ S}$, extending

the results from previous studies by almost 20°. Global wave modes which are believed to play a key role for understanding energy transport phenomena in the venusian atmosphere, such as a 4-day Kelvin wave mode in low latitudes and diurnal and semidiurnal solar thermal tides have been detected in the analysis of the cloud tracked global wind fields.

The conducted studies, based on the data acquired in the course of the primary mission of Venus Express, helped to improve ongoing and future observation sequences in order to derive higher accuracy wind fields which will help to gradually refine the information on atmospheric dynamics at cloud level. In 2011 the VMC observations will be conducted in concert with imaging experiments on board the japanese Venus Climate Orbiter, providing a valuable opportunity to study the morphology and dynamics of the upper cloud region simultaneously from two spacecrafts and in two different complementary observation geometries.

1 Introduction

1.1 Historical observations of Venus

Ever since prehistoric times, our next neighbor planet (orbiting the sun at ~ 0.7 AU) has attracted the curiosity of humankind and stirred our imagination. Often mistaking Venus for two different entities, morning and evening star, most of the early civilizations have included the third brightest celestial object (maximum brightness -4.6 magnitudes) into their mythologies. Not few of them attributed beauty and grace to the brilliant “star”. For a long time its movement and appearance were observed and followed by sages and priests, records dating back at least to the Babylonians around 3000 B.C. (Huber 1977).

The first scientific result on Venus was achieved by Galileo Galilei in 1610 when he discovered the phases of Venus and deduced that the planet is therefore not self-luminous and orbiting the sun (“*Cynthiae figuras aemulatur mater amorum*” (Galilei 1610), translated: “The mother of loves emulates the figure of Cynthia [the Moon]”). Following observations during the seventeenth and eighteenth century confirmed the phases. Probably the first report on features on the nearly blank face of Venus (in visible light) came from Francesco Fontana, when he claimed to have observed dusky spots on the illuminated disc in 1645. Although the existence of those spots remained disputed for a long time, more observers confirmed sightings of them, including Giovanni Domenico Cassini among others. Other observers, such as E. E. Barnard for example, were never fully convinced of their reality. In 1726 Francesco Bianchini even (erroneously) concluded a rotation period of 24 hours for Venus from these markings. Finally in the late 1920’s Wright (1927) and Ross (1928) recorded markings on Venus on photographs in the ultraviolet which were evident to everyone. These UV markings have been extensively confirmed by subsequent observations and are frequently used for investigations on Venusian atmospheric dynamics until today. Also in this thesis they comprise the predominant observational basis for the presented data and results. For a far more detailed account on the development of studies on Venus I recommend the introductory chapter by Cruikshank (1983) in the “Venus” book.

1.2 The atmosphere and climate of Venus

1.2.1 Basic composition and structure of the Venus atmosphere

Although basically a twin of earth in terms of size, mass and density (see table 1.1), the slow and retrograde rotating Venus (sidereal rotation period: 243.7 days) developed dramatically different atmospheric conditions. The most apparent one of which is the

complete and uninterrupted cloud layer covering the whole planet. But also in other terms the Venus atmosphere is completely different from its counterpart on Earth.

While Earth’s atmosphere is composed mainly of nitrogen and oxygen, the atmosphere of our “twin sister” planet is mostly composed of CO₂ (~96.5 %) and some N₂ (~3.5 %). Other volatiles, like SO₂ (~150 ppm), Argon (~70 ppm) and water vapor (~20 ppm) are only present in trace amounts (values originate from the NASA Venus factsheet and represent near-surface atmospheric composition).

	Mass [10 ²⁴ · kg]	Volume [10 ¹⁰ · km ³]	Mean radius [km]	Mean density [kg · m ⁻³]	Solar irradiance [W · m ⁻²]	Bond albedo
Venus	4.869	92.843	6051.8	5243	2613.9	0.750
Earth	5.974	108.321	6371.0	5515	1367.6	0.306
Ratio	0.815	0.857	0.95	0.951	1.911	2.45

Table 1.1: Venus and Earth bulk parameters compared

A comparison between the theoretical black body temperatures of Venus (231.7 K) and Earth (254.3 K) as observed from space might, at a first glance, appear to be counterintuitive to the average surface temperature levels which are ~288 K on Earth and ~737 K on Venus. The differences between the black body temperature, neglecting atmospheric effects, and the actual surface temperature are caused by the so called greenhouse effect, which has become a well known term from the ongoing discussions about the anthropogenic-induced climate change on Earth. Only amounting to about 34° C on Earth, the main reasons for the greenhouse effect on Venus are the dense (~92 bars and 65kg/m⁻³ at surface level) CO₂ atmosphere, contributing about 420 K and the thick cloud layer (~140 K). It is still unknown how Venus originally developed this “runaway” greenhouse effect, but the answer is believed to be closely connected to the apparent loss of the planetary water inventory.

Figure 1.1 (left) shows a comparison between typical Venus, Earth and Mars temperature profiles. The most obvious differences are seen in the extreme temperatures on Venus, caused by the runaway greenhouse effect, below ~ 90 km altitude and in the thermosphere above 100 km altitude. There the nitrogen-oxygen atmosphere of Earth behaves vastly different from the CO₂ atmospheres of Mars and Venus. Another interesting detail is the peculiar night side profile of the Venus thermosphere, which is behaving so differently from the ones of Earth and Mars that it has been denominated with the term “cryosphere”.

A zonally averaged profile of the middle atmosphere of Venus (see fig. 1.1 (right)), obtained by Venera and Vega probes, shows that the temperatures along constant pressure level do increase from the equator to the pole. Due to the higher level of solar heating at the equator as compared to the poles, this structure leaves the middle atmosphere of Venus in a radiative equilibrium, requiring dynamical forcing to be sustained. At altitudes between 60-70 km, another interesting structure is observed in the high latitudes. Inside the so called “cold collar”, temperatures can be about 30° lower compared to its surroundings.

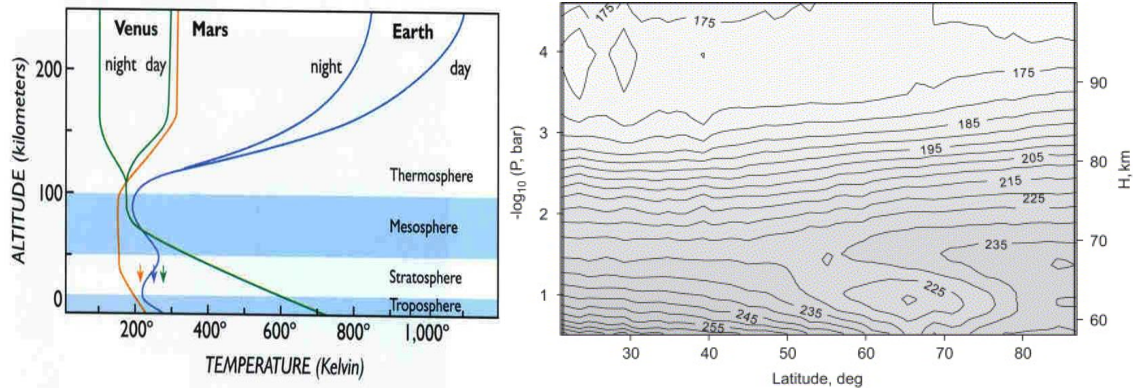
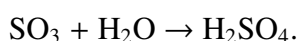
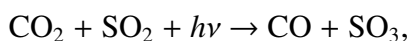


Figure 1.1: *Left*: Comparison of temperature profiles of the atmospheres of terrestrial planets. *Right*: Zonally averaged latitude versus altitude temperature field of the middle atmosphere of Venus (Zasova et al. 2007).

1.2.2 The clouds of Venus

The thick cloud layer that completely veils the planet extends from about 45 up to nearly 70 km above the surface of Venus. Haze layers are present above and below this main cloud layer (see figure 1.2 *left*). The regularly observed dark markings in the ultraviolet (UV) spectral range (see fig. 1.3, *left*) are caused in parts by sulfur dioxide (SO₂) but mainly by a still unidentified substance. The spectral cloud albedo (fig. 1.2, *right*) in the UV range shows that this unknown UV absorber must be responsible for the absorption in wavelengths longer than 320 nm, where SO₂ does not match the observed absorption behavior. Possible candidates for the second UV absorber include sulfur compounds or even allotropes of elemental sulfur. The UV bright regions of the clouds essentially consist of sulfuric acid. The UV patterns in the clouds are seen where optical depth in the UV approaches unity. This is the case at a pressure level of 40-50 mbar, corresponding to altitudes of 65-70 km Esposito et al. (1983).

Within the main cloud deck, particles of different sizes are found at different altitudes resulting in a layered substructure. Cloud particle sizes range from below 1 μm to more than 30 μm and basically show a trimodal size distribution. The smallest, micron and sub-micron sized droplets, called “mode 1” particles form an aerosol haze extending throughout most of the cloud layer and their composition is not known yet. The intermediate “mode 2” droplets have typical diameters around 2-3 μm. Spectroscopic, polarimetric and other evidence implies a composition of 75% H₂SO₄ and 25% H₂O. Formation of the sulfuric acid drops seems to occur through photochemical combination of H₂O and SO₂ near the cloud top level under participation of CO₂ via the reactions:



Most of the cloud mass is present in the biggest “mode 3” particles, which may be either evolved aggregates of sulphuric acid drops or another mode with a different, again unknown, composition. Indirect evidence from Pioneer Venus Large Probe data suggests a solid, possibly non-spherical, particle species which would rule out H₂O, H₂SO₄ and HCl

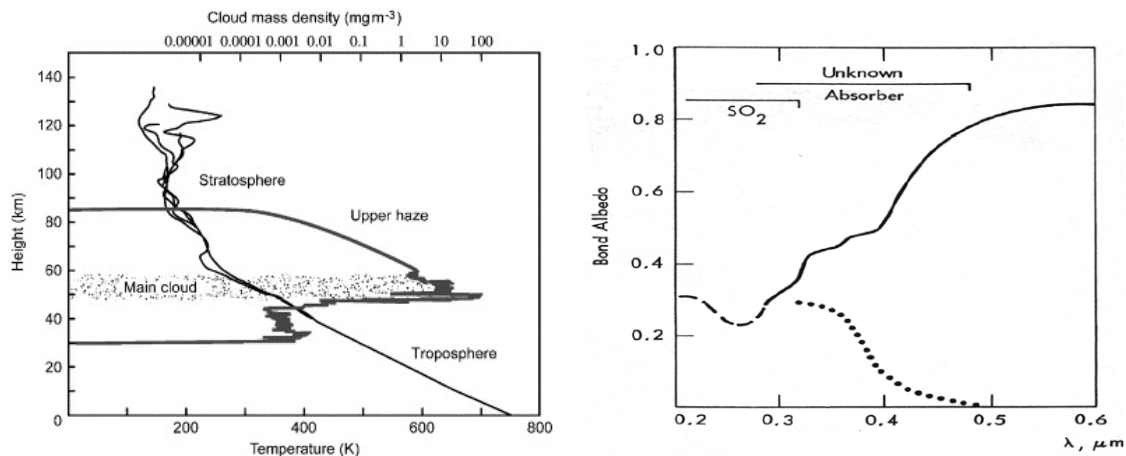


Figure 1.2: *Left*: Typical vertical temperature (black curves, bottom scale) and cloud density profiles (gray curve, top scale) in Venus atmosphere (from Taylor (2006b)). *Right*: Spectral cloud albedo in the UV range.

(which has also been identified within the clouds).

Despite the enormous thickness of the cloud deck, they are not completely impervious to all visible and IR parts of the light spectrum. Since the cloud droplets are quite efficient scatterers at these wavelengths, a relatively large fraction of sunlight permeates the atmosphere below the clouds. The Venera and Pioneer landers found that between 2.5% (Pioneer) and 3.5% (Veneras) of the total solar irradiation reaches the surface, providing illumination levels comparable to those during a thunderstorm on Earth (Moroz 2002).

Through several spectral “windows”, the hot surface and lower atmosphere of Venus, which emit strongly in the IR, can be observed from space. Observations by the Near-Infrared Mapping spectrometer on board the Galileo spacecraft (figure 1.3, *right*) showed large scale variations horizontal and vertical structures in the Venus cloud deck. These large scale structures, together with observed strong variations of minor species concentrations in and around the cloud level, indicate surprisingly active meteorological behavior in the deep atmosphere of Venus (Taylor 2006a,b).

Obviously, many open questions remain on the composition of the cloud deck. Among the most crucial ones are the search for the identity of the unknown UV absorber (and other chemical species) and the mechanisms behind its formation, chemical life-cycle and its (re-)distribution around the planet.

1.2.3 Atmospheric dynamics at the cloud level

Also in terms of atmospheric dynamics Venus is entirely different from Earth. A strong retrograde (westward) so called “super-rotation” of the atmosphere at cloud level has first been determined from ground based UV observations of the cloud deck in the 1960s by the continued reappearance of a prominent large scale feature resembling a dark horizontal **Y** shape (which has also been observed by space missions, see figure 1.3 *left*). From the approximate 4-day periodicity of this Y-shape, cloud level wind speeds around 100 ms⁻¹ had been determined (Boyer and Carmichel 1961, Boyer 1961, Smith 1967). Later UV observations from the Mariner 10 (Murray et al. 1974, Belton et al. 1976a,b), the Pioneer

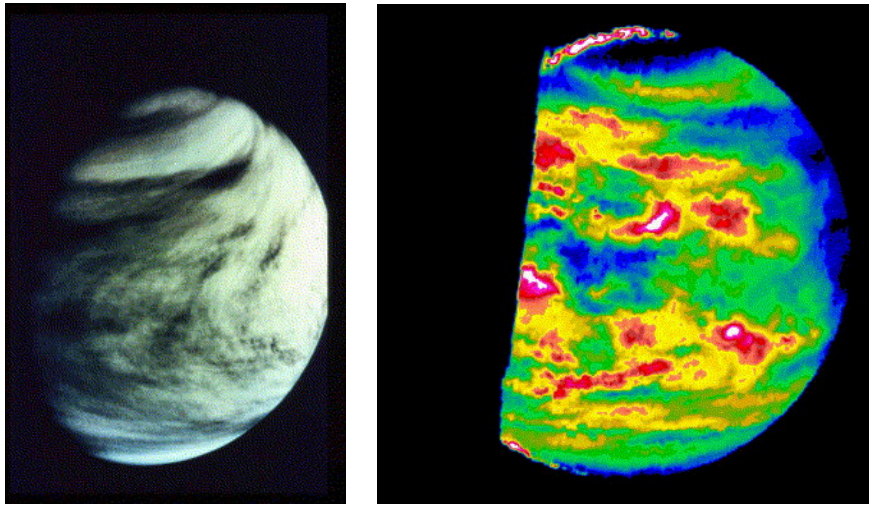


Figure 1.3: *Left:* Ultraviolet image of Venus from the Pioneer Orbiter (NASA), showing the typical sideways 'Y' shape that has been observed since the 1960s. *Right:* False color Infrared Image of the Venus night side at $2.3 \mu\text{m}$ obtained by the Galileo spacecraft during its flyby in 1990 (Carlson et al. 1991). The clouds are seen to be highly non uniform, causing strong brightness variations. White and red colors indicate thin cloud regions through which more heat is radiated from the hot surface below, black and blue values represent thicker clouds

Venus Orbiter (Travis et al. 1979, Rossow et al. 1980) and the Galileo (Belton et al. 1991, Toigo et al. 1994) spacecraft missions have enabled investigations on the properties of the global dynamics at cloud top level with much higher resolution and increased temporal coverage.

By tracking the movement of small cloud features, which are traveling at the ambient wind speeds, it was confirmed that indeed the bulk velocity of the atmosphere is in a continuous state of zonal (parallel to the equator) super-rotation. This means that the atmosphere is rotating about 50 times faster (at the cloud level) than the slowly rotating planet body below. In addition it was found that large scale structures like the Y-feature represent global scale waves, propagating upstream at about $20\text{-}30 \text{ ms}^{-1}$ (del Genio and Rossow 1990, Smith et al. 1992). Also thermal tides, induced by solar heating, with a surprisingly large semidiurnal component relative to the diurnal component have been identified (Limaye et al. 1982, Rossow et al. 1990). Schubert (1983) discusses several different suggestions for the maintenance of the super-rotation of the atmosphere, which include processes such as equatorward transport of angular momentum by eddies and angular momentum transport through the solar thermal tides. But to date no commonly accepted explanation has been found for the origin and maintenance of the super-rotation. Together with the runaway greenhouse effect and the nature of the unknown UV absorber it the third big mystery of the Venus atmosphere.

Other remarkable wave features on large scales are the so called "circumpolar belts" and the "bow-like waves" (Belton et al. 1976b, Rossow et al. 1980). The first term denotes very narrow (50 km) and elongated (thousands of km) bright bar-like features parallel to the equator which are only observed to be moving slowly (20 ms^{-1}) toward the south,

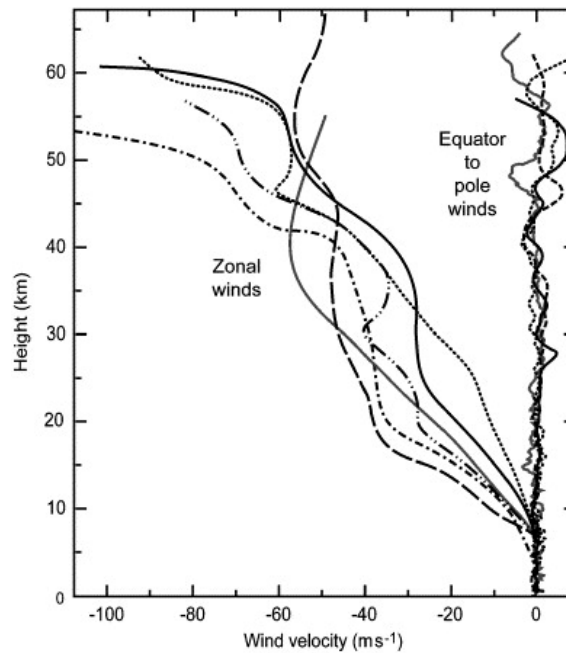


Figure 1.4: Venus wind profiles for zonal and meridional (equator to pole) winds.

regardless of hemisphere. The most likely explanation for the nature of these circum-polar belts is that they are a type of gravity waves. A gravity wave in this respect is a resonance caused in an atmosphere by density variations, propagating as waves under the influence of gravity as a restoring force (not to be confused with the relativistic effect of gravitational waves).

The bow-like (or bow-shaped) waves are believed to be caused by massive upwelling in the subsolar region (local noon at the equator, where solar heating is strongest) acting as a kind of obstacle for the zonal winds. Further indication for this upwelling in a subsolar disturbance are “cell-like” convective features which are mainly observed in the vicinity and downstream of the subsolar region (Belton et al. 1976b, Rossow et al. 1980).

The entry probes of the Veneras and Pioneer Venus provided further insight to the vertical wind structure, showing strong wind shear and variability at altitudes close to the cloud tops and decline to quasi constant values with height, down to few ms^{-1} in the lowest parts of the atmosphere (see figure 1.4) (Counselman et al. 1980).

Detailed wind tracking results over the whole day side of Venus show latitudinal dependences of the zonal super-rotation as well as a poleward migration of UV markings in both hemispheres. Latitudinal profiles of the zonal winds regularly exhibit strong jets with wind speeds in excess of 120 ms^{-1} in the mid latitude regions ($40\text{-}60^\circ$) which are in general agreement with the assumption of cyclostrophic balance in Venus’s atmosphere (see: Appendix B on page 97). With speeds of less than 10 ms^{-1} the poleward motions are much slower than the zonal winds but equally important in terms of the general circulation. This meridional (parallel to the meridians) flow betrays the existence of two gigantic hemispheric circulation cells in which air rises at the equator due to solar heating and descends again after radiative cooling in the near-polar region (Limaye 1985). On a slow rotating planet like Venus these so called “Hadley” cells (named after G. Hadley who proposed the mechanism in 1735) are not limited to the near-equatorial regions like

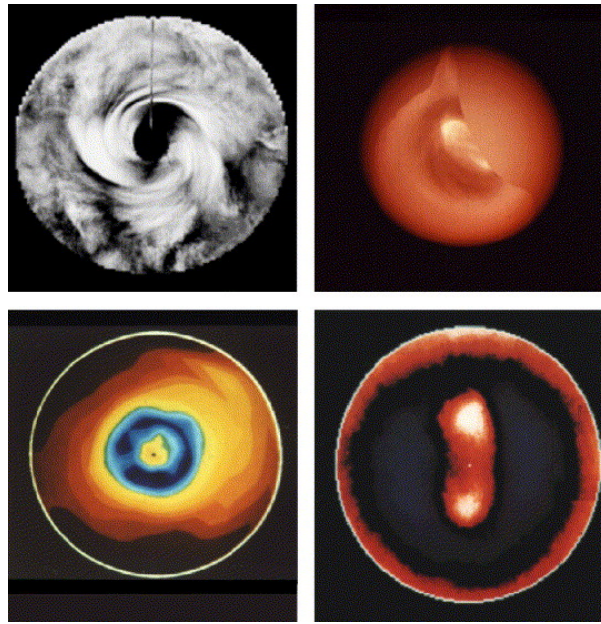


Figure 1.5: The north polar vortex in a composite of Pioneer Venus UV images (top left), dipole structure at $11.5 \mu\text{m}$ from Pioneer Venus Orbiter (Taylor et al. 1980) (top right), a 72-day average showing the cold collar structure (bottom left), and a similar average in a coordinate frame rotating every 2.7 days, showing the dipole structure (bottom right).

on Earth, where they break up due to the coriolis force due to the Earth's rotation.

The combination of the strong zonal and the weaker meridional flow explains the spiraling streaks seen in the UV images of Venus (Suomi 1975, Smith and Gierasch 1996) and is likely connected to an organization of the atmospheric circulation in two hemispheric vortices centered over both poles of Venus (Suomi and Limaye 1978, Limaye 2007). On closer examination the Hadley circulation appears not to spread completely to the poles. Instead the descending branches of the Hadley cells appear to coincide with the already mentioned cold collar structures detected by entry probes. In both hemispheres, numerous IR observations of the polar regions confirmed the presence of these currents of cold air, surrounding the poles at radial distances of about 2500 km (corresponding to latitudes around 75°). Temperatures inside these collars are about 30°C below the ones outside at corresponding altitudes. Such features would normally tend to dissipate rapidly due to the resulting pressure differences, indicating that they are being continually forced by a yet unknown mechanism.

The polar vortices, analogous to the eye of a terrestrial hurricane but at vastly larger scales, have also been observed to show a dipole-like shape in thermal observations in the past. Recent observations, however, have shown that the vortices are more often organized in the simpler shape of a single "vortex eye" (Lebonnois et al. 2006). These vortex eyes were reported to rotate about the poles with periods of about 2.7 (Earth) days, about twice as fast in angular velocity than the atmosphere at equatorial latitudes. Figure 1.5 shows images of the north polar vortex (in dipole shape), and cold collar. Figure 1.6 gives a synopsis sketch of the above described as well as other dynamic properties of the Venus atmosphere.

Among the great number of puzzles that are still to be solved about the atmospheric

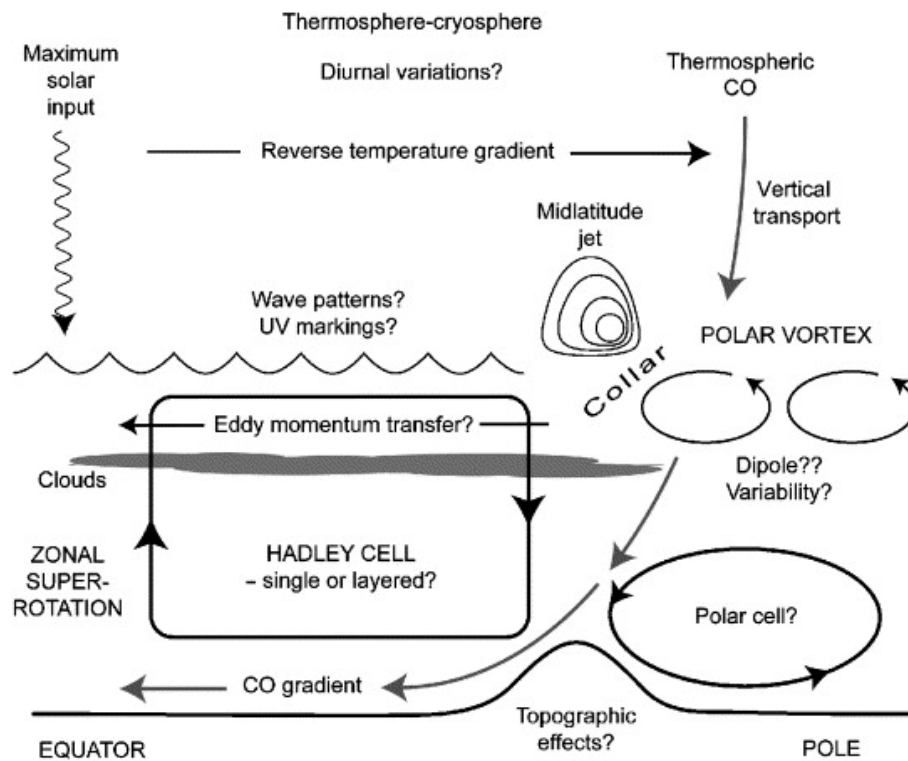


Figure 1.6: Summary of the main properties of the atmospheric circulation on Venus. Question marks denote some of the principle questions left to be answered. (Taylor 2006b)

dynamics of Venus, the key questions to the mysteries of this “Planet of Storms” are: Which processes are maintaining the strong super-rotation? Is the meridional circulation organized indeed in two deep hemispheric Hadley cells, or are there two or more Hadley layers on top of each other? Is there a second Hadley-type cell in the polar region? How does the polar vortex behave over time? How are the many gravity wave modes in the atmosphere produced and which role do they play in distributing kinetic energy around the planet?

1.3 Venus Express

The Venus Express (VEX) is the first European mission to Venus (Svedhem et al. 2007). Its main objectives are to investigate atmospheric composition, structure and dynamics as well as to study the plasma environment and the surface of Venus. Its scientific payload consists of seven instruments which are designed to follow these objectives. Most of the instrument designs, and also the spacecraft bus itself, are not specifically developed for Venus Express but are inherited from Mars Express and Rosetta missions.

The seven instruments are:

- **ASPERA** (Analyzer of Space Plasma and Energetic Atoms) which is investigating in situ plasma and neutral energetic atoms around the planet (Barabash et al. 2007).

- **MAG** (Magnetometer) conducting magnetic field measurements and supporting ASPERA (Zhang et al. 2006).
- **PFS** (Planetary Fourier Spectrometer) a high-resolution infrared fourier spectrometer which unfortunately is inoperable due to a mechanical defect (Formisano et al. 2006)
- **SPICAV/SOIR** (Spectroscopy for the Investigation of the Characteristics of the Atmosphere of Venus) a high-resolution UV and near-IR spectrometer for stellar and solar occultations and nadir observations studying mainly the vertical structure and composition of the Venus atmosphere. (Bertaux et al. 2006).
- **VeRa** (Venus Radio Science) a radio system with an ultra-stable oscillator (USO), investigating the fine structure of the atmosphere and ionosphere and also the surface. In addition VeRa is performing gravity anomaly experiments and sounding the solar corona (Häusler et al. 2006).
- **VIRTIS** (Visible and Infrared Thermal Imaging Spectrometer) an imaging and high-resolution spectrometer, operating from the visible through thermal infrared spectral range with a wide range of mission objectives from the higher atmosphere down to the surface (Drossart et al. 2007).
- **VMC** (Venus Monitoring Camera) a compact sized wide angle camera with channels in the UV, visible and infrared, investigating atmospheric dynamics, surface heat anomalies, O₂ nightglow and water vapor in the lower atmosphere (Markiewicz et al. 2007a).

Venus Express has been launched on 9th November 2005 from the the Baikonur Cosmodrome in Kazakhstan by a Sojuz-Fregat rocket. After a journey of only 153 days it arrived at Venus on 11. April 2006 and was inserted into a highly elliptical polar orbit about the planet. The apocenter distance is about 66,000 km, pericenter altitude ranges between 250-350 km altitude and the revolution period is 24 hours. The pericenter latitude was approximately 78° N at the beginning of the mission and is slowly drifting poleward. By convention, time in each orbit is counted starting from 0 h at pericenter but orbit numbers are increased in apocenter at 12 h.

The unusual orbit of Venus Express allows for observations highly complementary to those of earlier missions. With the apocenter above the south pole the VEX orbit gives a global view of the southern hemisphere of Venus, allowing for the first time to extensively study polar and global dynamics and morphology for extended and uninterrupted periods of time in each orbit. In addition, the close approach around pericenter delivers the possibility to combine close-up observation to global overviews, thus acquiring morphological and dynamical information on different orders of magnitudes.

From an operational point of view, the Venus Express orbit can roughly be divided in three different phases (see also figure 1.7): the pericenter observations between 23-2 h orbit time, telecommunications phase (2-12 h, in descending branch of the orbit) and the apocenter and so called “off-pericenter” operations (12-23 h, in ascending orbit branch). The science operations of Venus Express have been organized in ten “science cases”.

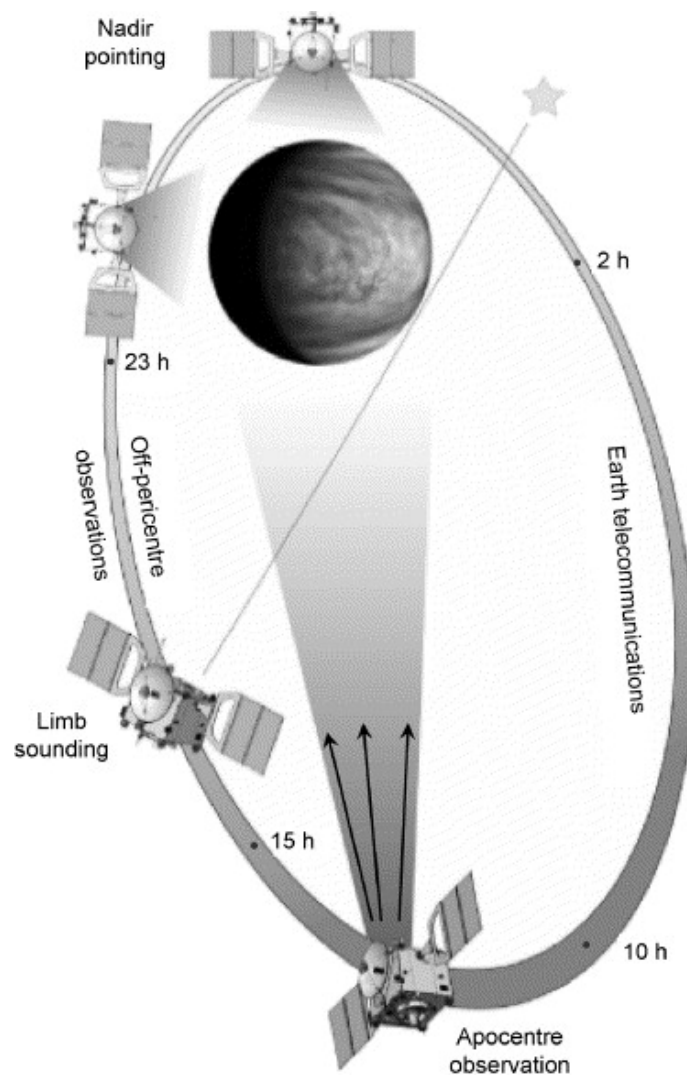


Figure 1.7: Overview of Venus Express orbit and typical operations conducted in different orbit sections.

Three of these science cases (numbered as science cases #1, #2 and #3) are equivalent to science operations conducted in the three observation periods with the +Z axis (and therefore most instruments) of the spacecraft pointing to local nadir on the planet. Main science goals during pericenter passages (case #1) are spectroscopic and imaging observations of the northern latitudes with medium to high spatial resolutions and plasma, as well as magnetic field measurements in the vicinity of the planet. In off-pericenter observations, (case #2) spectrometers and imaging instruments study the whole southern hemisphere, with emphasis on the atmospheric dynamics, while the plasma and magnetic field instruments conduct measurements in the solar wind interaction region. In apocenter observations (case #3), basically the same science goals are followed from a greater distance and with an emphasis on the south polar region dynamics.

Another set of five science cases is dedicated to observing the vertical structure of the atmosphere at the limbs of the planet (cases #4 to #8). In addition to a very general observation of the limbs by all optical instruments (case #7), two of these “limb type” ob-

servations include stellar (case #5) and solar (case #6) occultations by the SPICAV/SOIR instrument. The remaining two cases are dedicated to the bi-static radar sounding of surface properties (#4) and vertical atmospheric structure (#8) by VeRa. During the limb observations the spacecraft is either pointing into a fixed direction or performing customized slewing maneuvers.

The remaining two science cases are observations of the solar corona (case #9) in superior conjunction and investigations of gravity anomalies (case #10), both also conducted by the VeRa experiment.

A more detailed description of these cases, as well as a comprehensive overview of Venus Express science planning and operations is given in Titov et al. (2006).

1.4 Goals and structure of the thesis

The main scientific objectives within the scope of this thesis are to collect imaging data with the Venus Monitoring Camera (VMC) on board the Venus Express spacecraft over the course of the primary mission between May 2006 and March 2007 and analyze it with respect to unresolved questions about the atmospheric dynamics of the cloud top region of Venus. The data of the VMC instrument comprises the first spaceborne observations after more than a decade and is complementing and extending the data acquired by previous camera experiments on board the Mariner 10, Pioneer Venus and Galileo space probes. The tasks performed in pursuit of this work were in detail:

- **Scientific tasks**

- Studying the morphology of the Venus cloud top region on different scales in order to increase knowledge about the spatial and temporal distribution and behavior of the unknown UV absorber.
- Tracking of UV cloud patterns in order to study the dynamics of the Venus atmosphere at the cloud top level.
- Investigate the retrieved dynamical data from cloud tracking for spatial and temporal variability of the global super-rotation phenomenon, the meridional circulation in the southern hemisphere and search for global wave modes and solar thermal tides.
- Comparison of VMC data to results from earlier missions.

- **Technical tasks and preparations**

- Programming of image acquisition software for the VMC experiment.
- Planning and implementing VMC observations and imaging sequences in order to achieve a good spatial and temporal coverage of the Venus atmosphere on the day side as well as on the night side of the planet.
- Providing tables with information about image parameters and scientific objectives for archiving purposes.

- Removal of artifacts from the acquired images. Due to a prolonged accidental exposure of the VMC instrument to direct sun irradiation, the instrument suffered damage to the CCD-based detector which resulted in two types of artifact patterns.
- Programming of a tool for linking navigation data to images in order to enable high precision navigation for each pixel of the imaging detector.
- Adaption of existing software tools for tracking cloud features in dedicated VMC image sequences.

This document is organized as follows:

- This chapter is supposed to give a brief introduction to the atmosphere of Venus, focusing on the clouds and atmospheric dynamics in the upper cloud region.
- Chapter 2 describes the VMC experiment in some detail. It addresses the scientific objectives of the VMC as well as the most important aspects of the hardware and provide information about the software. Further, important aspects for the planning of the VMC image sequences are explained and an overview of the dataset acquired during the primary mission is given.
- Chapter 3 is split into two major sections. The first section presents the results of the investigations of cloud morphology. The second section gives a description and analysis of the employed cloud tracking methods, describes the data retrieved on atmospheric dynamics by cloud tracking and presents the results inferred on the cloud level motions in the atmosphere.
- Chapter 4 summarizes and discusses the results of this thesis and gives an outlook on possible and needed future work.
- Details of the investigation of the nature of the sun-induced damage to the VMC instruments are given in Appendix A.

2 The Venus Monitoring Camera experiment

2.1 Scientific objectives of the VMC in the context of this thesis

The main task of the VMC is to provide long term observational data of the Venus atmosphere and to some limited extend of the surface. Observations are conducted on both the day and the night side of the planet. Each of the four channels of VMC is used to follow different scientific objectives, which are described in some detail below.

2.1.1 UV Channel

2.1.1.1 Morphology of the unknown UV absorber

Since the unidentified UV absorber accounts for about 50% of the total amount of energy absorbed from sun irradiation in the Venus atmosphere it is an important factor for the energy balance and dynamics of the entire atmosphere. Identification of this substance is one of the major goals in Venus atmospheric research. Therefore the UV channel of the instrument was chosen to be centered at 365 nm, coinciding with its main absorption wavelength in order to allow for studying its spatial and temporal variability.

The prime questions to VMC UV data with respect to the morphology of the unknown absorber are: How does the amount and distribution of the absorber vary with time and location on the planet? How is it distributed vertically in the cloud deck? In order to aid in answering these questions VMC is monitoring Venus in all orbit phases, continuing studies undertaken by previous missions (Rossow et al. 1980, Esposito 1980). Large scale distribution and variability in the southern hemisphere are observed from the apocenter and early off-pericenter parts of the ascending orbit branch. Intermediate scale data is acquired from off-pericenter observations and high resolution studies on morphology and phase angle dependence of contrasts are performed around pericenter.

These questions and investigations will be the main topic of the following chapter on morphology.

2.1.1.2 Atmospheric dynamics of the cloud tops

The UV markings caused by the unknown UV absorber are regularly used to derive information on cloud top dynamics. Different techniques have been applied to derive wind

fields from tracking of markings caused by the UV absorber (Limaye and Suomi 1981, Limaye et al. 1988, Limaye 1988, Toigo et al. 1994) or infer global winds from streak-feature orientation (Smith and Gierasch 1996).

Tracking of winds at the cloud top is expected to provide insights into one of the greatest mysteries of the Venus atmosphere, the extreme zonal super-rotation. To date it remains an open question how the slow rotating planet reached this state and how stable the global wind field is over time and how exactly the winds, reaching speeds around 100 ms^{-1} at the cloud top, are maintained.

VMC data will be used to obtain long term dynamical observations of the southern hemisphere of Venus. Important scientific questions here are: What is the structure of the zonal super-rotation and the meridional circulation around the planet? How do they depend on latitude and local solar time? Can global wave modes like solar tides or the “4-day” Kelvin wave be identified? Can we observe temporal variability on different timescales?. The global wind field of the southern hemisphere is monitored over extended periods of time from apocenter and off-pericenter. In pericenter, smaller scale dynamics like convectively generated features and gravity waves down to scales of few kilometers are continuously observed. With the unprecedented combination of high imaging rates and long term observations VMC data is expected to improve both temporal and spacial coverage as well as accuracy of dynamic information of the cloud top and its dynamics.

Global wind fields derived from cloud feature tracking in UV images are an integral part of this thesis and are addressed in the dynamics section of the next chapter (section 3.2). Smaller scale dynamic features like localized wave trains at different latitudes are treated in both the morphology and dynamics sections (3.1 and 3.2).

2.1.2 The two IR channels

2.1.2.1 Water vapor abundance and cloud opacity

Water vapor is believed to be involved in the formation of the sulfuric acid aerosols which are abundant in Venus’ upper clouds. Thermal infrared observations have shown large variability of water vapor abundance at the cloud top (Schofield et al. 1982, Ignatiev et al. 1999, Koukouli 2002). A possible cause of the varying H_2O concentrations is convective mixing of the upper cloud layer in which the vertical gradient of water vapor is very steep.

One of the VMC infrared filters is sounding the $0.94 \mu\text{m}$ H_2O band and the other is providing a continuum reference point at $1.01 \mu\text{m}$. VMC IR data is therefore expected to map the spatial distribution of water vapor at the cloud tops and its evolution with time. This data might help to constrain the models of sulfuric acid aerosol formation. Correlations between IR and UV images can possibly help to give additional clues about convection and variations of cloud opacity in the upper cloud and. With sufficient contrast level in the IR observations it is theoretically possible to directly track the progression and evolution of the total cloud opacity variations.

Since this thesis is focused on the UV observations of VMC I will only deal briefly with correlations between UV and IR signals in the morphology section (3.2).

2.1.2.2 Surface and lower atmosphere

Allen and Crawford (1984) discovered a spectral window in the near IR around $1 \mu\text{m}$,

through which thermal radiation from the hot lower atmosphere, down to the surface, can leak into space. This discovery provides a powerful tool to study the surface and lowest parts of the atmosphere even through the thick Venus clouds. As these emissions are orders of magnitude weaker than the $1\ \mu\text{m}$ portion of solar light reflected from the cloud top, observations of them are strictly limited to the night side of Venus. Since intensity of radiation from this spectral window depends mostly on surface temperature and thus on elevation it can provide information about surface topography. Of course also water vapor column density is present in the signal in this spectral window.

Therefore in night side observations the VMC IR channel near the $0.965\ \mu\text{m}$ H_2O band is focusing on the study of spatial water distribution in the lower 10 km of the atmosphere. The channel at $1.01\ \mu\text{m}$ is performing thermal imaging of the surface in parallel.

These investigations are not dealt with in this thesis. Other members of the VMC team have performed both numerical (Ignatiev 2003) studies and data analysis (Basilevsky and et. al. 2008) on the night side observations of the surface and lower atmosphere.

2.1.3 Visible channel

Several types of air glow have been observed on the Venus night side in the past. The spectrometer experiments on board the Venera 9 and 10 spacecrafts have discovered strong emissions in visible wavelengths (Krasnopolskii 1983). From the measured spectrum the emissions have been identified to originate from the Herzberg I and II systems of O_2 with a total intensity of $\sim 3\ \text{kR}$ and were located at roughly 100 km altitude.

The visible channel of VMC is set roughly in the middle of the Herzberg system, covering a spectral range from 500 to 560 nm. O_2 emissions should only be detectable in images with long exposure times and free from any straylight (a condition only met in near-pericenter total eclipses of the sun by Venus). In addition, observations in the visible channel are also infrequently conducted in search for lightning on the night side and to measure the visible albedo on the day side. During these albedo measurements, some unexpected visible contrasts, particularly in apocenter observations have been observed. Also, even more surprising, correlations between small-scale high latitude wave features in the UV, IR and visible channels are present in VMC images.

Since the emissions of the O_2 airglow have proven to be too weak to be detected in VMC images of the night side, I will not deal with the O_2 nightglow in this thesis. Correlations between images from the visible channel with other channels will be discussed in the morphology chapter.

2.2 The Camera

2.2.1 Hardware

The VMC instrument as flown on board the Venus Express consists of one single unit that houses the optics, the detector and all electronics. A sketch and a photograph of the VMC instrument are shown in figure 2.1. The optics contain four objectives with one narrow band filter in each, allowing simultaneous imaging of all four channels onto one common CCD detector. The total field of view in each channel is 17.5° (0.3 rad). In order to

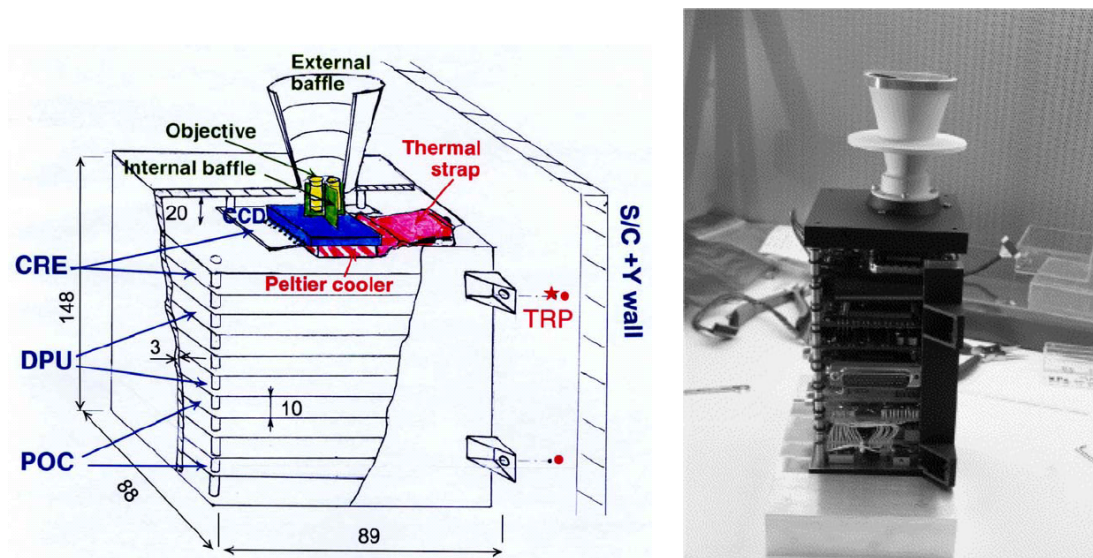


Figure 2.1: *Left*: Sketch of VMC. *Right*: Photograph of the instrument housing with external baffle and the inner electronic boards.

follow its scientific objectives one of the channels is set in the ultraviolet (UV) range at 365 nm, one channel in the visible (VIS) range at 513 nm and two channels in the infrared channels at 965 nm (IR1) and 1010 nm (IR2). All filter bandwidths are only about 50 nm. The optics are shielded from stray light both by an axis symmetric cone-shaped external baffle as well as an internal baffle. In addition both IR and the VIS channel feature an obscuration spot in the center of each channel for protection against “ghost” features. No movable parts have been included in the instrument design, therefore no mechanical shutter nor filter wheels have been built into the VMC. These design properties reduced total instrument cost and provide prevention against any mechanical malfunctions. Figure 2.2 shows the spectral response functions of all four channels, as well as the spectral quantum efficiency of the CCD detector.

The CCD in use in VMC is a KODAK KAI-1010M antiblooming monochrome image sensor. The sensor is coated with a polymeric micro lens layer in order to enhance sensitivity and reduce image smear. Of the 1024x1024 pixel sensor array 1008(H)x1018(V) $9 \times 9 \mu\text{m}^2$ pixels are active and can be used for imaging. Each of the four channels is projected onto a 411x411 pixel array on the CCD, separated by a 200 pixel wide “cross”-shaped structure of dark pixels. The resulting angular resolution of each individual pixel is 0.7 mrad/pixel. Cooling is provided by a Peltier element, connected to the bottom of the CCD by a thermal strap. The CCD full well of 30,000 e^- combined with the 14-bit digital converter gives a system gain of about 5 e^- per DN (Markiewicz et al. 2007a).

The CCD readout electronics (CRE) allow for exposure times ranging from 0.5 ms to 30 s in steps of 0.5 ms. This wide range in exposures permits the observation of both day and night side of Venus. The programmable Digital Processing Unit (DPU) is capable of various onboard image processing steps like data compression, sub-frame cutting, cropping and binning. After processing it routes the image data either to the internal memory with 120 MB storage capacity or directly to the shared mass memory storage (SSMM) of the Venus Express. Storage of one quadrant (524 KB) in the internal

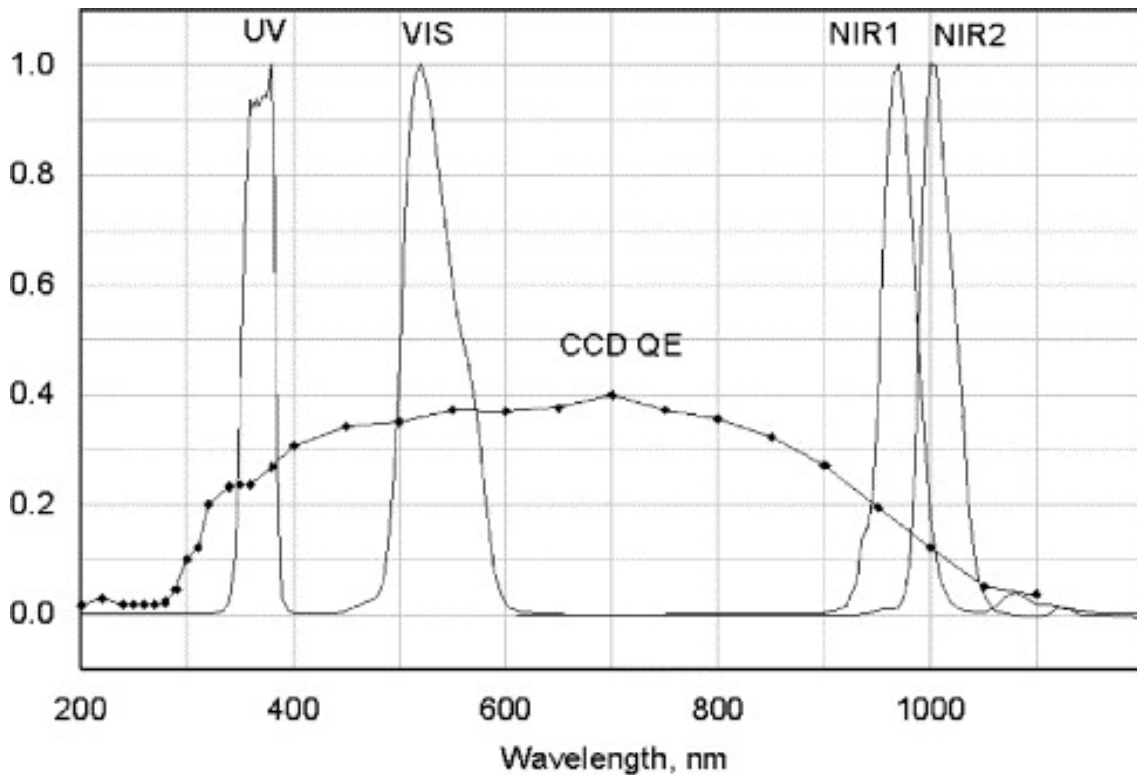


Figure 2.2: Spectral response functions for all four channels and wavelength dependent quantum efficiency function of the CCD.

memory requires 5 s of transmission time and storage to the SSMM roughly 20 s.

The VMC has been calibrated on ground, including full focus tests, radiometric calibration and dark signal analysis. A complete description of the laboratory setup, the measurements and their analysis can be found in the VMC Calibration Report (Document VMC-MPAE-RP-SS011-001).

During the first month after launch, VMC underwent a performance check in a dedicated near-earth commissioning campaign. These checks included observations of point sources (Sirius and Venus) and the Earth-Moon system as well as stray light characterization. Data from this in-flight tests was mainly used to determine alignment between the four channels and the +Z axis of the spacecraft.

2.2.2 Software Architecture of the VMC

Theoretically capable of semi-autonomous operations, the VMC has an own operating system platform on which so called preprogrammed operational programs (POPs) and user defined procedures (UDPs) are executed during science operations. The operating software has been developed by the team of Professor Harald Michalik at the “Institut für Datentechnik und Kommunikationsnetze”(IDA) at the University of Braunschweig. It is structured into seven levels (see also figure 2.3, left) :

1. Levels 0 and 1 provide an interface between the hardware of the DPU with the higher software levels. Level 0 consists of hardware descriptions like address, port

and data definitions. Level 1 handles I/O functions and device drivers

2. Level 2 interfaces sensor, spacecraft and DPU hardware services. It consists of service functions to the front-end electronics
3. Level 3 contains basic image processing procedures. Image sequencing acquisition and evaluation are performed here.
4. Level 4 is responsible for the execution of POP and UDP routines. Image compression is performed on this level, and housekeeping data is collected.
5. Level 5 manages instrument modes (described below) and controls housekeeping data.
6. Level 6 finally contains the POPs and UDPs responsible for science operations.

The operations of the VMC instrument are categorized into a number of instrument modes. Each instrument action is designed to be conducted as part of one of these instrument modes. With the transition into an instrument mode all parts of the instrument electronics are activated that are needed for the dedicated task. After activation of any mode VMC always remains in that mode until the next mode transitions is commanded. While within an instrument mode, VMC stays in a default sub mode and cycles through a fixed series of other sub modes upon execution of UDPs or POPs. The implemented modes are: Cooling, Calibration, Monitor, Pericenter, Limb and Transmission. An overview of all modes and their transitions is shown in figure 2.3 on the right. To give an illustrative example, let us take a look at the Monitor mode. The default sub mode here is “Cool only”, which means that while all electronics are enabled only the Peltier cooler is active and cooling the CCD. Upon commanding of an image, VMC first switches into “Image acquisition”, thus activating the CRE, which stays active until the next sub mode “Image readout” in which Image data is handed over to the DPU. Then, in the “Processing + cooling” stage data is being processed in the DPU and routed either to the VMC memory or the SSMM. Finally, VMC is switching back to “Cool only”, awaiting the next command to execute. The “Transmission” mode is exclusively needed to transfer stored Image data from the internal VMC memory to the SSMM on the spacecraft. Since the VMC memory is a SDRAM storage, data stored there must always be transferred to the SSMM before the instrument is switched off in order to prevent data loss.

2.2.3 The SingleImage routine

My first task at the beginning of the work for this thesis was to program a versatile imaging routine that was capable of interpreting image acquisition commands sent to the spacecraft, execute image acquisition, cut sub frames from the complete CCD-readout images and allow for routing data to either internal VMC memory or the SSMM. I programmed the so called “SingleImage” routine in the hardware specific Onboard Commanding Language (OCP). The routine is an example for a UDP and accepts the following parameters:

1. *Image_number*: An unsigned 32 bit binary encoded integer number specifying a preferably unique, numerical value for each image. The convention is to use six

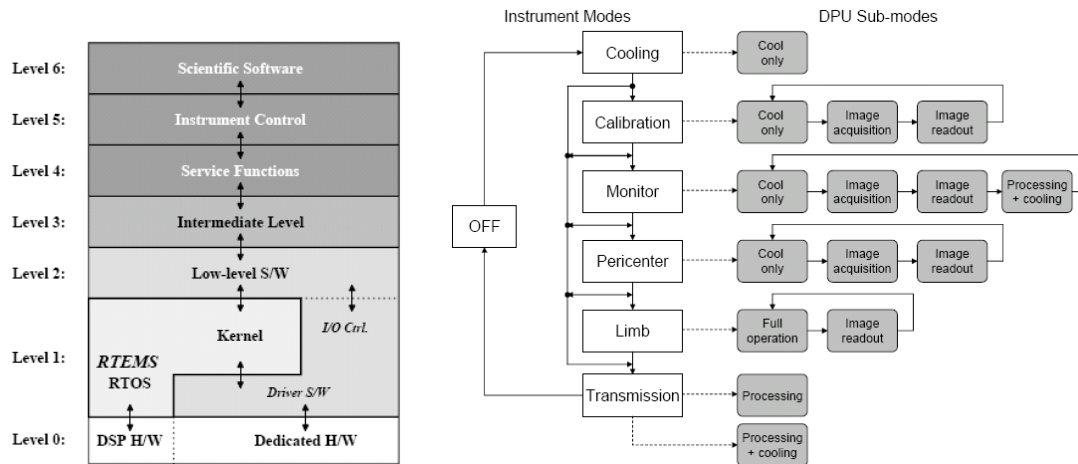


Figure 2.3: *Left*: Multi level architecture of VMC OS. *Right*: Overview of instrument modes and submodes and transitions between them.

digit number with three digits for the orbit and three digits for the image number in that orbit (in decimal representation).

2. *Exposure_time*: An unsigned 32 bit binary encoded integer number giving the amount of 0.5 ms intervals to be concatenated to reach the desired exposure time.
3. *Mask*: An unsigned 8 bit binary encoded integer number used as a bit mask, controlling which channels are to be sent to the storage after CCD readout. Only the lower four bits are used at this moment, each bit corresponds to one of the four VMC channels. Therefore any combination of channels can be chosen for storage from a CCD readout, see table 2.1.
4. *Special_flags*: An unsigned 8 bit binary encoded number controlling where the image data is to be stored. Only the lowest bit is currently used. If the bit is set to 0, data will be routed to VMC internal memory. If set to 1 data is transferred directly to the SSMM via the high speed link.
5. *Comp_flags* and *Comp_value*: Two unsigned 16 bit binary integer numbers. *Comp_flags* is used to enable different compression methods. *Comp_value* sets the size to which the compressed image file should be reduced, relative to the original image file size according to the formula

$$Size_{Compressed} = Size_{Original} \cdot \left(1 - \sum_{n=1}^{16} 2^{-n} \right)$$

Where n is the number of the bit (from low to high). This allows in principle for very accurate size determination of compressed files in steps of 2^{-16} times the original file size (=64 bits for images of individual channels)

6. *Processing_flags*: An unsigned 16 bit binary encoded number intended for use as a bit mask to trigger different on board image processing POPs. Currently this parameter is not in use.

Bit number	1	2	3	4
Bit value	2^0	2^1	2^2	2^3
Channel	IR1	VIS	IR2	UV

Table 2.1: Bitmask values and corresponding VMC channels. Channels are selected by setting the according bit to 1. If all bits are set to 0 the whole CCD readout is transmitted in one file. If all bits are set to 1 all four channels are transmitted in four individual files.

So far image compression is not being used by the VMC. When the routine was uploaded to the spacecraft during cruise phase, the compression POPs had not been available and since this precluded testing of the compression parameters at IDA in Braunschweig it was decided to deactivate this functionality for safety reasons.

2.3 Observations and Planning

Since the VMC optics have a fixed angular resolution the distance from Venus determines spatial resolution on the planet. Around apocenter ($\approx 66,000$ km distance) the resolution on the planet is about 50 km per pixel, increasing to few 100 m per pixel in pericenter. The complete Venus disc is visible outward of about 40,000 km away from Venus. Therefore the VMC is following different scientific objectives in the previously described phases of the Venus Express orbit (see section 1.3). Table 2.2 summarizes typical image resolutions and according observation types.

	Pericenter	Off-pericenter	Apocenter	Limb
Distance	250-10,000 km	10,000-50,000 km	50,000-66,000 km	~ 2000 km
Total field of View	70-3000 km	3000-14,000 km	14,000-20,000 km	~ 500 km
Spatial Resolution	0.2-7 km	7-35 km	35-48 km	~ 1.5 km
Typical timing between images	8-300 s	5-10 m	>10 m	~ 8 s

Table 2.2: VMC observation types.

Satellite observations at Venus imply certain constraints which have an impact on the acquisition of scientific data. The most immediate limiting factor in the inner part of the solar system are thermal constraints due to Sun illumination of the spacecraft. Since only the instrument (+Z) and high gain antenna (+X) walls of the spacecraft are designed to withstand long-standing sun illumination. Exposure of other walls to direct sunlight is only possible for a certain duration of time and is followed by thermal recovery times of 12-22 hours. Durations of VMC observation periods as well as available observation geometries are impacted by these thermal constraints.

Other factors constraining observations are spacecraft maneuvers and the telecommunication phase in the descending orbit branch. An important limitation to the total number of images we can acquire in a given orbit is the data downlink capacity during the telecommunications phase. This of course depends on the relative position of Venus, Earth and the Sun. Data rates are highest between quadratures when the distance between the spacecraft and the receiving ground stations is small and angular distance between Sun and Venus, as observed from Earth, is maximum. Lowest available data rates are reached close to opposition, when the Sun is closest to the line of sight to the spacecraft.

Additional limitations are present during pericenter observations, when rapid imaging is necessary and therefore all images have to be stored in the internal memory of VMC. The maximum amount of images that can be acquired during one pericenter pass is about 100 images. Also the current implementation of the image acquisition software requires ~5 seconds to crop individual channels from the full CCD frame, leading to a minimum imaging interval of 8 seconds (image processing time plus 3 seconds safety margin). In apocenter and off-pericenter imaging the imaging frequency is limited even more by transmission times of image data to the SSMM. These transmission times allow for minimum time intervals of 20 seconds. Especially for night side images, when exposure times are 30 s, the exposure times have to be added to the minimum imaging intervals.

After spacecraft attitude and observation slots have been implemented according to the mentioned constraints, VMC image sequences are compiled to yield a maximum in spatial and temporal coverage for the conducted observations. In apocenter and off-pericenter observations on the day side, time intervals between images are chosen such that, at the given progression of spatial resolution, cloud features move by an equal amount of pixels. Images are then timed according to:

$$t(n)_i = n \cdot \frac{u_c}{d_i \cdot \tan \alpha_p} ; d_i = d_{i-1} - \langle v \rangle_{[t(n)_{i-1}]} \cdot t(n)_{i-1}$$

Where $t(n)_i$ is the time interval (number i in an image sequence), during which clouds get displaced by a number of n pixels, as a function of distance d_i from the cloud deck, the approximate (zonal) cloud speed u_c and the angular resolution of one pixel α_p . Since cloud speeds are not known a priori, a zonal speed of 100 ms^{-1} is used as a standard approximation. The time intervals progress as a series, depending on the preceding position d_{i-1} and the average speed $\langle v \rangle_{[t(n)_{i-1}]}$ during the preceding time interval.

The desired amount of displacement in pixels is determined by length of observation slots and available data volume. Apocenter and off-pericenter observation times vary between ~3-10 hours in which usually about 50 images are taken in the UV channel. If data rates are high enough, an equal number of images gets taken also in one or both IR channels plus a small number of images in the VIS channel.

During pericenter observations, spacecraft motion and shrinking field of view necessitate an image timing (and attitude control) which provides for maximized coverage on the planed and overlap between images. At the beginning of the pericenter usually image sequences with an overlap of 25-66% (depending on available on board data volume quota and downlink capacity) are taken in order to allow a composition of mosaics. As the velocity of the spacecraft increases, overlap is constantly decreasing as soon as the minimum time intervals of 8 seconds are reached. The number of images per pericenter passage ranges between 30-100, depending on data downlink capacity.

Planning and compiling imaging sequences had been my second task after the development of the SingleImage UDP.

2.3.1 Artifacts in VMC images and removal procedure

It was known before the start of the mission that the +z axis of the spacecraft, and therefore the VMC instrument, might be pointed directly toward the sun during the cruise phase. In order to evaluate the possible threat of damage to the detector, simulations of sun illumination have been modeled numerically and conducted in laboratory experiments during the calibration phase of the Instrument. During the laboratory tests the detector was exposed to a $\sim 10^\circ$ wide beam of simulated sun light for a duration of 11 hours. The test results showed no signs of degradation of the instrument.

However, the sun image during flight was only $\sim 1^\circ$ wide, possibly resulting in critically higher flux levels onto the detector. Also the known sensitivity to UV light of the micro lens layer on top of the CCD has not been provided by the manufacturer prior to the discovery of the artifact patterns in the VMC images. With no shutter to protect the detector from sunlight, the sun shone directly on the detector for more than 500 hours in total. Upon arrival at Venus, a complicated pattern of artifacts proved to be constantly present in VMC images. Figure 2.4 shows an original VMC image on the left and the complete artifact pattern on the right.

The artifact pattern shows actually two different kinds of features. One is the dark strip, situated approximately at the middle of the image and extending nearly all the way through it. This feature was dubbed the “dark UV strip”, since it is seen only in the UV channel. Detailed investigations revealed that the dark UV strip was produced from yellowing of a micro lens layer on top of the CCD due to strong UV irradiation from the sun, attenuating the signal where it is present. The second artifact pattern, spreading across the whole CCD (in all four channels) is characterized by an irregular pattern of bright filaments and bright and dark patches and spots. This pattern has been dubbed “filament=spot pattern” or FSP. In contrast to the dark stripe, which remains constant in size, shape and signal attenuation level, the FSP are evolving slowly over time on timescales of several days. The cause of this pattern is not known for sure yet, but I have done studies on their behavior over time. More details on the artifact patterns and the result of the studies on the FSP are given in Appendix A.

In order to clean VMC Images from those artifacts we use sets of pericenter images, preferentially acquired at high latitudes during most orbits. The relatively featureless cloud cover in near-polar latitudes provides a fairly uniform background, usable for in-orbit flatfielding. All images in one sequence are then added up, resulting in almost completely uniform signal levels from the Venus cloud deck in the summary images. Since artifact patterns change only marginally in each orbit, their contributions to the signal add up and stand out prominently in these sum-images. The next step is to normalize the summary images to the mean signal level, obtaining an orbit-specific flat field mask. By dividing a raw VMC image by the flat field mask, the systematic variations due to the artifact patterns are removed from the images. The according formula for this procedure is:

$$\hat{\Phi} = \frac{\sum_{k=1}^N \sigma_k}{\langle \Phi \rangle} ; \sigma_{clean} = \frac{\sigma_{raw}}{\hat{\Phi}}$$

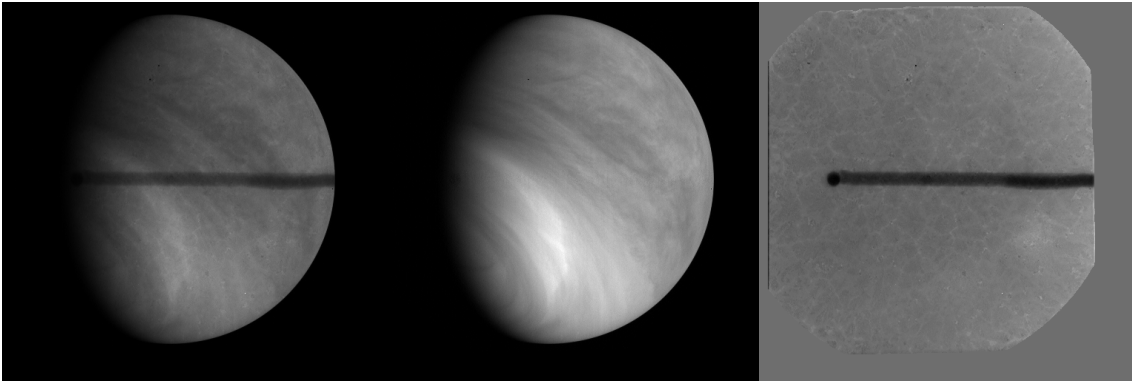


Figure 2.4: *Left:* Original VMC image. *Middle:* VMC image after artifact removal. *Right:* Extracted flatfield matrix, containing artifact patterns.

Where $\hat{\Phi}$ is the normalized flatfield matrix, N the number of images in a given flat field sequence, σ_k the individual raw image matrices and $\langle \Phi \rangle$ the mean signal level in the sum image. The Minnaert coefficient k was empirically determined and the value used was $k=0.55$.

This method has some obvious limitations and drawbacks. Due to availability of observation slots in each orbit it is not always possible to obtain an image sequence at high latitudes, which fortunately occurs only seldom. Also in some cases we are not able to construct sufficiently uniform signal levels in the sum-images. This happens when relatively prominent high-latitude features (e.g. bright and dark polar bands, see morphology section) are present. Also a strong brightness gradient remains when the orbital plane is at very low angles with the terminator plane. Fortunately Thomas Roatsch and Klaus-Dieter Matz from the German Aerospace Center (DLR) in Berlin have created workaround solutions that help to overcome these limitations. Since the FSP are evolving in near-linear fashion over short timescales, single orbits without flat fielding image sequences can be flatfielded by interpolating between the flatfield matrices from the predecessor and successor orbits. The same procedure also helps to overcome isolated cases in which too many features are present in the high latitude image sequences.

However, brightness gradients present in near-terminator orbit images can not be completely removed by cosine correction of the signal with respect to the solar aspect angle, due to light scattering in the Venus atmosphere. Thus the removal of the artifacts is usually paid for with a slight residual gradient in these orbits. We also have cases in which the FSP evolve sufficiently in the course of a single orbit to change their appearance enough that traces of their presence remain. Whenever this is the case we take great care to verify all identified morphological features by comparison of subsequent images, when they are clearly displaced by spacecraft motion, in order to ensure that no false identification of artifacts is being made.

One thing that cannot be avoided is noise amplification in areas with dark artifacts. It is obvious that the signal to noise level is decreased proportionally to the level of darkening, e.g. the noise is amplified by a factor of 2.5 and more in the dark UV stripe. Therefore the UV stripe area and a varying part of the FSP will be recognizable from locally amplified noise profiles in highly contrast enhanced images.

Channel	Case #1	Case #2	Case #3	Limb-type (Cases #5-#7)
UVI	3413 (58)	20245 (323)	2207 (0)	3210 (77)
IR1	2303 (1260)	5336 (1502)	1175 (344)	1397 (223)
IR2	2871 (1364)	8518 (4294)	1341 (338)	1843 (831)
VIS	342 (58)	2862 (329)	446 (0)	1051 (173)

Table 2.3: Summary table of the VMC image inventory until orbit 530. Numbers are given for total amount of images per channel and science case. Numbers in parentheses give the subset of night side images.

2.4 The dataset

2.4.1 Statistics

During the first 530 orbits, VMC acquired an inventory of 59000 Images. Since most science goals are based on observations in the UV, roughly 50% of all images are taken in this channel (29000 Images). Of the ~ 10000 Images taken in the IR1 channel 60% were acquired on the dayside cloud deck, and 40% were dedicated to nightside surface observations. For the 14000 IR2 images the ratio was $\sim 50\%$ for both day- and nightside. Table 2.3 gives a detailed overview of the number of images acquired in each channel and for which science case (a description of the science cases is found in section 1.3).

Typical coverage on the planet in case-1 images ranges between $\sim 20^\circ$ S in latitude and longitude near the equator in early pericenter images, down to less than one degree in both directions per image in high northern latitudes. Case-2 images usually cover large parts of the southern hemisphere ($\sim 30\text{-}50^\circ$ in latitude/longitude). Case-2 images from distances greater than 35000 km and case-3 images basically show the whole southern hemisphere from pole to equator.

On the day side, coverage is usually referred to in terms of local solar time, since only clouds are observed. The total coverage of the day side within the first 530 orbits is slightly biased toward the evening side by cases-1&2 observations. On the night side, where the lower atmosphere and surface is imaged through the $1\mu\text{m}$ window, the coverage is referred to normally as latitude/longitude. The approximate coverage of surface imaging before orbit 530 ranges from 210° to 310° eastern longitude and 30° S to $\sim 45^\circ$ N in latitude.

2.4.2 Data description

The VMC images are retrieved in individual channel frames as data arrays of 512 by 512 pixels with a 16-bit depth of the signal levels in each pixel. Figure 2.5 shows an example of four images in the four individual channels in the VMC coordinate frame taken approximately 1 minute apart from each other. In this example the cross which separates the channels is superimposed in order to show its position on the CCD.

Due to the downscaling of the gray-scale from 16 to 8 bits for display on monitors and print-outs, the contrasts in the images are muted. Also a strong brightness gradient from the non-uniform sun illumination can be seen. In order to facilitate orientation and identification of features on the Venus disc, all other images presented in this thesis will

be shown rotated, contrast enhanced and brightness corrected. The rotation will be such that the bottom of the images will be oriented toward the south direction and the right edge will be oriented to the east direction. Contrast enhancement is done with simple contrast stretching in apocenter and off-pericenter images and with histogram equalization in pericenter images. The brightness gradient from solar illumination is removed with a simple Minnaert function of the form:

$$I_M(\Psi) = I \cdot \cos^{-k} \Psi$$

Where I_M is the corrected and I the original signal level, Ψ is the solar emission angle and k is an empirically determined parameter.

Further, the images are identified by a frame number consisting of their orbit number and image number within that orbit, both given as four-digit numbers. For example the 60th image in orbit 465 is identified by the frame number 0465_0060.

In addition to the individual display as 512x512 pixel arrays, the overlap between images in pericenter sequences allows for the creation of mosaics, composed of several images acquired in an image sequence. An example of a mosaic from VMC images is shown in figure 2.6.

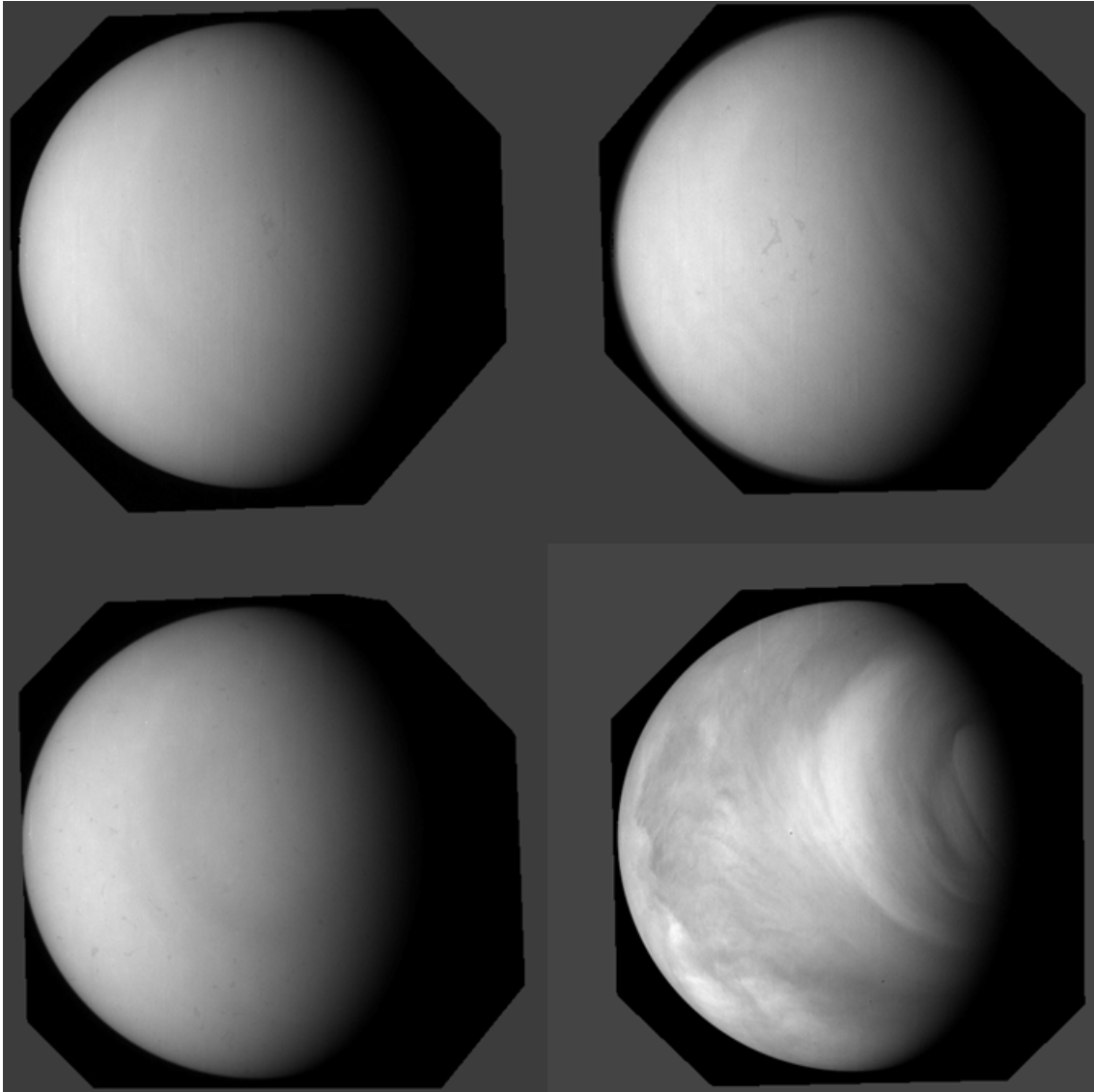


Figure 2.5: Typical VMC images from off-pericenter observations in orbit 465. The channels are: NIR1 in the upper left, VIS in the upper right, NIR2 in the lower left and UV in the lower right. (Image frames: 0465_0062, 065_0064, 0465_0063, 0465_0060)

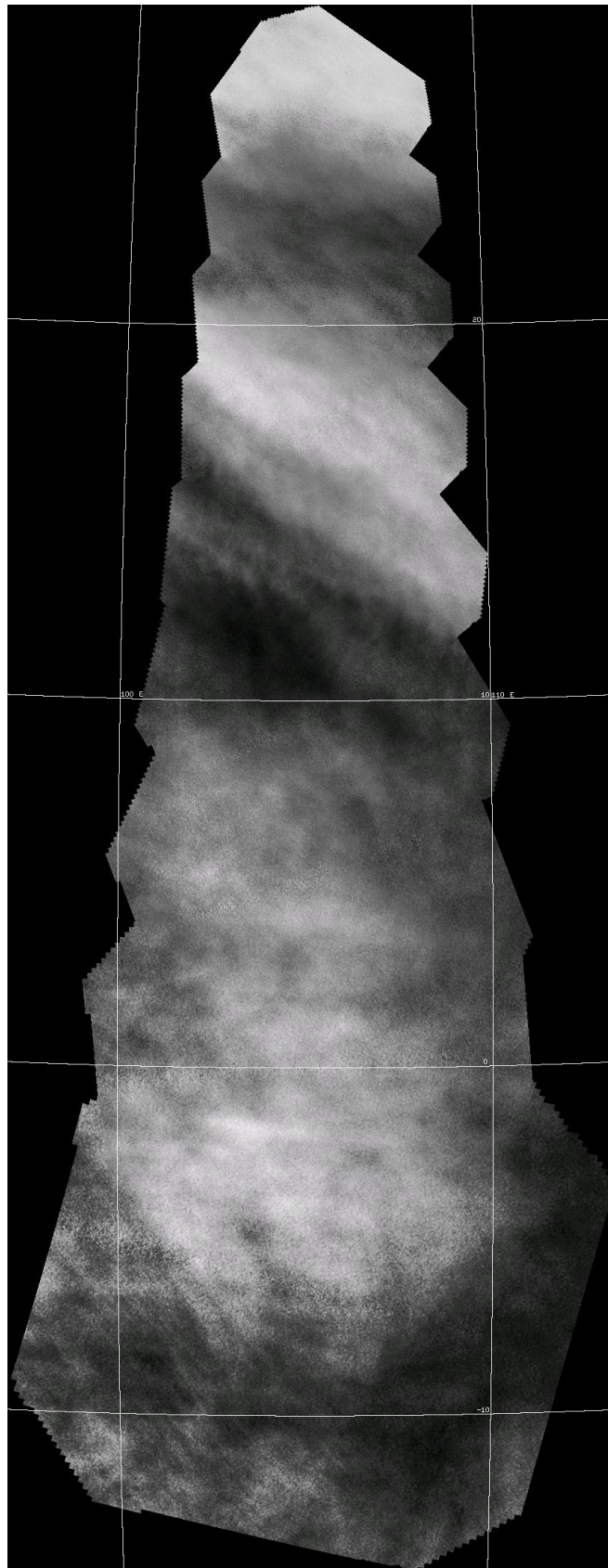


Figure 2.6: VMC pericenter mosaic from orbit 114.

3 Results

3.1 Cloud top Morphology

3.1.1 Overview

Cloud top morphology on Venus is usually studied in the ultraviolet spectral range by observing the dark and bright albedo patterns caused by the presence or absence of SO₂ and the unidentified UV absorber and contrast variations due to variations in the optical thickness of the clouds. According to Pollack et al. (1980), the UV unknown absorber is situated mainly a few kilometers within the cloud top. Measurements of the net flux in the UV-blue range indicate that the absorber is mainly present at lower altitudes of the upper cloud layer (~61 km) but not in the middle and lower regions of the main cloud deck. Contrasts in the lower latitudes are likely produced by absorber being mixed in the clouds but destroyed by photo-dissociation at the topmost region of the clouds. Therefore dark markings in the equatorial regions are associated with downdrafts and bright regions with updrafts of the convection triggered from solar heating there. In higher latitudes the contrasts are presumably caused by the so-called “haze mechanism”. According to this model, UV bright areas in high latitudes are generated by an enhanced optical depth of the upper (sulphuric acid) haze layer, while UV dark areas are characterized by lower haze densities and therefore better visibility of the altitude where the UV absorber is present.

Pollack et al. (1980) also state that the unknown UV absorber would also be suspected to absorb radiation longward of 0.5 μ m. This in turn lets one expect correlation between the UV and the VIS channel of VMC. Also the haze model would imply correlations between the UV and the IR channels, since denser upper haze should also show up brighter around 1 μ m, than regions where the optical depth 1 is reached at a lower altitude.

The highly elliptical polar orbit of Venus Express (compare fig. 1.7) allows for observing the planet from a wide range of distances and with varying resolution. But at the same time, Venus appears somewhat different than in earlier observations from a more equatorial perspective. In order to connect and compare the VMC observations of the cloud deck in the UV channel to findings from earlier missions, this overview is intended to introduce the regularly used morphological terminology on the numerous types of UV patterns across Venus (expanding on the descriptions from the introduction chapter). The sketch in figure 3.1 from Rossow et al. (1980) shows a schematic collection of the known morphological features that have been detected from terrestrial as well as from space borne UV imaging. The sketch was created on the basis of Pioneer Venus observations and reflects the appearance of Venus from the viewpoint of the equatorial plane.

From the general appearances of the cloud features one can roughly distinguish three

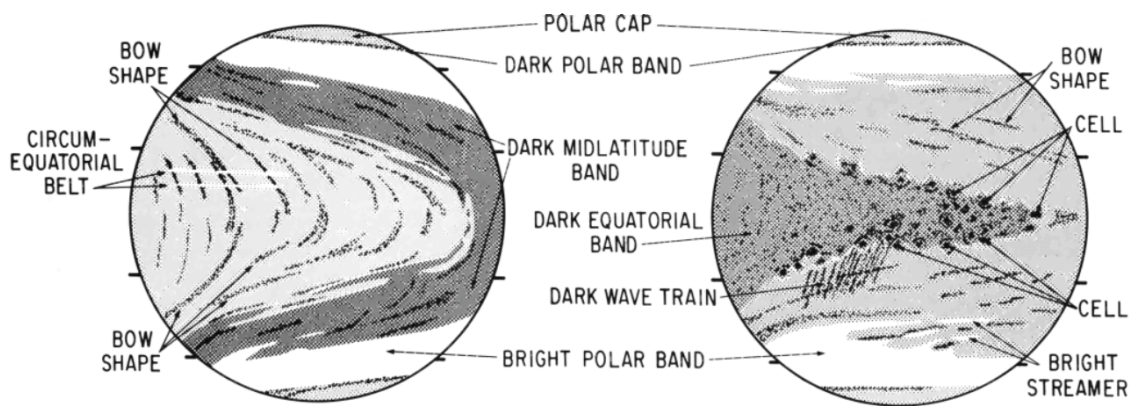


Figure 3.1: Schematic summary of the basic types of cloud features on Venus in the UV. The left sketch depicts the situation with maximal tilted bands, the right one with minimum tilt configuration. The tick marks on both circles indicate 20° and 50° of latitude in both hemispheres. From: Rossow et al. (1980)

separate latitudinal regimes: a polar regime poleward of $\sim 50^\circ$ latitude in both hemispheres, a mid-latitude regime between about 20° to 50° and finally a near-equatorial regime between $\pm 20^\circ$ latitude around the equator. Each of these three regimes shows a number of typical patterns, setting them apart from each other. However, they are not strictly separated from each other by clear boundaries but rather pass gradually into each other. The latitude boundaries given are therefore to be understood as average values and may vary by about $\pm 5\text{-}10^\circ$ at any individual times. Appearances of all three regions have been observed to vary widely and seemingly chaotically over time.

The polar regime is characterized by drawn-out (spiral) band type features and a general absence of isolated small scale markings. Directly at the poles Venus usually appears to have a **bright polar cap**. Which, in contrast to the other terrestrial planets, is of course not an ice cap but most likely a sort of vertically thin haze-“lid” covering the eye of the polar vortex (Taylor et al. 1990). This cap is confined by one or more narrow **dark polar bands**, of which the innermost are usually situated at $70\text{-}75^\circ$ latitude. In the case of so called “polar brightening” events, no dark polar bands are observed. The question whether they are covered by bright higher altitude hazes or are not physically present is a matter of ongoing investigations. The boundary of the polar regime is given by the **bright polar bands** which, despite their name, extend down to $65\text{-}45^\circ$ latitude, which is already extending into the mid-latitude dynamical regime. The most frequent and obvious variation in the polar region is the change of alignment of the polar bands between steeply tilted ($\sim 30^\circ$) and parallel with respect to the equatorial plane. In some cases **dark and bright streamers** have been reported. These are elongated, smaller scale streaks that appear inside the bright and dark polar bands respectively. It has been argued that they might represent traces of interaction between the polar and mid-latitude regimes.

The transition to the mid-latitude regime is marked by the **dark mid-latitude bands**. In tilted configurations these broad (spanning up to several degrees of latitude) dark bands sometimes span in length over the entire range of the mid-latitude regime, virtually connecting the near-equatorial and the polar regions. Together with the **bow shaped features** they often appear symmetrically in both hemispheres, mostly superimposed on or parallel

to each other. The dark mid-latitude bands are therefore to be identified with the arms of the previously mentioned sideways Y-feature and mark a large scale combination of zonal and meridional flow. The bow shapes are the morphological tracers of the bow-like waves mentioned in the introduction chapter and they can be tilted by as much as 30-40° even when the larger band structures are in a zonal (non-tilted) configuration. Ripple-like fine structures have been seen in high resolution Pioneer Venus and Galileo, which are superimposed approximately perpendicular on both the bow shapes and the dark mid-latitude bands, sometimes giving their edges a ragged appearance.

These ripples or **wave trains** are especially prominent at the border to the equatorial regime. Around the equator a typical large scale feature is the **dark equatorial band**. When the mid latitude bands connect at the equator with the equatorial band in a common vertex, the famous Y-shape is produced. Depending on combinations of these markings and tilt configurations also inverse **C-**, **V-** or sideways **Ψ** shapes are formed. The dark equatorial band is especially prominent in low-tilt configurations. Other wave features in low latitudes are the **circumequatorial bands**, which also have been mentioned in the introduction chapter. It remains an enigma why these extremely thin and long equator-parallel features have only been observed to progress southward regardless of hemisphere (Rossow et al. 1980). The **cell-like features** appear to be exclusively constrained to the low latitudes. While often producing a mottled appearance of the cloud deck around the equator, they seem to be more drawn out toward the border of the near-equatorial regime. Thought to be originating from convective action the irregularly scattered cells seem to form preferentially near, and downstream of, the sub solar point. They have been reported in two varieties: **dark rimmed** brighter cells with sizes of ~500-1000 km in diameter and smaller **bright rimmed** dark cells, spanning ~200-500 km. Vertical size and therefore aspect ratios of these convective cells have been debated since a long time, since they hold various implications on vertical transport of mass and momentum in the Venus atmosphere.

Prior to Venus Express the smallest observed scales in terms of cloud morphology were about 30 km. In the following I will present the view of VMC on the above described previously known features, their possible sub-structures and some newly discovered features.

3.1.2 Cloud morphology from VMC images

3.1.2.1 Apocentric observations of the south polar region

As presented in table 2.2, the usual resolution around apocenter ranges between 35-48 km per pixel, comparable to average resolutions of earlier Venus missions and the highest available resolutions from modern ground based observations. The main difference is that the apocenter of the Venus Express orbit enables a direct overview of the south polar region, making it possible for the first time to conduct long term observations of polar morphology and dynamics for extended durations in each orbit. All apocenter images presented here have been corrected with a Minnaert function in order to dampen the brightness gradient resulting from Venus's spherical shape and allow a better view of the near-terminator structures. As apocentric observations are separated by about 12 hours from the pericenter passes in which VMC is taking its so called "flat-fielding" image

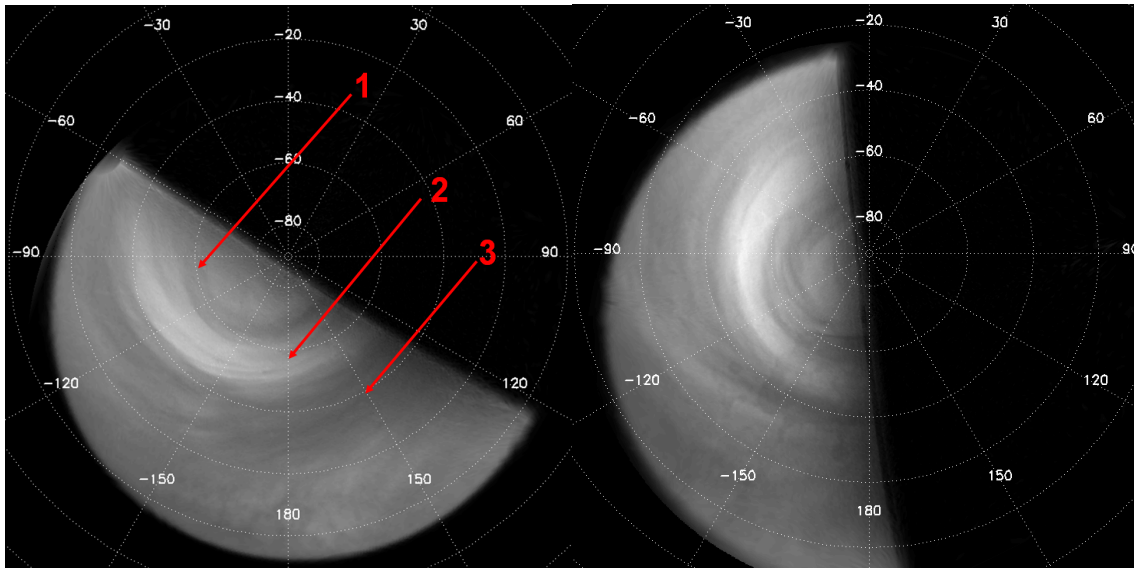


Figure 3.2: Contrast enhanced VMC UV images in polar projection. The numbers in red indicate the essential features typically present in apocenter images: 1= dark polar band; 2= bright polar band; 3= dark midlatitude band. *Left*: Band configuration with a relatively strong tilt. The bright polar band extends from about -40° up to more than -60° and dark mid-latitude bands to about -55° . *Right*: Bands are in mostly zonal configuration. The bright band is approximately aligned with the -50° meridian. Rotation of the atmosphere is counter-clockwise.(Image frames: 0038_0047, 0288_0026)

sequences, they suffer regularly from remainders of the evolving artifact patterns.

Viewed from around apocenter, the dark polar band appears as a closed elliptical/circular feature or an open spiral, roughly centered around the south pole and with various tilt configurations. Figure 3.2 is a selection of two cases with differently tilted polar and mid-latitude bands that are approximating the tilt configurations depicted in figure 3.1. In both images the dark and bright polar bands and a dark midlatitude band are visible. Also several dark and bright streamers are present. In the left image, with a strong tilt in the bands, even some cell-like features are visible up to 20° latitude. The image to the right features a broad dark equatorial band.

The VMC observations from apocenter comprise the first global scale and long term observations of the cloud deck from a polar perspective. As can be seen in figures 3.3 and 3.4, the appearance of the south polar region is varying widely between orbits. Although the appearance of this region is virtually as individual as a human fingerprint, some general properties stand out on a regular basis and lead to a number of (qualitatively) recurring configurations of the polar region.

The dark and bright polar bands have been observed in numerous orbits to appear as almost perfectly circular features, an example is shown in figure 3.3.(a), where the dark polar band is seen as a $\sim 5^\circ$ wide closed circular band around 70° latitude. On other occurrences the dark polar band appears as a strongly deformed ellipse (fig. 3.3.(b)). A common property in both cases is that the dark polar band seems to be completely separated from the mid latitude bands by the bright polar band encircling it. This possibly hints

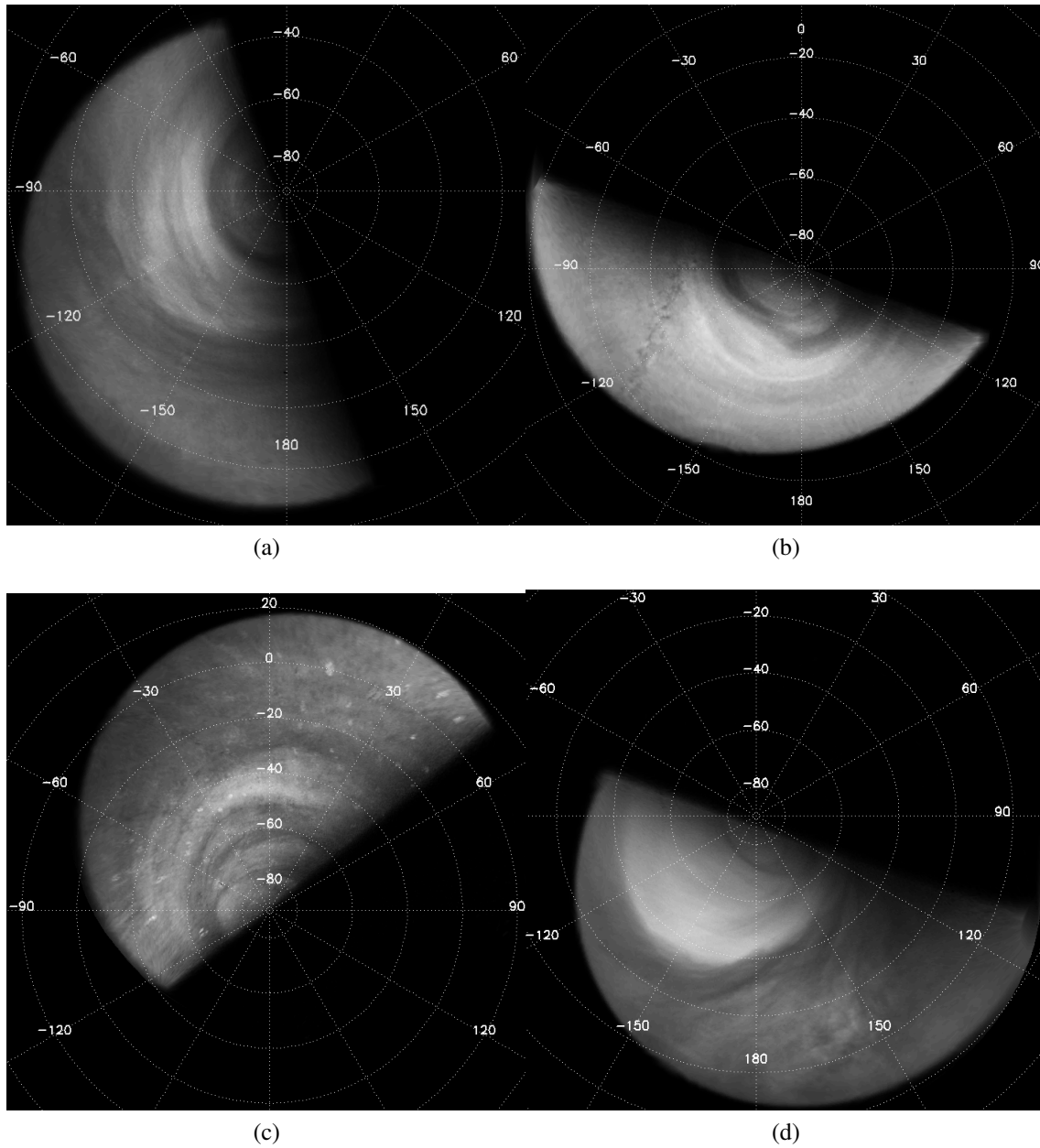


Figure 3.3: Variable appearance of the high latitude region in different orbits. (Image frames (a) 0051_0042, (b) 0384_0029, (c) 0423_0000, (d) 0267_0000)

at a relatively weak meridional coupling between the mid- and high latitude dynamical regimes.

In other cases several, approximately concentric, elliptical dark polar bands are detected (fig. 3.3.(c)). In this configuration, the dark ellipses are not only concentric but also seem to be connected with each other. Since these “systems” of connected dark bands are spanning latitudes from $\sim 80^\circ$ S down to about 55° S it is difficult to tell “polar” and “mid-latitude” band features apart from each other. Similar configurations have been reported from Pioneer Venus observations of the south polar region by Rossow et al. (1980), where they have been described as a broad bright polar band, interrupted by several tilted unusually narrow dark bands (seen from a more equatorial perspective). Indeed, the dark bands appear to be less broad ($1\text{--}3^\circ$) in the latitudinal direction, when organized in such systems.

At least one so called “polar-brightening” event has been observed by VMC (see fig 3.3.(d)) (Markiewicz et al. 2007b). Such events have regularly been detected by terrestrial (Dollfus et al. 1975) and Pioneer Venus (del Genio and Rossow 1982) observations. They are characterized by the presence of a vastly enlarged bright polar cap, extending down to latitudes of $\sim 40^\circ$. del Genio and Rossow (1982) concluded that such events are caused by the formation of dense bright H_2SO_4 hazes above the clouds, blocking the dark markings from view. However, a very narrow dark elliptical band is seen in figure 3.3.(d) between $70\text{--}80^\circ$ S latitude. Also recent studies on cloud altimetry from VIRTIS and VMC data (Ignatiev et al. 2008) concluded that the bright areas in this case are not necessarily seen at higher altitudes than the dark markings. Therefore it seems possible that the polar brightening events may be caused by dynamic influences at cloud level.

In several cases, the polar bands were not present as closed elliptical features but rather as “open spirals”. Figure 3.4.(a) shows such a case in which dark and bright polar and mid latitude bands appear to form such a spiral configuration. Clearly, the innermost dark polar band (at $\sim 70^\circ$ S latitude) is not a closed elliptical feature but rather forms the innermost part of a spiral structure, probably continued by the second in the second dark band (at $\sim 60^\circ$ S) and possibly in the third dark (mid-latitude) band around 40° S.

The polar region has also been observed to show exotic configurations (see fig. 3.4.(b)) in which several narrow dark polar bands are present between the pole and $\sim 55^\circ$ S, which appear to be either broken or consist of elliptical bands with varying orientation with respect to each other.

On several occasions, the polar region displayed a correlation between features seen in the UV, visible and infrared channels. Correlations between features seen in the UV and the visible range in the south polar region have already been reported by previous observations from Mariner 10 (Belton et al. 1976b). Also correlations between UV and IR features have been detected by Galileo observations (Belton et al. 1991). Figure 3.5 shows a comparison between Images taken one minute apart from each other in the UV (a), the VIS (b) and the IR1 channel (c). All three images are contrast enhanced and Minnaert corrected and displayed as original images with a superimposed latitude/longitude grid. In this example, correlations are seen for a narrow dark polar band extending from $\sim 80^\circ$ to about 65° latitude (from $0\text{--}60^\circ$ longitude) between UV and VIS channels and the poleward edge of a second dark polar band between $70\text{--}60^\circ$ latitude in all three channels.

A further look on the correspondence between the UV and the VIS channel (figure 3.6) in the two preceding orbits (437 and 438) shows a similar correlation between the

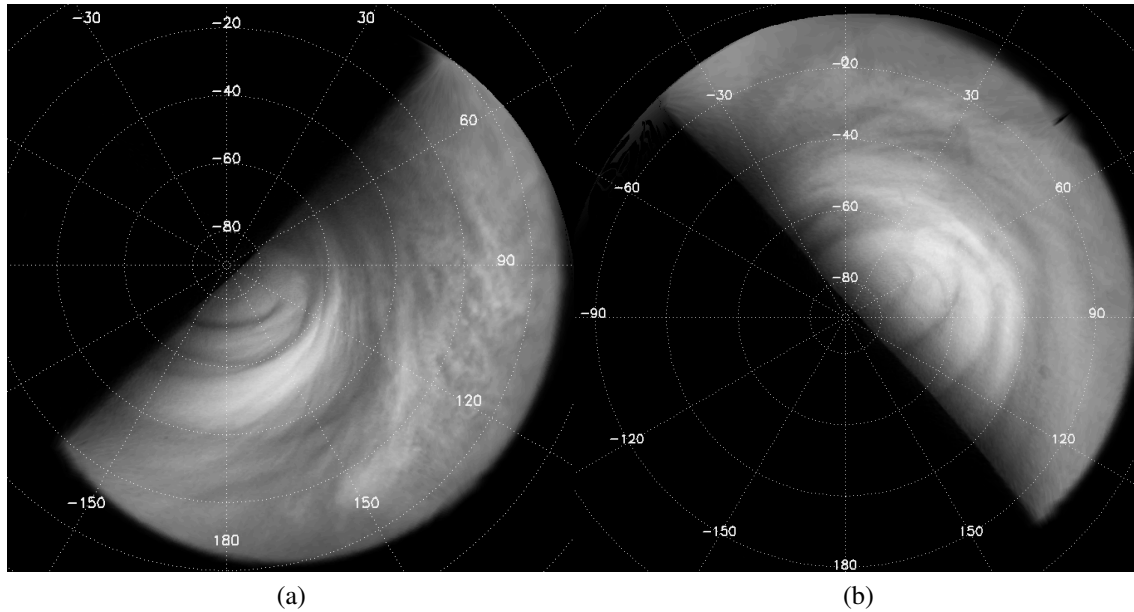


Figure 3.4: Variable appearance of the high latitude region in different orbits. (Image frames: (a) 0246_0000, (b) 0217_0000)

UV and VIS channels. Again, the correlation seems to be localized precisely at the border regions of dark UV features, rather than the entire dark marking in the UV. One possible explanation for this localized correlation is that contrast values in the broad part of the band are too low to be detected in the VIS channel. Keeping in mind the slant sun-incidence angles in high latitudes another, hypothetical, explanation for the localization of the contrast in the VIS channels would be the assumption of shadowing due to sudden altitude changes at the borders of the dark bands. This scenario would be in agreement with the assumption of contrasts generated by the haze model described by Pollack et al. (1980). Since satisfactory contrast correlations between the UV and VIS channel in the polar region have only been detected in a few orbits so far, more observations are needed for further and more quantitative investigations of this hypothesis.

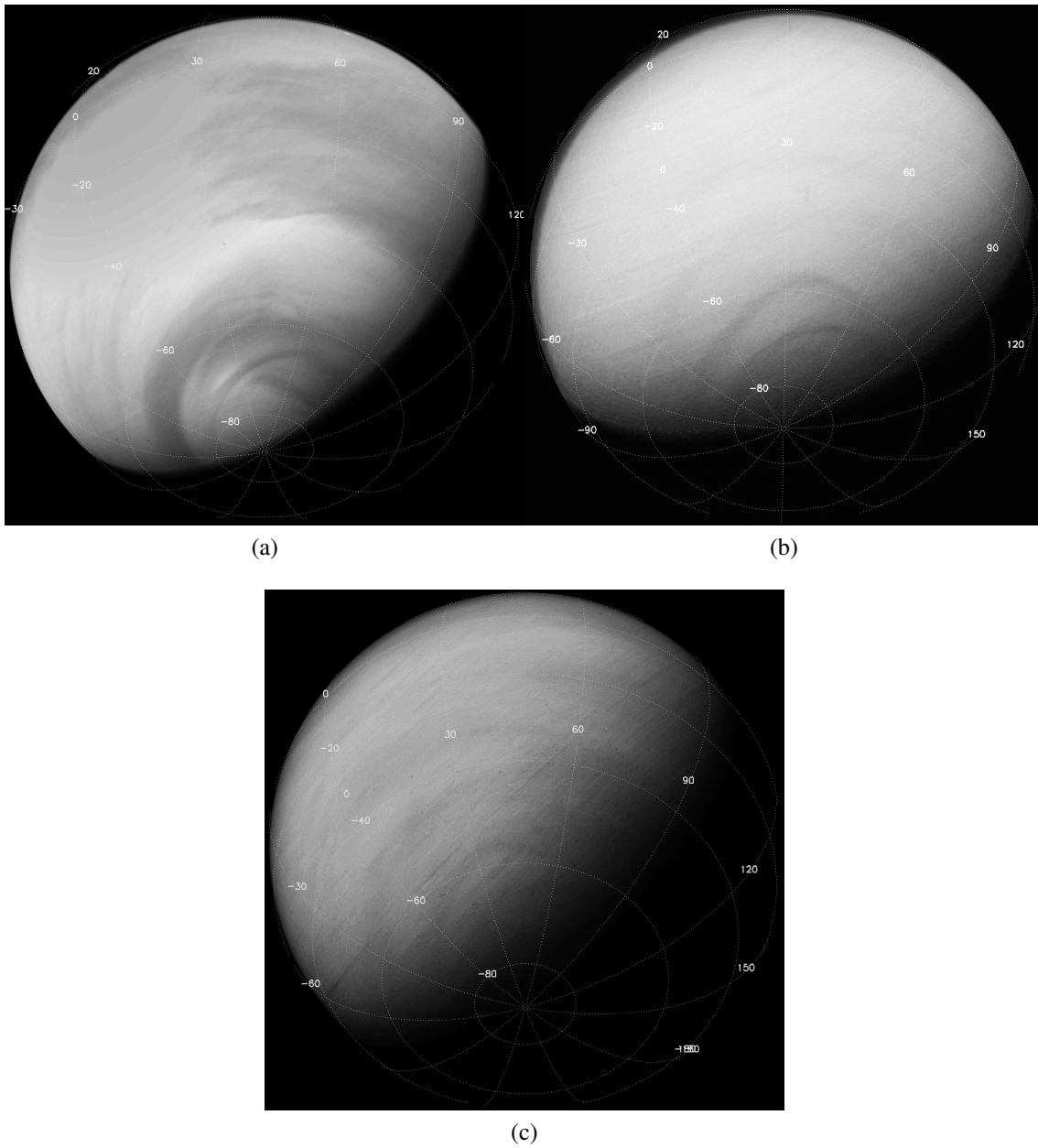


Figure 3.5: Channels compared: (a) UV, (b) VIS, (c) IR1 in orbit 439. (Image frames: (a) 0439_0021, (b) 0439_0024, (c) 0439_0026)

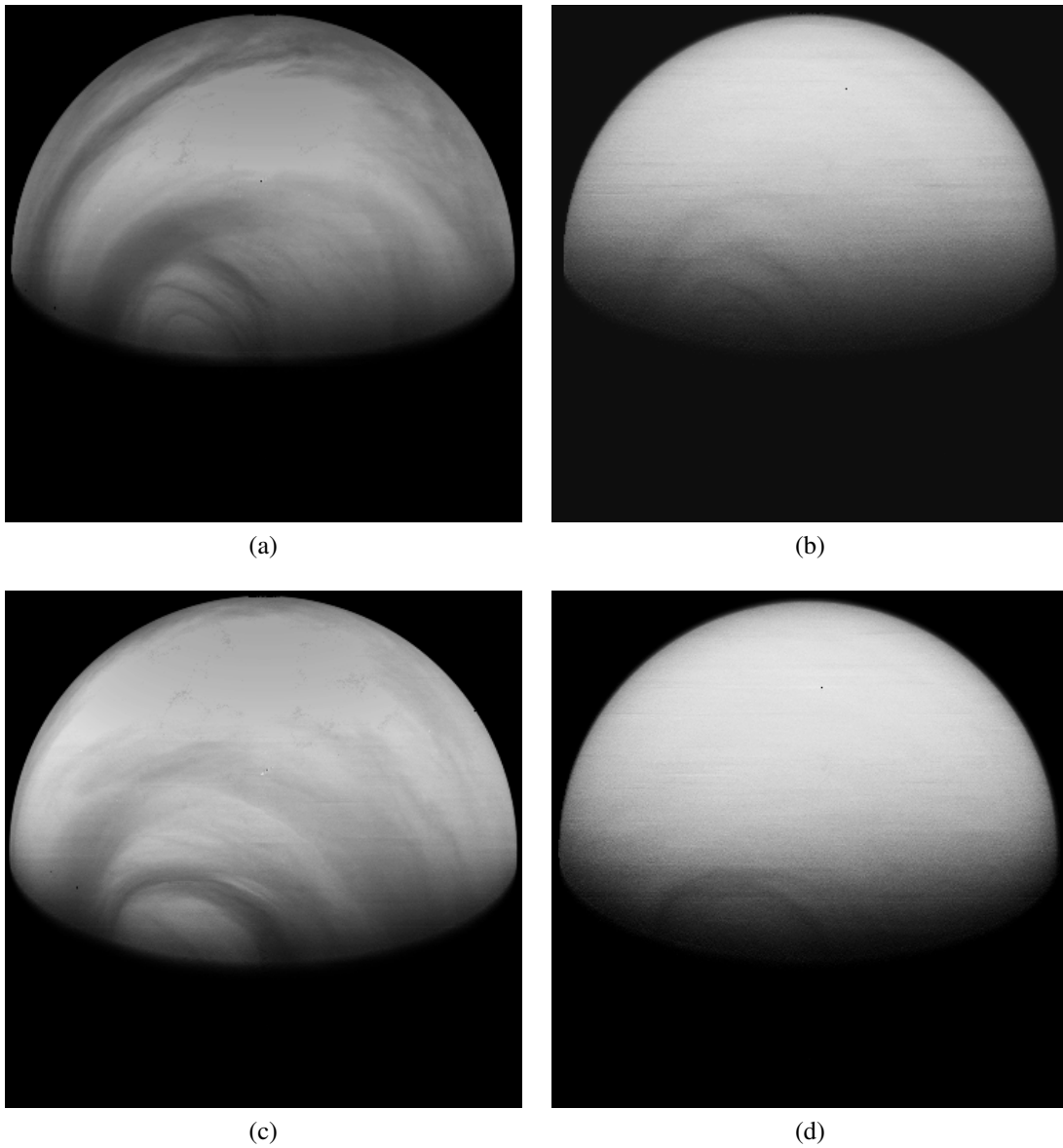


Figure 3.6: Channels compared: UV (left), VIS (right) in orbit 437 and 438. (Image frames:(a) 0437_0021, (b) 0437_0024, (c) 0438_0026, (d) 0438_0029)

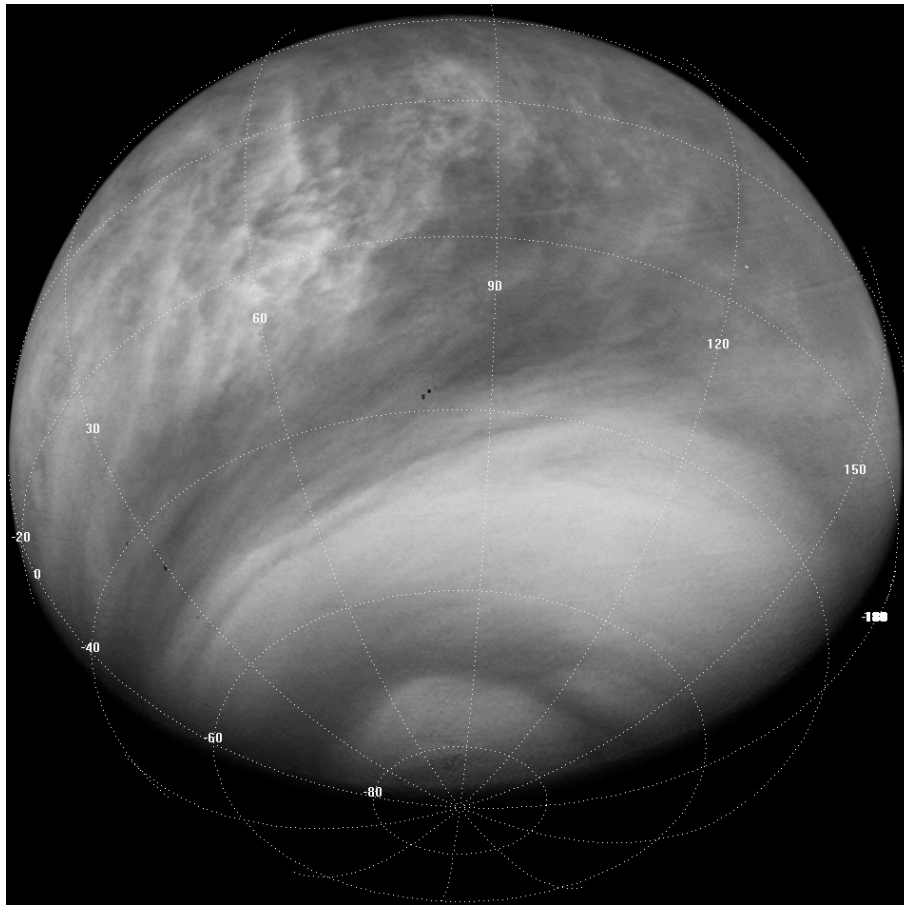


Figure 3.7: VMC off-pericenter image with coordinate grid. Grid lines are spaced by 20° for latitudes and 30° for longitudes. Cell structures are seen down to about 25° southern latitude. A prominent dark mid latitude band extends between $20\text{--}50^\circ$ S (Image frame: 0462_0030).

3.1.2.2 Off-pericenter observations of the southern hemisphere

The VMC images from the ascending branch of the Venus Express orbit (see fig.1.7) are the ones most comparable to the image data sets of previous missions with respect to image resolution and perspective on the planet. During the outer parts of the off-pericenter phase large parts of the southern hemisphere are in the field of view of VMC. As the spacecraft closes in, the planet begins to fill the whole field of view and southern mid latitudes as well as the northern equatorial regime are observed. Still, it is sometimes difficult to relate the VMC images from the off-pericenter (and pericenter) sections of the orbit to images from other Venus missions, due to the different observation geometries. The Venus Express orbit does not permit extended studies of symmetry properties between the hemispheres, since only small parts of the northern hemisphere are covered at a given time. Nevertheless, all known morphological features have been detected in VMC off-pericenter observation. Figure 3.7 shows a typical VMC off-pericenter image with a superimposed coordinate grid.

The **dark midlatitude bands** have been observed on a regular basis and VMC images show more detailed structure inside them than previous observations. On some occasions

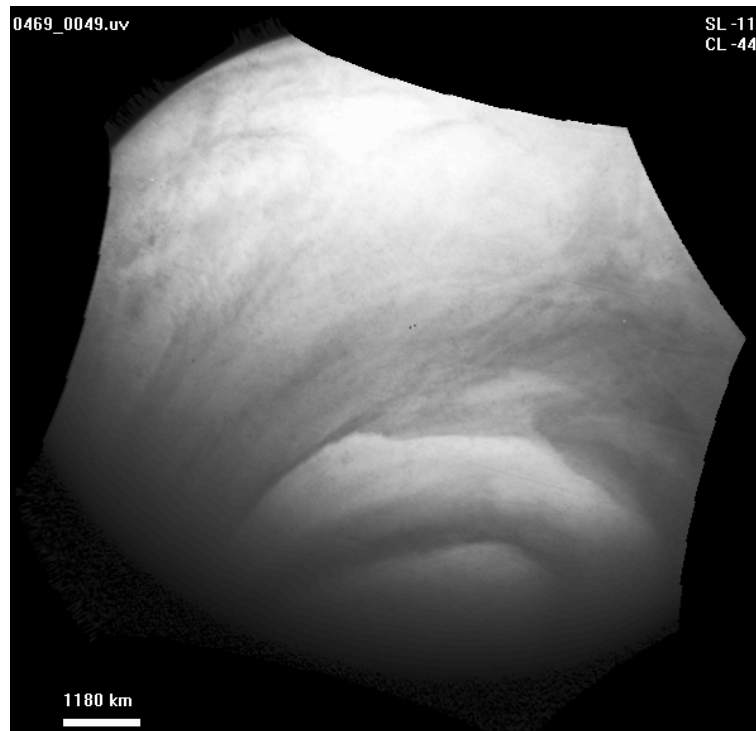


Figure 3.8: Overlaid structures in a mid latitude band. Numbers on top right indicate Longitude from sub solar point (SL) and latitude (CL) for the center point of the mapped image (Image frame: 0469_0049).

they appear to be composed of a more than one band superimposed on each other (see fig. 3.8, in the right part of the image). This indicates that the cloud deck is not observed at a narrowly confined altitude but that we actually observe motions at somewhat varying altitudes where cloud features move at different speeds. This has implications for wind speeds derived from cloud tracking. Since relatively strong vertical wind shears are known from Pioneer and Venera entry probe measurements to be present at the cloud deck (compare: fig. 1.4) this would lead to increased scattering of wind speed measurements at least in the mid latitudes. As will be seen later in the dynamics section this is actually the case for our wind measurements. Another interesting substructure are occasionally observed billow-like structures at the borders of some of the mid latitude bands which are reminiscent of Kelvin-Helmholtz instabilities. An example is given in figure 3.9. Kelvin-Helmholtz instabilities occur when velocity shear is present within a continuous fluid or at an interface of two fluids moving at different speeds relative to each other. The existence of large scale non-laminar flows implies relatively strong horizontal wind shear. Indeed these billow-like structures have been seen predominantly at $\sim 40\text{-}50^\circ$ S latitude. Where strong mid latitude jets are regularly observed. However, zonal wind speed profiles from VMC wind measurements do not show enough horizontal wind shear to account for Kelvin-Helmholtz instabilities. Therefore, a change in altitude between the dark and bright bands would be needed to account for the onset of non-laminar flow.

Circumequatorial Belts (CEB) are also commonly seen in VMC images, showing the same properties as in previous observations. The CEB's are extended longitudinally by several 1000 km (extending over the whole field of view of VMC in all images in

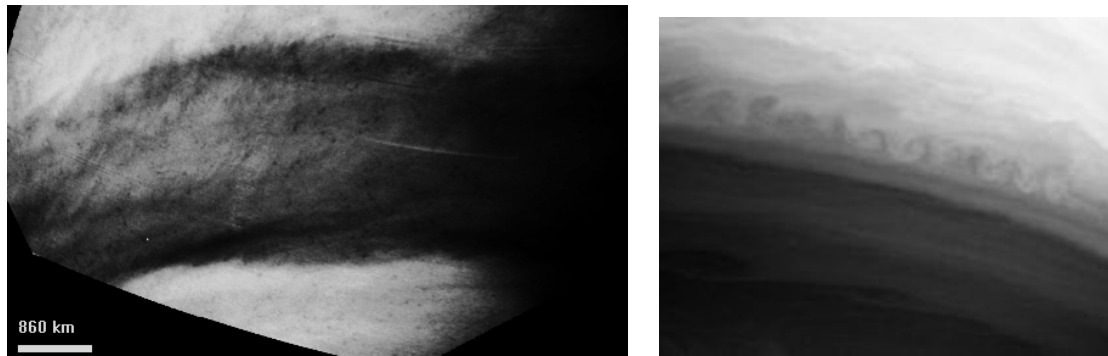


Figure 3.9: *Left*: Billow like structures at the edges of a dark mid latitude band observed by the VMC on Venus, especially in the upper left part. *Right*: Kelvin-Helmholtz billows in the atmosphere of Saturn (NASA, JPL). Image frame: 0472_0098)

which they are detected) and latitudinally by less than 50 km. In addition to the known CEB's VMC also observed similar UV-bright linear features in the mid latitudes, but with tilt angles matching or even exceeding those of the mid latitude bands (see figure 3.10). As the CEB's, also these tilted bar-like features seem to be tracers of gravity waves. In contrast to the CEB's they have not been detected in subsequent orbits, therefore it is not known yet if and how they propagate. One interesting detail is that they appear as dark features in the near-infrared, another property setting them apart from the CEB's.

3.1.2.3 Pericenter observations of the northern hemisphere

At distances of less than 10.000 km away from Venus, the VMC instrument has delivered images with resolutions from less than 7 km/pixel in the equatorial region to less than 1 km/pixel in the high northern latitudes. These resolutions have never been reached by any instrument before and therefore they provide new insights into the cloud deck morphology. Due to the very limited coverage on the planet, they can deliver only snapshots of the observed cloud features. Typical imaging sequences during pericenter passes allow for a maximum overlap of 50% between images in the equatorial regions and about 20-30% in higher latitudes.

The clouds of Venus show a great variability in appearance in the equatorial region with a nearly endless variety in shapes and sizes. Nevertheless certain regular properties can be identified even in this highly mutable part of the atmosphere. The largest structures present in the equatorial regime are the **bow-like waves**. As can be seen in figure 3.11 their appearance in VMC images is identical to earlier descriptions. They appear as alternating dark and bright streaks superimposed on the mostly cell-like cloud features with horizontal wavelengths of 100-150 km. At the equator their wavefronts are approximately perpendicular to the mean atmospheric flow, curving inwards roughly symmetric in both hemispheres. The bow-like waves are exclusively visible in the UV spectral range. Since the IR channels are detecting signals from deeper within the cloud deck, this implies that these waves are likely to be situated at or above the altitude at which the UV markings are observed. Alternatively, potential brightness variations in the IR could be too weak to be detected. No conclusive measurements exist on the contrast properties of the bow-like

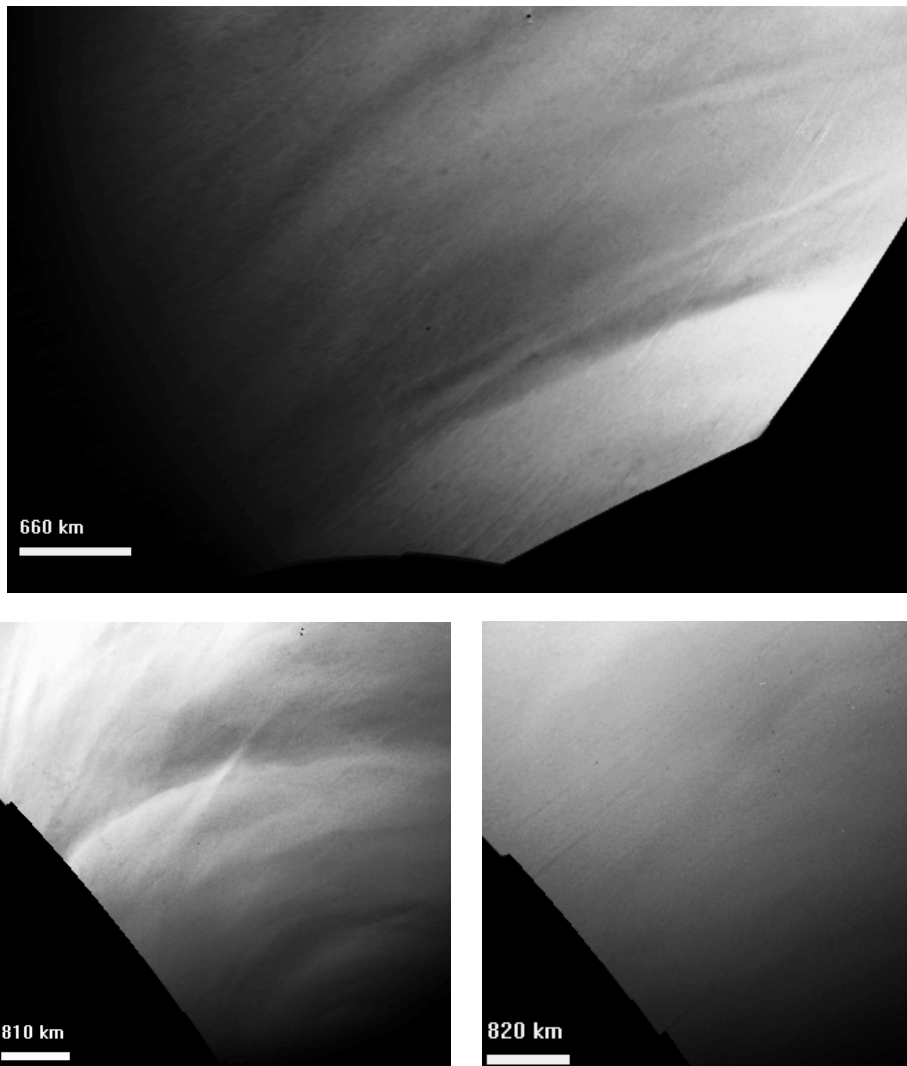


Figure 3.10: *Top*: Narrow bar-like features matching the tilt of a dark mid latitude band. *Bottom*: Bar-like feature with strong tilt, appearing bright in the UV (left) and dark in the NIR1 channel (right). Image frames: 0443_0078 (top), 0444_0034 (bottom left), 0444_0035 (bottom right).

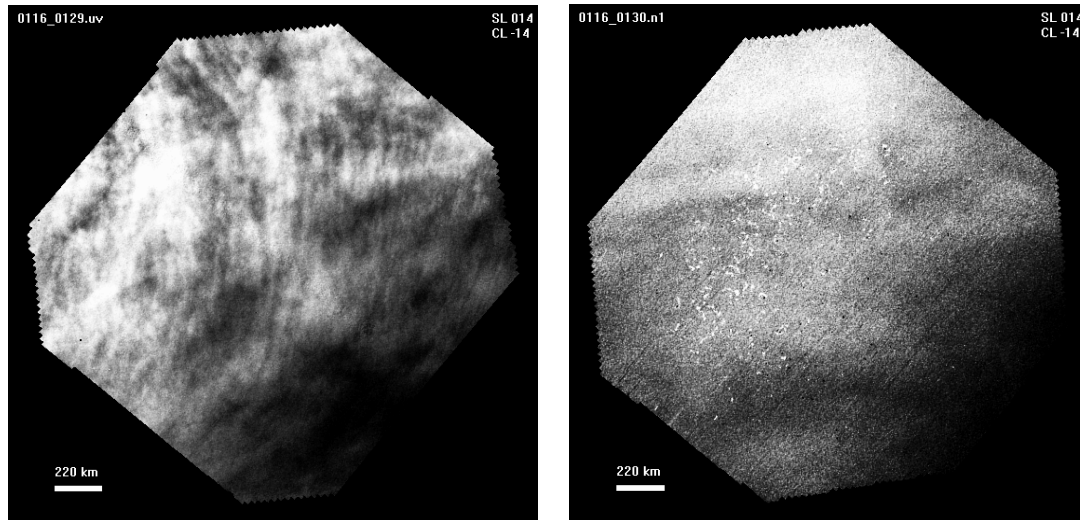


Figure 3.11: *Left*: Bow-like waves in the UV 14° upstream of the sub solar point (image centered 14° south of the equator). *Right*: The same region in the NIR1 channel, showing no traces of bow-like waves but streaks oriented with the mean flow (Image frames: 0116_0129, 0116_0130).

waves since the high contrasts of the simultaneously present dark UV markings (with usually 30-40% contrast) do not allow a clear distinction of which contrast variations are to be attributed to the wave patterns. However, on close inspection, the dark and bright UV markings seem to show a tendency to partial organization with respect to the bow waves on scales of ~ 50 km. It is unclear whether this is just a pseudo-correlation from simultaneous observation of different structures or a real physical interaction between the convective motion and the bow waves.

As was already discussed by Markiewicz et al. (2007b) the convectively generated **cell-like structures** in the near-equatorial region show small scale substructures inside the structures identified in earlier observations. As mentioned, the cells have been reported to have horizontal dimensions of 500-1000 km for the dark rimmed bright cells and 200-500 km for the bright rimmed dark variants (Belton et al. 1976b). These large scales seemed to be at odds with the presence of a vertically thin neutrally stable layer just below the cloud tops (inferred from Pioneer Venus and Vega in situ measurements) in which the convection is thought to occur. Confined to vertical dimensions of only ~ 5 -7 kilometers (Baker et al. 1998), the large horizontal scales would lead to diameter versus depth ratios of up to 100. Such a broad and thin convection would pose a severe challenge to the dynamics of convection. On Earth typical aspect ratios of diameter versus depth are only ranging between 10-30 (Agee 1987). Several attempts have been made to explain the observed cell sizes, for example with deep penetrative convection (Baker and Schubert 1992) or a combination of anisotropic eddy diffusion and radiative transfer effects (Covey and Schubert 1981). Figure 3.12 shows two examples where the larger bright cells are actually further divided by dark filaments into smaller sub-cells spanning only 30-120 km each. Assuming that the larger cell structures are actually clusters of the smaller ones and convection is happening on the scale of the substructures, aspect ratios would be as small

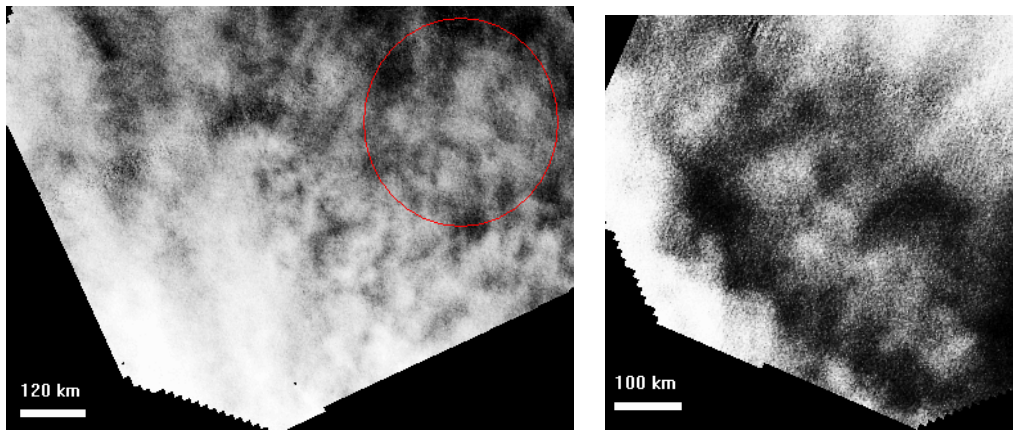


Figure 3.12: Substructures in so called “dark rimmed bright cells”. Images are from inside (left) and 35° downwind (right) of the sub solar region near the equator (Image frames: 0116_0120, 0042_0016).

as ~ 20 on average. This reconciles the dimensions of convective cells in the upper cloud layer of Venus with their terrestrial counterparts. In agreement with earlier observations the distribution of the cell features is ranging from about 20° upwind of the sub solar point as far as $\sim 40^\circ$ downwind. The latitudinal range in which the cell structures are present is approximately $\pm 25\text{-}30^\circ$ around the equator.

In addition to the known morphological features, a few new structures have been identified in VMC pericenter images of the equatorial region. Among them is one variety of cell-like features which show certain common traits (see Figure 3.13 (a)-(c)). Although varying in exact size and shape these slightly modified cell-like features are a regularly occurring phenomenon observed over a wide range of solar longitudes. Although they do not constitute a new kind of morphologic features, they share a whole set of properties which are observed in all occurrences of the phenomenon. Common properties of these cell-like features are:

- Centered in close proximity (within $\pm 5^\circ$ latitude) to the equator
- One or more cell like components with a bright inner part $\sim 50\text{-}100$ km in diameter surrounded by a darker rim
- Elongated dark “tails” to one or both sides of the cell like structure
- Dark filaments extending in all directions around the feature
- Total extension over 1000 km and more in length

It is not known how those “tails” and filaments connected to the cell-like features are generated. The filaments could possibly hint at up- or downwelling motions on large scales of 1000 km, thus implying the presence of deep convection which penetrates below the thin neutrally stable layer (Baker and Schubert 1992). However, they bear remarkable similarities in their shapes to evolved (weak) tropical cyclones over maritime climate on Earth.

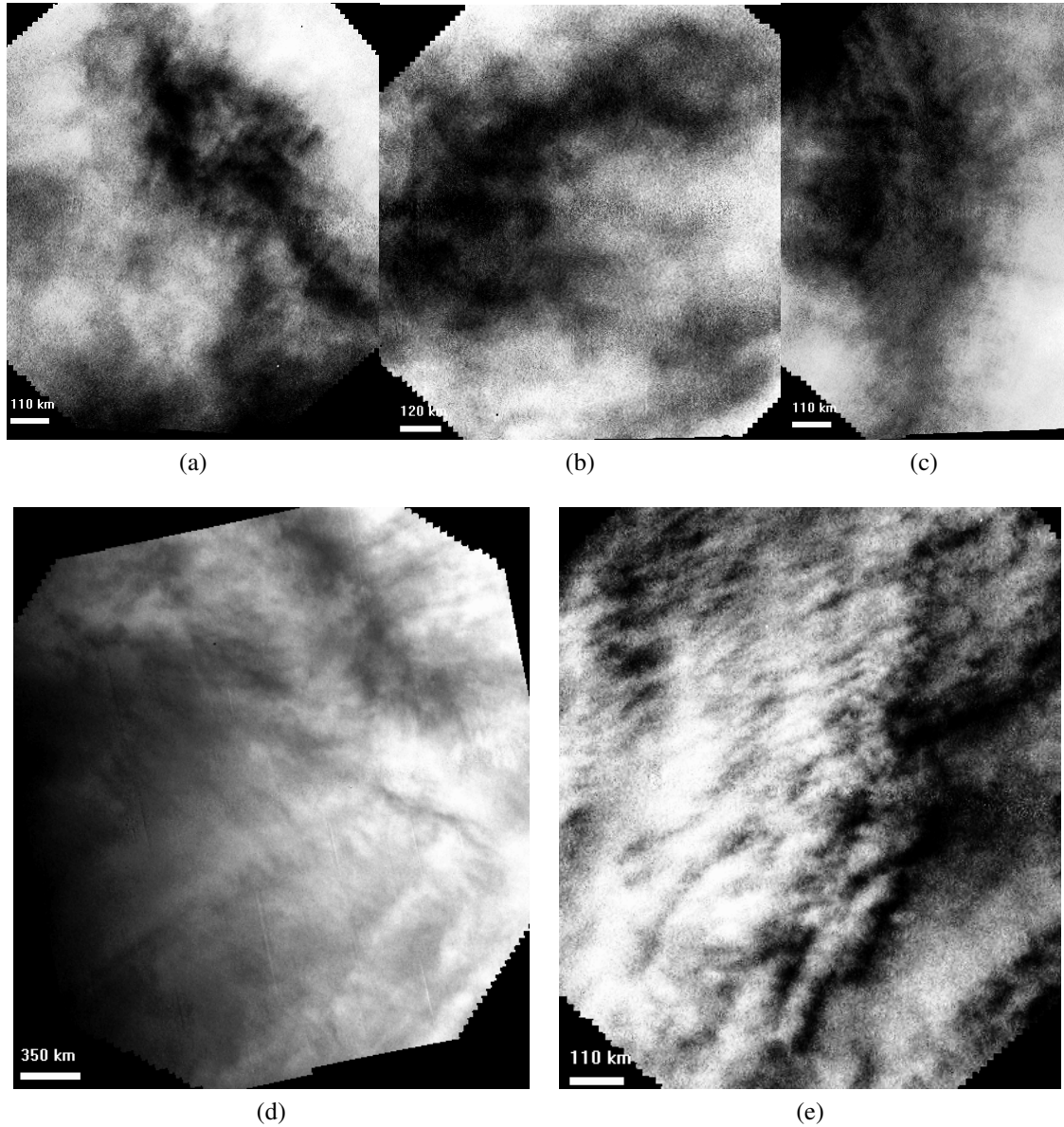


Figure 3.13: Newly identified recurring cloud patterns in the near equatorial region. Images (a) to (c) are centered exactly at the equator. Image (a) is situated 36° downwind of the sub solar point, image (b) 46° upwind and image (c) 27° upwind. Image (d) is centered 54° downwind of the sub solar point and at -14° latitude. Image (e) is centered on the equator and shows the region 40° downwind of the sub solar point, where cell patterns transform into more streak like patterns (Image frames: (a) 0149_008, (b) 0321_0125, (c) 0108_0123, (d) 0496_0117, (e) 0150_0088).

Images of the region about 40° downwind of the sub solar point (see fig 3.13 (d), (e)) regularly show fine streak patterns. In some cases they are composed of intricate filamentary patterns (d) or bundles of narrow, interrupted and zonally oriented streaks (e). The latter is strongly reminiscent of so called “cloud straits” of terrestrial clouds which form in the presence of weak convection in a strong wind flow, organizing themselves into “pearl-chain” lines oriented with the wind direction. This is exactly analogous to the conditions in the region where the image was taken: 54° downwind of the sub solar point the vigorous convection triggered by solar heating seems to have ceased almost completely, although some weaker turbulences possibly remain. In (d) actually another “modified” cell structure is visible in the upper right corner.

Approximately $30\text{-}35^\circ$ north of the near equatorial region, the mid latitude regime of Venus atmospheric dynamics is entered again. Most of the VMC images between $35\text{-}50^\circ$ show close-up views of the bow shapes and dark mid latitude bands. Wave-like disturbances, oriented perpendicular to the (tilted) direction of the bow shapes have been reported from Mariner 10 and Pioneer Venus observations of the cloud deck already. VMC has also seen these wave-like disturbances. Although they might be attributed again to a kind of gravity wave mode they display some ambiguous properties. An example of these wave-like disturbances across a dark band is given in figure 3.14 (left). In this case the disturbances are indeed cyclic, with a “wavelength” of ~ 45 km. But instead of co-aligned wave fronts these cyclic disturbances appear more like drawn-out streaks in one part of the feature and, again, like Kelvin-Helmholtz instabilities (compare fig. 3.9) in other parts. Despite the fact that these formations have been observed on several occasions, the process of their formation remains a mystery. A highly speculative attempt for an explanation of this phenomenon would be an assumption of a combination of vertical shear, causing the wave-like part of the pattern, and a simultaneous horizontal shear causing the more billow-like disturbances. But this scenario would require a complex and extremely special case of dynamics, so it seems rather unlikely. It has to be kept in mind, however, that we do not know about the vertical structure behind this pattern. If either the dark or the bright part of the pattern is situated above the other, the observed features could be the result of gravity waves in the higher layer. In this scenario the higher layer would be subject to a gravity-wave disturbance, possibly due to vertical wind shear or changes in altitude along the band. The change in pattern along the wave vector could then be attributed to gradual evaporation of the cloud droplets in this higher layer. An analogy for such behavior is frequently seen in lee-waves on Earth. But for this analogy to hold, the substance constituting the higher sheet would have to be more volatile than all substances known to exist in the cloud deck in enough abundance to form cloud formations. Therefore also this explanation does not seem very likely. A third speculation comes from another analogy to cloud features observed on earth. Fritts and Alexander (2003) ascribe the process of formation of the cloud structure seen in figure 3.14 (right) to convective rolls caused by braking gravity waves in a strong vertical wind shear environment.

CEB-like wave features have also been observed at high latitudes (see fig. 3.15 (e)). In addition to the known properties of the CEB’s, they also reveal substructures in high resolution images. In many cases they appear to be not one single stripe but rather like a parallel bundle of several narrower “wavefronts”. The number of wavefronts in CEB’s and their mid- to high latitude counterparts detected in the VMC high resolution images, varies between one up to about ten narrow parallel lines alternating between dark and bright.

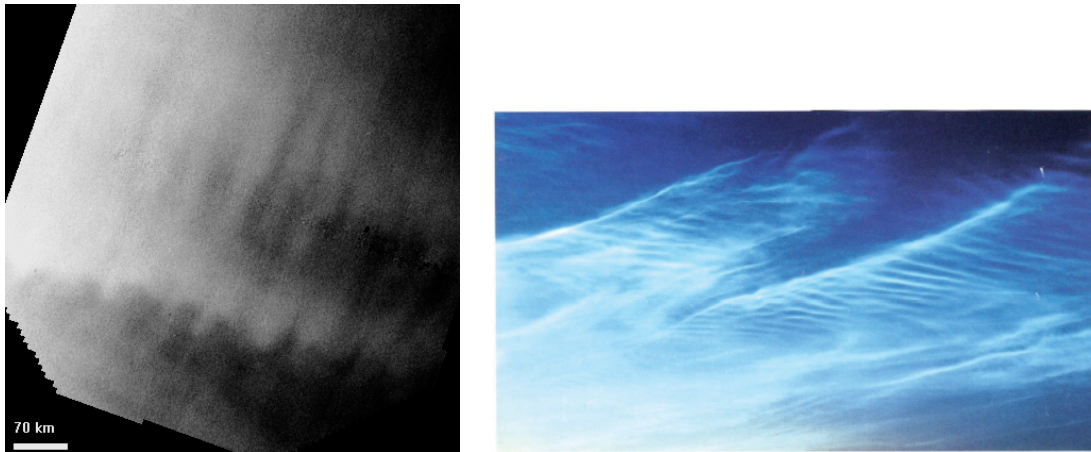


Figure 3.14: *Left*: Enigmatic wave-like disturbance pattern perpendicular to dark mid latitude streak. *Right*: Terrestrial cloud patterns formed presumably by streamwise-aligned instability structures (Image frame: 0383_0230, right image taken from: Fritts and Alexander (2003)).

Assuming that one full wavelength is represented by one bright and one dark stripe, the wavelengths of these substructures have been determined to values roughly between 7-14 km. Thanks to their long lifetimes of more than 24 hours and wide longitudinal extensions it has been possible to re-identify some CEB features in consecutive orbits and determine their latitudinal propagation speed. In agreement with previous measurements the CEB features were exclusively observed to move toward the south, propagating at velocities of $25 \pm 10 \text{ ms}^{-1}$ with respect to the surface.

These narrow elongated wave features appear to be representatives of one out of three classes of gravity wave features detected in mid to high latitude images of the VMC. As shown in figure 3.15 three qualitatively different species of wave disturbances can be distinguished. The first “small” type of waves (Fig. 3.15.(a) and (b)) is characterized by small apparent wavelengths of $5 \pm 2 \text{ km}$, organized in “patches” of parallel wavefronts in various states of alignment among individual patches. The term “small” refers to the broadness of the wavefronts which ranges typically between 10-40 km. The second “medium” type (Sub-figure (c)) of waves features longer wavelengths up to $\sim 20 \text{ km}$ and broader wavefronts, on the order of more than 100 km. Also the patches of medium-type waves show more alignment of their wave vectors among each other and extend further in length than the patches of small-type waves. The third “large” type (Sub-figure (d)) of waves shows a possibly bimodal distribution of $7 \pm 2 \text{ km}$ and $14 \pm 1 \text{ km}$. The large-type waves do not appear in patches, but as long and narrow bands of dark and bright stripes. Typically these bands measure about 40-100 km in the narrow dimension and extend the field of view of the VMC in all observed cases in the direction of the wavefronts. Therefore their extension in this dimension is most probably on the order of 1000 km or more. The large type waves are frequently accompanied by surrounding patches of small-type waves with various states of alignment with respect to the large wavefronts. Medium-type waves have not been observed in proximity to any of the two other types so far. Apparently CEB’s fall into the large wave category. All three wave types are usually observed in the vicinity of the borders between dark and bright streaks in mid- and high northern lat-

itudes. However, the CEB-like “variants” of the large-type waves show exceptions from this rule.

In an attempt to study the behavior of the identified wave types I did a statistical analysis of their observable properties, namely:

- Wavelength, defined as the combined length of one bright and one dark stripe measured perpendicular to the wavefront.
- Tilt angle, defined as the angle of the wave vector (perpendicular to the wavefront) with respect to the “west” direction on the planet.
- Latitude of approximate occurrence on the planet.
- Solar-relative longitude (or SRL), defined as the longitude of occurrence with respect to the sub solar point, negative values indicate positions downwind, positive values upwind of the sub solar point.

The results of this analysis are shown in figures 3.16 (distribution of wavelengths), 3.17 and 3.18 (scatterplots of properties). As mentioned before, the small-type waves have a common wavelength of ~ 5 km. They have been detected with the same wavelengths in all four VMC channels. The medium-type waves, which have been identified only in 5 orbits, show a broad wavelength distribution from 8-20 km. The bimodal wavelength distribution of the long type waves indicates an intriguing 2:1 ratio between the peak values of 7 km and 14 km, possibly hinting at the existence of two separate wave modes of this phenomenon.

Since wavelengths appear to be slightly different for the three wave types, I analyzed tilt angle, latitude and solar-relative longitude with respect to them (see Fig. 3.17). For the small type no correlation with any of these properties as a function of wavelength was found in a global respect. However, looking at individual orbits they exhibit a tendency to an increasing tilt angle as a function of latitude. The position of occurrence of the small waves shows a correlation between solar-relative longitude and minimum latitude (Fig. 3.18). Their tilt angles seem to be confined within a range of $0-45^\circ$.

In contrast, the few observed occurrences of medium-type waves suggest a correlation of all three properties with wavelength. It appears that the medium-type is present with smaller wavelengths in lower latitudes on the morning side of the planet, possibly developing into longer wavelengths at higher latitudes and increasing in tilt angle (at least) toward noon. Only one medium-type wave was observed on the afternoon side (negative longitude, relative to the subsolar point), therefore no statement can be made about the progression of correlations on the afternoon side. The correlation between wavelength and tilt angle of the medium waves is almost perfectly linear (with one exception for the smallest observed wavelength). Tilt angles of the medium waves do reach high values up to 120° . The lowest observed tilt angle is 20° . The low number of observed occurrences leaves all these results preliminary. Further observations are direly needed to enhance the statistics of this type of wave-features.

Finally the long type waves do not show correlation between wavelength and tilt angle, but the longer wavelength “mode” seems to occur preferentially at higher latitudes and in the afternoon, whereas the short wavelength “mode” is more often observed on the

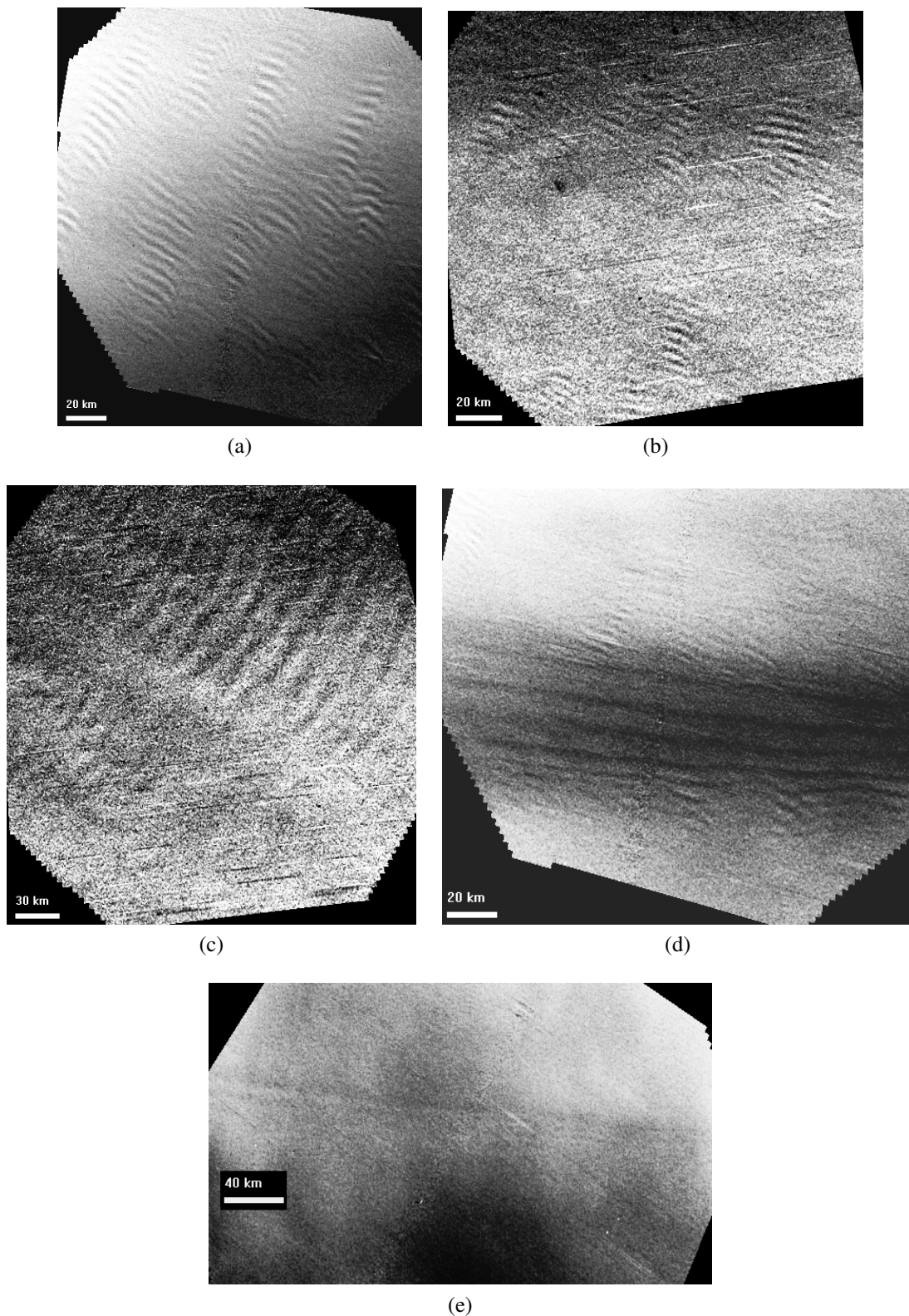


Figure 3.15: Different classes of wave patterns at middle to high northern latitudes between 40-70° S. “Small” type waves observed in the UV (a) and NIR1 (b) channel in different orbits. “Medium” type waves (c) with tilt angles larger than 90° with respect to the “west” direction in UV. “Large” type waves (d), surrounded by small waves in UV. Circumequatorial Belts (e) seem to belong to the large wave type (Image frames: (a) 6442_0068, (b) 0243_0048, (c) 0242_0034, (d) 0442_0067, (e) 0441_0112).

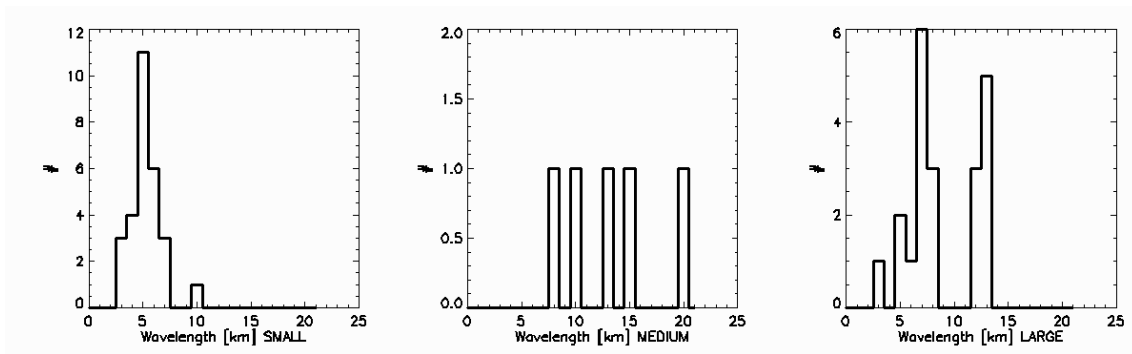


Figure 3.16: Size distribution for the small-type waves (right), medium-type waves (center) and large-type waves (right).

morning than on the afternoon side. Tilt angles for both modes are always lower than 40° and shows an apparent trend to increase from morning to afternoon.

Common to all three types is a clear correlation of lowest observed latitude with respect to solar-relative longitude. They were observed at minimum latitudes around 50° on the morning side, steadily increasing to $\sim 65^\circ$ on the afternoon side. Although this correlation seems to link the wave phenomena even further to the dark and bright polar bands (which, due to their average tilt angles, also often appear to progress from lower toward higher latitudes with solar-relative longitude), this could be a selection effect due to a more frequent coverage of lower latitudes on the morning side by VMC imaging sequences and should be regarded with caution.

Now the really interesting question after all these comparisons is: Can we learn something about these mysterious waves? One clear conclusion is that all three types represent different physical processes, since their observable parameters vary distinctly from each other. Large and small waves, often appearing in direct vicinity to each other, are likely to be linked by a common source triggering them. Medium waves on the other hand seem to be either originating from a different source, or at least require some other conditions to develop than the other two types.

The observed contrast values range from $\sim 3\text{-}4\%$ in all four channels for the waves. Due to these low values and the fact that the contrasts are approximately the same in all channels, it is extremely unlikely that they are being caused by vertical mixing of H_2SO_4 and the UV absorber. A more likely explanation are density variations in the clouds. Areas with higher aerosol densities would show up as bright stripes and areas with lower aerosol density as dark stripes. The assumption of cloud density variations is in agreement with the matching contrast levels in all four channels. The fact that the observed wavelengths also do not vary between channels proposes that the waves might be detected at roughly the same altitude level. However, the average resolution of ~ 350 meters per pixel and the relatively low signal to noise ratio (noise levels are approximately 1% variation of the mean signal level), further limiting measurement accuracy to ~ 3 pixels, might not be enough to resolve variations of less than 1 km in wavelength between channels. Therefore it remains possible that the wave features are indeed being observed on different altitude levels in the UV and the IR channels. The main mechanism to produce such density variations are gravity waves.

Now, what could be the possible source for these gravity waves? A review on the

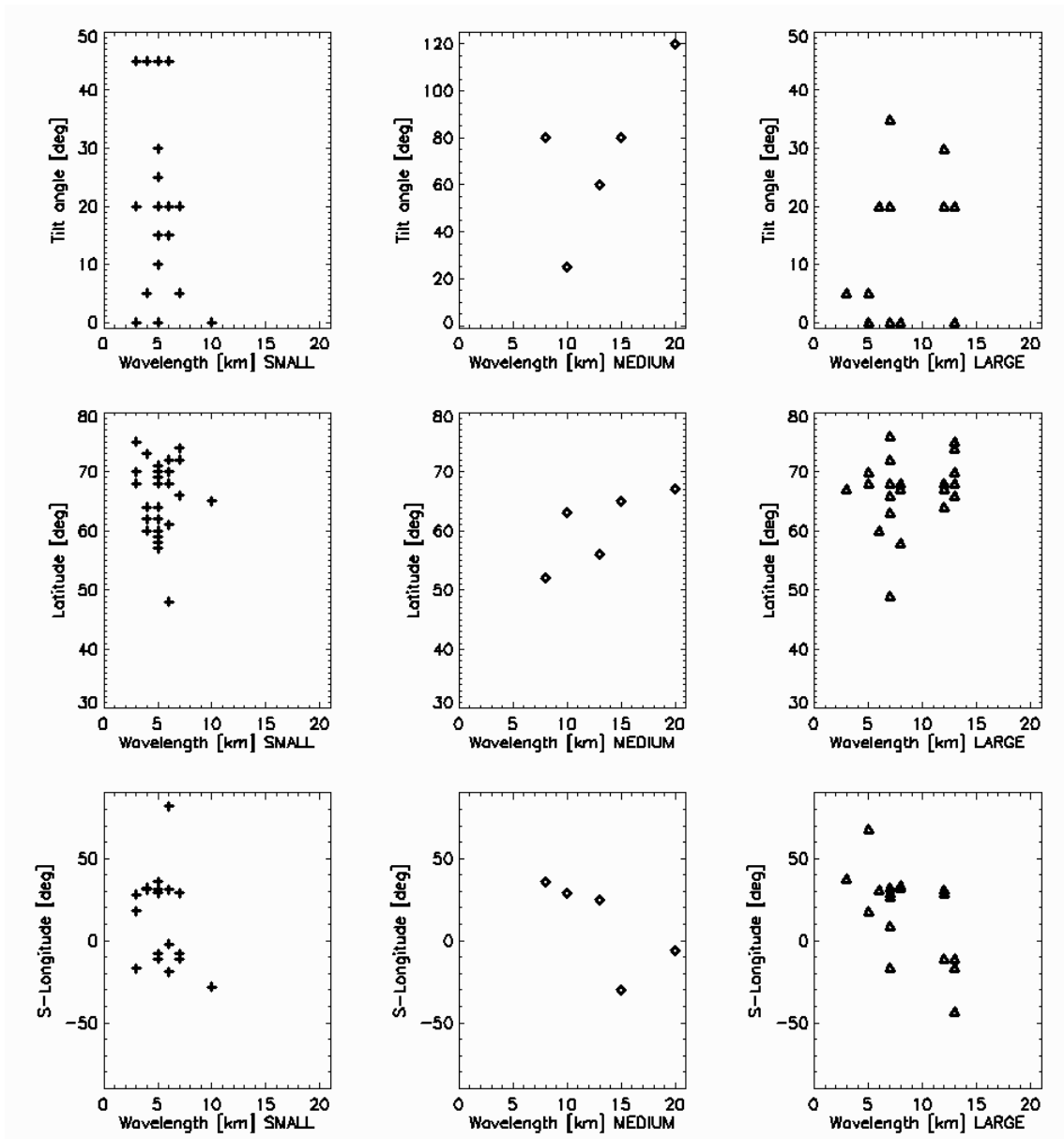


Figure 3.17: Different properties (top to bottom) of the three wave types (left to right) with respect to wavelength.

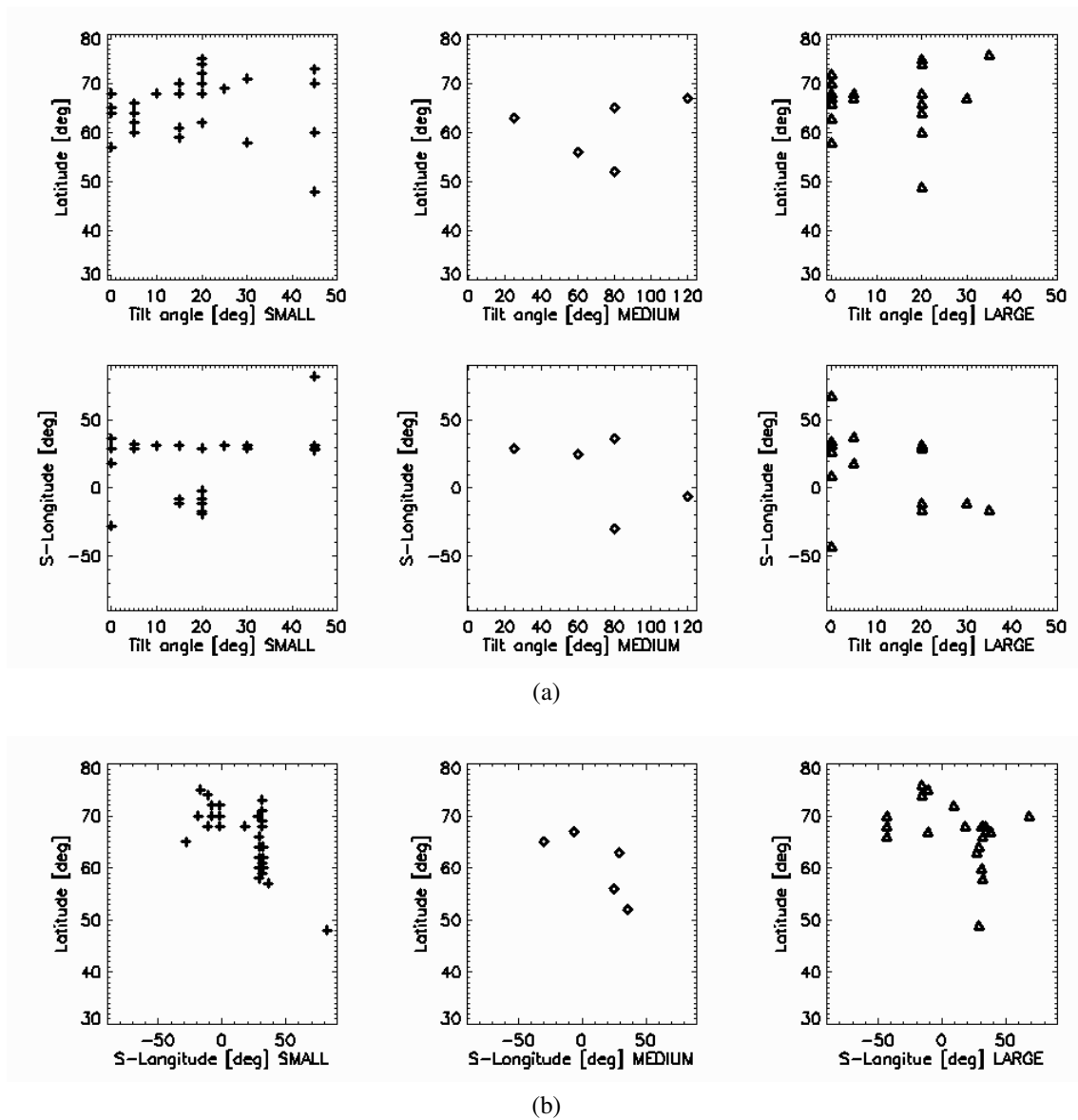


Figure 3.18: Tilt angle distributions with respect to Solar longitude and latitude of occurrence (a) and solar-relative position on the planet (b) for each of the three wave types (left to right).

physics of gravity waves by Fritts and Alexander (2003) lists topography, underlying convection and wind shear as sources for gravity waves in the middle atmosphere. Topography can be ruled out almost immediately, since the observed horizontal wavelengths are 1-2 orders of magnitude smaller than would be expected and the altitude of the observed waves is far too high above the surface to be dynamically linked to the underlying topography. Wind shear remains a possible source, since latitudinal wind profiles show a relatively steep decrease of zonal wind speeds toward the pole in high latitude regions. But the most likely process causing the observed high-frequency gravity waves is underlying convection. McGouldrick and Toon (2007, 2008) describe the existence of strong localized density variations (so called “holes”) within the main cloud deck of Venus. These holes, generated from radiative evaporation of cloud aerosol at the cloud base, can lead to convection within the neutrally stable layer below the cloud tops. Gravity waves would form as a result of air parcel displacement while flowing past overshooting convective plumes. Recent VIRTIS data also confirmed the existence of localized convection inside the clouds (G. Piccioni, private communication). Since these holes appear to trigger convective “rolls” with extensions of more than 1000 km in length, the large-type waves seem to be the primarily triggered waves by this convection. The small-type waves may be a secondary effect, created by breakup of the large-type waves. This generation of so called “secondary gravity waves” by breakup of convectively generated gravity waves has been studied and modeled for Earth’s atmosphere (Lane and Sharman 2006). One indication for this is the fact that they are frequently seen directly “attached” to the large-type waves, apparently emanating away from them in both directions.

The question remains why the mid type waves are so different from the small and large types. Due to the extremely small dataset of only 5 observations no definitive answer can be given on that account yet. They may just be a variant of the small waves, developing in different boundary conditions.

3.2 Dynamics

The second main topic of this thesis is atmospheric dynamics in the cloud top region of Venus, concentrating on the questions already mentioned in the introduction chapter. The main method of data retrieval for the cloud top dynamics was tracking of the movements of cloud markings in image sequences from the UV channel of the VMC. A very general impression of the rotation of the atmosphere can be obtained from apocenter imaging by observing the motions of large scale features such as polar and mid-latitude bands. More detailed insights are provided by tracking of intermediate and small scale features in off-pericenter branch imaging.

In the very beginning of my work for the thesis, before I started with the tracking of UV cloud markings, I did a first and rather qualitative study of the orbit-by-orbit change of the appearance of the cloud features in apocenter observations. An example for a typical evolution of the evolution of large scale cloud markings, over the course of six orbits, in high latitudes observed from apocenter is shown in figure 3.19.

The first attempts to get an impression about the general global circulation were done in two ways. One attempt was to find the best match between patterns in a series of subsequent orbits. This approach led to a crude estimation of a rotation period of ~ 3 days

for best matches among features in the near-polar region and about 4-5 days for features in the middle latitudes. These values are roughly in agreement with later, more precise measurements from cloud tracking (presented later in this section), but far too inaccurate to achieve reliable information about the global rotation.

A second attempt was to identify the semi major axes of ellipses formed by the innermost dark polar bands in subsequent orbits and derive their average rotation speeds. In some cases, where a well-defined ellipse shape could be identified, this approach yielded rotation periods between 2.6 ± 0.2 and 2.75 ± 0.2 days which are basically consistent with the regularly observed near-polar rotation period of ~ 2.7 days (Schubert 1983). Examples for well-defined elliptical shapes of dark polar bands are seen in figure 3.19.(a) and (f). In most cases however, the dark polar bands deviated too much from elliptical shapes to identify a semi-major axis (for example in configurations like in sub-figure (e)). There the attempts on measuring rotation speeds over several orbits produced results anywhere between 2 to 5 days of rotation periods for the near-polar region.

After these first qualitative attempts I focused on the tracking of small and medium scale UV markings in image sequences from apocenter and off-pericenter observations.

3.2.1 Tracking methods

Two general approaches were followed for the tracking of the UV cloud markings to derive wind speeds from image sequences. The first is manual (or “visual”) tracking of cloud features, conducted by human experimenters. The second is automatic (or “digital”) tracking, executed by a pattern recognition algorithm. The visual tracking efforts are further split into two different tracking techniques, the so-called “parallel method” and the “sequential method”.

The first step in all cloud tracking methods was to establish navigation for the utilized images. I used the post-processed SPICE kernels to calculate VMC boresight vectors and their intersection with the cloud layer. The SPICE kernels are a database for high resolution navigation and orientation data for spacecraft and celestial bodies, hosted and maintained by NASA-JPL, in cooperation with the ESOC flight dynamics department for Venus Express data and DLR for VMC-specific informations (for further reference, please visit: <http://naif.jpl.nasa.gov/naif/>). Once the observation geometry has been determined, the positions on the cloud deck are calculated for each image pixel. For these calculations, the cloud top height was set to a fixed value of 70 km above the planetary surface for navigation purposes. The actual altitude of the UV markings is expected to vary by about ± 5 km around this level, which only results in negligible uncertainties in coordinate determination.

The use of two different visual tracking methods is owed to historical reasons and limited software compatibility. But even though the use of variant methods increases the necessary effort and caution of comparing and combining their results, it allow for a possibility to cross-check potential systematic errors in either method.

The **sequential method** traces back to the wind speed measurements from previous missions, especially from Pioneer Venus OCPP observations (Limaye and Suomi 1981, Limaye et al. 1988, Limaye 1988). Basically, the same method and tools have been used as for the cloud-tracked vectors derived from the OCPP data. In particular, a loop of an entire image sequence from one VEX orbit was displayed in either rectilinear (latitudes

3 Results

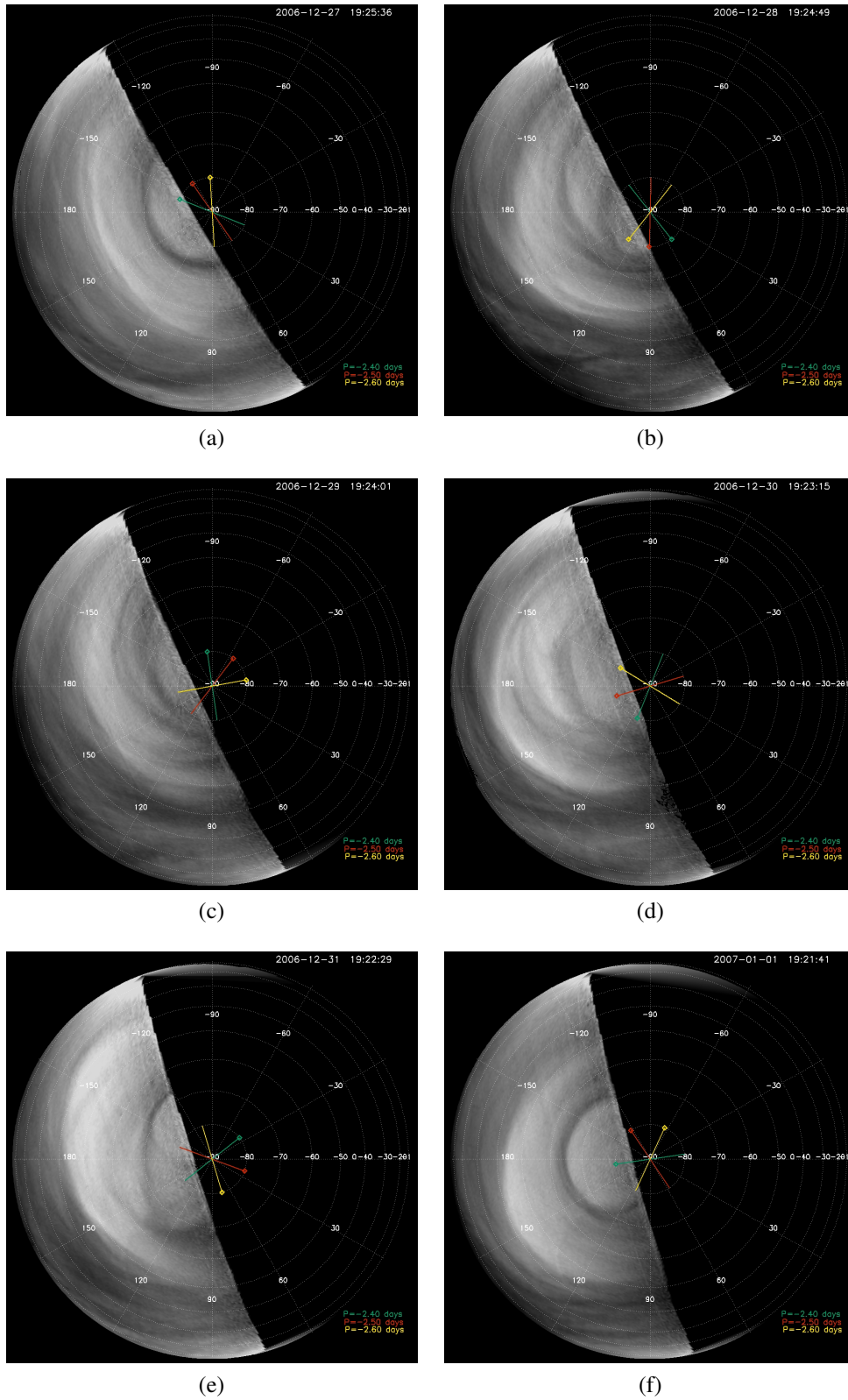


Figure 3.19: Images taken close to the apocenters of orbits 250 to 255 intervals of ~ 24 hours (Image frames: (a) 0250_0064, (b) 0251_0055, (c) 0252_0063, (d) 0253_0063, (e) 0254_0040, (f) 0255_0040).

and longitudes are forming orthogonal, regularly spaced lines) or polar projection of the images into a fixed coordinate frame. In both cases the angular resolution was set to a value of 0.2° . Figure 3.20, shows an example of a VMC image in rectilinear projection. In this method, the motion of a cloud feature is observed in the way of a short movie clip, giving the experimenter an overview of the path of a selected cloud feature as well as the global pattern of motion. After familiarizing with the general flow pattern the experimenter puts small markers on distinctive cloud features in one image from the given sequence. Then the loop is continued, switching to a later image from the same sequence. There, another group of markers is put on the same (re-identified) cloud features. These steps are then repeated until the selected cloud features have changed significantly from their initial shapes and sizes and cannot be identified anymore. To enhance visibility of the cloud features, a contrast enhancing high pass filter was applied to the images after care was taken that the filtering did not alter any other image properties. This method was the main tool I used for the retrieval of wind vectors. The software tools I used during the tracking process were refurbished from existing software modules which had been originally developed for tracking of UV cloud features in OCPP data.

The **paired method** is a straightforward approach in which two different images from the same sequence are displayed side by side on a monitor and the cloud features in both are observed and compared simultaneously. Also in this method, markers are set in order to track the corresponding points of cloud features in the compared image pairs. One significant difference is that here the images did not undergo any filtering, contrast enhancement or projection. Thus, basically unaltered VMC images were used for tracking with this method. The images were only slightly resized in order to achieve an approximately constant display size of the planet in each image. The paired method was used mainly by Igor Khatuntsev from IKI, Moscow. I also used this approach for wind tracking in several orbits, mainly to compare results from the same orbit and observer with respect to potential method-specific bias effects. The outcome of this test was that in low to mid latitudes no differences in wind speeds were found but in high latitudes the paired method delivers characteristically lower wind speeds than the sequential method.

Although the basic principle –visual correlation between two images– is the same in both approaches, there are subtle but important differences. In the first case the observer tracks clouds by blink comparison between two images, trying to follow the displacement of the tracked features on a fixed coordinate grid. In the second case the tracked feature is seen in both images simultaneously, thus emphasizing visual pattern recognition. A somewhat subjective addition: during the tracking process the sequential method is similar to the attempt of keeping a moving object in focus. The paired method contrasts to this essentially by the process of shifting the visual focus back and forth between two separate objects.

In both visual methods, a great variety of feature types have been tracked. Basically all features that did not span on a globally significant scale were used to track the cloud movements. We did not differentiate between bright and dark features, tracking both alike. The main criteria for feature selection were as follows:

1. Significant, well discernible contrast between the feature and its immediate surroundings. No fixed criterion was applied but the vast majority of tracked features had contrasts in excess of 15% with respect to their surrounding.

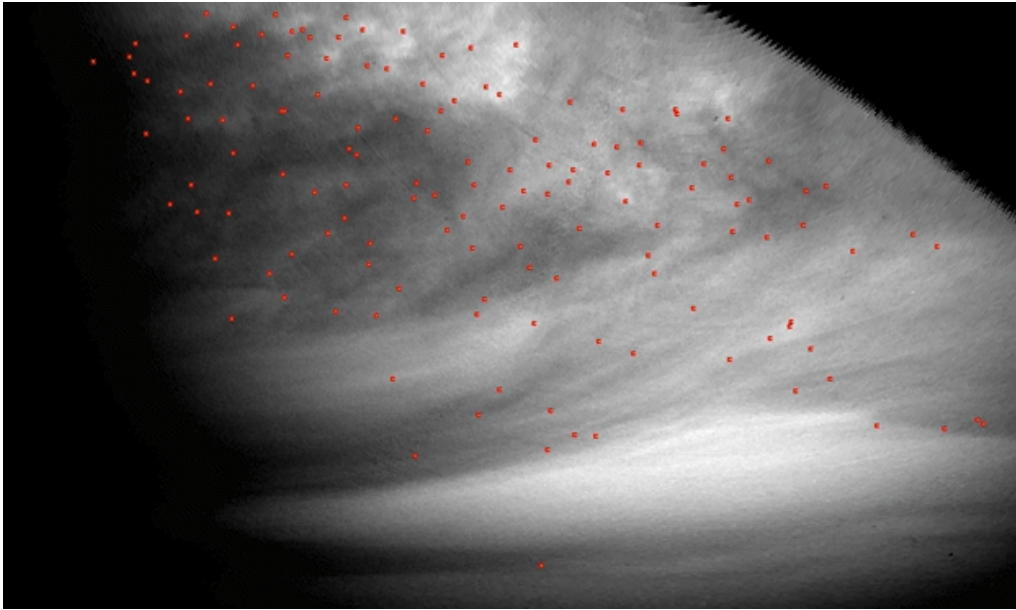


Figure 3.20: Typical VMC image used for wind tracking purposes. The image in rectilinear projection, where latitudes and longitudes form a rectangular coordinate grid with a resolution of 0.2° in both directions. The markers on the projected image represent actual tracking markers, set in the process of the sequential tracking method.

2. Features size of 100-3000 km that allows for reliable identification of the feature center (sizes depending partly on image resolution).
3. Prominent shapes like protrusions or clearly edged parts of boundaries for larger features.
4. Minimum time intervals between images were chosen to allow for resolving wind speed differences of about $10\text{-}20 \text{ ms}^{-1}$ (depending on image resolution).
5. No features from the limb regions were used because they are subject to foreshortening

The wind speeds in both methods were derived in similar ways. After the navigation data was linked to the images (for both, the projected and unprojected images), latitudes and longitudes of the respective marked pixels were extracted for all measurements of the sequence. From these values and the time intervals between images the zonal and meridional wind speed components were calculated as:

$$u(\lambda, \varphi, t) = \frac{\Delta\lambda \cdot R_C}{\Delta t} \cdot \cos \varphi ; \quad v(\varphi, t) = \frac{\varphi \cdot R_C}{\Delta t}$$

Where u and v are zonal and meridional wind speed components, $\Delta\lambda$ and $\Delta\varphi$ are longitudinal and latitudinal displacement between images, R_C is the distance from the planetary center to 70 km above the surface ($R_C = 6121.8 \text{ km}$) and Δt is the time between images.

For the digital cloud tracking in the VMC images we used the same algorithm as described by Rossow et al. (1990). The digital analysis was performed systematically in

pairs of images with at least one hour time difference. It uses cross correlation between quadratic sub-arrays containing signal level patterns (targets) as a metric, with a “cloud” target of 10 x 10 pixels in the first image ($2^\circ \times 2^\circ$ latitude by longitude) and a larger (parameter dependent sized) search window in the second image. The displacement between the target location in the first image and the location of the maximum cross correlation coefficient between the target pattern from the first image and the search window in the second image was taken as the best estimate of the movement of the selected target over the interval between both images. The displacement over the two images leads again to the determination of the zonal and meridional components of the cloud level flow. The search window size, in pixels, was set to a window equivalent to a maximum flow of $\pm 100 \text{ ms}^{-1}$ in the meridional and -200 ms^{-1} in the zonal direction, accounting for the time interval between the images. The digital tracking so far produced a set of $\sim 205,000$ vectors, obtained from images acquired in nine orbits (30, 31, 34, 38, 46, 51, 56, 60 and 61). Preliminary results from orbits 262-267 have already been presented by Markiewicz et al. (2007b).

From the resulting set of vectors, latitudinal and/or longitudinal wind profiles and maps in both directions can be determined, by averaging all wind vectors inside a defined latitude/longitude bin. From the average spatial density of retrieved vectors per orbit, I decided to use latitude bins of 5 degrees and longitude bins of 7.5 degrees (corresponding to 0.5 hours of local solar time) in order to maintain good levels of statistics in each bin.

3.2.2 The dataset of wind vectors derived from wind tracking

The tracking data and derived results presented in this section are based on image sequences obtained between $\sim 60,000 - 26,000$ km distance from Venus, corresponding to image resolutions of $\sim 20-45$ km per pixel. Typical time intervals between images inside a sequence used for cloud tracking are ~ 40 minutes, equivalent to a displacement of cloud features between the images of 5-10 pixels. This timing of image sequences represents a compromise between a minimized error in velocity measurements ($\sim \Delta t^{-1}$) and maximized temporal resolution of the observations. Coverage on the planet, regarding tracked UV markings, ranges from about 10° N to 80° S in latitude and from 8 to 16 h local solar time. The contrast in the VMC UV images varies between 5% and 30%, with typical values of 15-30% for the tracked features.

In the off-pericenter branch the VMC observes middle and low latitudes in nadir geometry. Local time coverage depends on the sub spacecraft longitude, which slowly changes from one orbit to another by $\sim 1.5^\circ$ (or 6 minutes local time) per day. The off-pericenter branch images are predominantly used to track winds from medium and small scale features, ranging from several thousand down to several hundred kilometers in diameter. As the spacecraft approaches closer to the planet, cloud features on scales down to few tens of kilometers in size can be identified in the images. However, at distances closer than 10,000 km, the acquisition of wind tracking sequences becomes increasingly more difficult as the rapid motion of the spacecraft decreases the possible overlap between images and features can be kept in the field of view only for short times.

Figure 3.21 shows the distribution of wind vectors obtained from VMC cloud tracking in the latitudinal and local time directions. In total, about 20,000 vectors have been extracted from ~ 450 image pairs. Their distribution over the covered regions of the southern

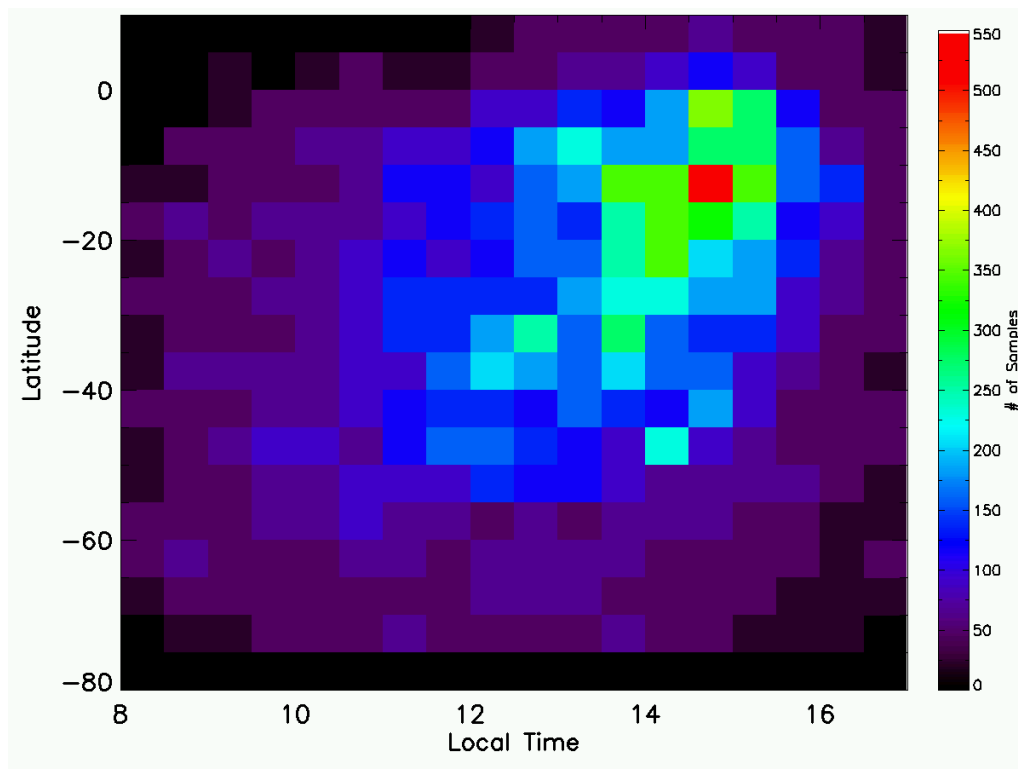


Figure 3.21: Distribution of VMC cloud-tracking vectors in bins of 5° latitude by 0.5 hours local solar time.

hemisphere is not uniform. The number density of retrieved vectors per 5° by 0.5 h local solar time bin shows a pronounced peak just downstream (to the west) of the sub solar region where a large number of well-discernible features of convective origin (e.g. cell-like features) is regularly observed and drops toward higher latitudes as well as toward the morning and evening terminator regions. The main limiting factor for coverage in local time is toward the dusk and dawn regions. There the steep brightness gradients of solar illumination dampen the contrasts of the UV markings, even in images with brightness corrected for solar incidence angle. At polar latitudes the morphology of the clouds is different altogether, presumably due to the decrease in, or even absence of, convective activity and presence of sub-micron haze (Kawabata et al. 1980) above the altitude of the UV markings. This results in a lack of discrete features, very low contrasts and drawn-out diffuse feature boundaries.

During the primary mission, the descending off-pericenter branch of the Venus Express orbit was reserved for data transmission to Earth. In conjunction with the relative change in local solar time of the orbit plane, this lead to separation of the VMC wind tracking data into three periods in which it was possible to observe the day side of Venus in the ascending off-pericenter branch from a sufficient distance. These three periods are separated by gaps of almost 140 orbits in which VMC was pointed either to the night side or too close to the terminator to allow for tracking sequences to be taken in the required orbit segment. The first period spans from orbits 29 to 72 (containing tracking sequences from orbits 29, 30, 31, 34, 38, 46, 51, 56, 60, 61, 72, during May-June 2006), the second period from orbits 208 to 295 (containing 208, 210, 230, 246, 250, 257, 258, 260, 263,

265-267, 279, 281-284, 295, during November 2006-January 2007) and the third period from orbits 439 to 530 (containing 439, 440, 442, 453, 460-463, 469, 471, 530, during July-September 2007).

As is evident from the list of orbits, the individual wind tracking sequences are separated from each other by several days in most cases. But also sets of up to 4 consecutive orbits are present in the data set. These irregularities in coverage were partly compensated by the fact that the field of view included a broad range of local times during imaging sequences at distances above 40,000 km.

3.2.3 Comparison of results from different methods

As is obvious from Figure 3.20, the appearance of the cloud deck strongly differs between the original and the projected images. While the original images show all parts of the planet true to the perspective of the VMC, the rectilinear projection tends to distort the polar region quite drastically. Respectively, the polar projection distorts the equatorial region to a point where features get too spread out to be used for tracking.

Since Venus cloud features evolve over time, visual tracking relies on a somewhat subjective approach to identify a cloud feature in two or more images acquired at different times. In the case of VMC data, the orbital motion of the Venus Express spacecraft results in a slightly different observation angle on a given cloud feature due to both its displacement from the ambient flow and the change in perspective. The paired method thus visually measures the combined displacement from change in observation angle and ambient flow. The part due to observation angle change is accounted for by the image navigation implicitly. From the preserved perspective in the original images, the experimenter has good insight into which parts are seen heavily foreshortened, especially close to the limbs. This allows for a well founded possibility to select only the weakly or non-foreshortened features for tracking. On the other hand the apparent feature size and resolution do change along the orbit. Therefore one has to take good care about re-identifying exactly the same part of a feature in different images. This is especially the case in the low contrast areas at higher latitudes. There it is possible for faint feature boundaries to interfere with so called “flat field remainders” which result from occasional residuals of the image artifacts, even after the flat field correction process has been applied to the images.

In the sequential tracking method, possible flat field remainders become distinctively visible after high pass filtering, because they represent high frequency variations. So they can easily be identified and avoided. Since their apparent movement is governed by the change of the VMC perspective on the planet, they mimic a movement completely different from all real atmospheric flows.

Figure 3.22 compares the zonally averaged latitude profiles, in 5° latitude bins, of zonal wind speeds derived from the agglomerate datasets of the sequential (red curve) and paired (blue curve) visual tracking methods and those from digital tracking (black curve). According to convention the westward zonal wind speeds are given as negative values, due to the definition of the eastward oriented coordinate frame for longitudes. The sequential method shows a tendency toward slightly higher speeds on average, which might be an indication for a small bias due to either method. The biggest differences occur at high latitudes, between $70\text{-}80^\circ$ S. It is hard to decide whether this systematic deviation of measurements at high latitudes is entirely due to method or observer bias. Assuming

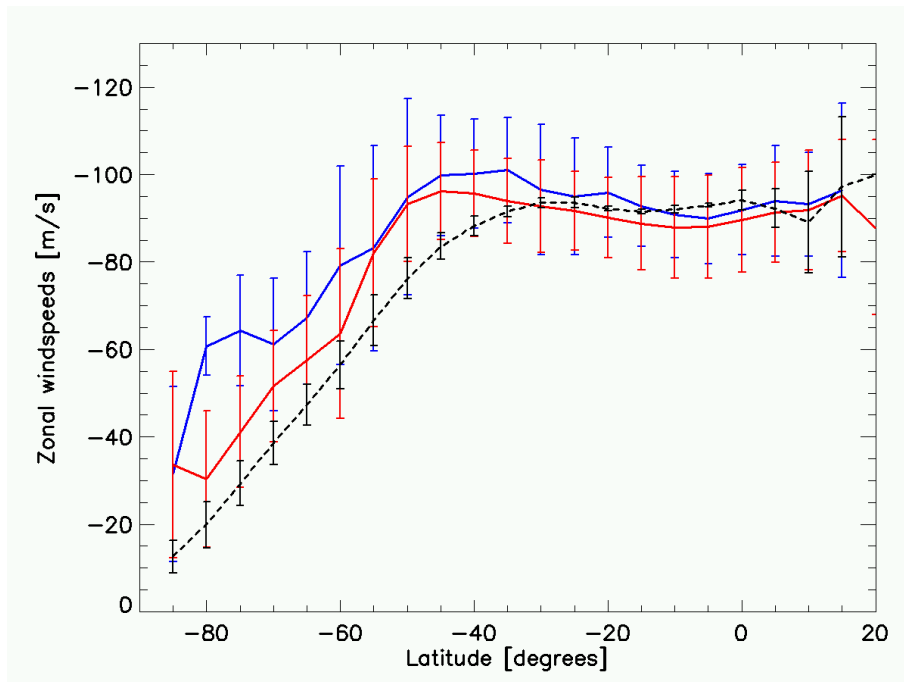


Figure 3.22: Zonally averaged latitudinal profiles of the zonal wind speed component. Derived from the paired (red), sequential (blue) visual tracking methods and the digital (black) method. Error bars represent uncertainties for individual measurements.

a method bias, it is practically impossible to tell which method is biased or if possibly each method would introduce a bias in a different direction. When assuming an observer bias, basically the same issues apply. Keeping in mind the enormous difficulties of finding “good” features to track in the high latitudes, any preference of results from one method or observer over another would introduce a great risk toward a biased end result. Further, the average standard variation in all latitude bins is approximately the same for both visual tracking methods. This is a clear indication that measurement accuracy is nearly the same for both methods.

In conclusion, the deviations between the two visual methods in low latitudes are well on the order of the expected measurement uncertainty for single measurements in the according latitude regions. Therefore low latitude results from both methods are obviously compatible with each other, allowing them to be merged into one common dataset for further evaluations. Despite the obvious discrepancy in the 70-85° S latitude range between the profiles from the two methods, I decided that merging also these results will improve the poor statistics in this region and minimize any present observer bias. At the expense of knowing that biased results may be present in the merged dataset, this approach ensures a more objective dataset in total. In consequence, all following results on the visual wind measurements are based on the merged total dataset, regardless of the employed method.

Also the comparison between the digital and the visual tracking results from the VMC data are in good qualitative agreement up to about 40 degrees latitude. Again a systematic difference between the wind speed profiles is present at higher latitudes. In addition a significant difference of $\sim 15\text{-}20\text{ ms}^{-1}$ between 40 and 60 degrees latitude is apparent between the digital compared to either visual profile. This leaves a big qualitative difference

between the digital profile and the visual ones, because a weak mid-latitude jet can be attributed to the greater zonal wind speed values around $\sim 45^\circ$ to the visual profile, whereas such a feature is entirely absent in the digital profile. There are most likely two causes for this - (i) the morphology and low contrast at these latitudes makes pattern matching by digital cross correlation difficult, and (ii) a selection effect in that visually only the targets that are moving fast are discernible, but in longitude regions where the flow may be slower, no targets are seen as is suggested by the longitudinally biased number distribution of the visual vectors (see fig. 3.21). Further tests have shown that digital results south of 60° S are not very reliable yet and are therefore to be viewed as entirely preliminary at this point.

As a consequence of the unreliable high latitude wind speed values from the digital tracking method and the important systematic differences in the mid latitude regions, I decided to treat digital and visual results strictly separated from each other and focused on the more reliable (and comparable to earlier wind speed profiles) visual tracking results.

3.2.4 Error sources and systematic uncertainties

A number of measurement properties are influencing the accuracy of the wind speed measurements. Main sources of uncertainty are image resolution, measurement accuracy and feature evolution. Additionally some bias from the different methods and/or observers might introduce systematic errors.

(1) Velocity uncertainty of an individual measurement due to limitations in measurement accuracy, such as image resolution, marker position error in the image and varying cloud height is easily assessed via first order Taylor expansion as follows:

$$\delta u = \sqrt{\left(\frac{R_C \cdot \delta \lambda}{\Delta t} \cdot \cos \varphi\right)^2 + \left(\frac{\delta R_C \cdot \Delta \lambda}{\Delta t} \cdot \cos \varphi\right)^2}$$

$$\delta v = \sqrt{\left(\frac{R_C \cdot \delta \varphi}{\Delta t}\right)^2 + \left(\frac{\delta R_C \cdot \Delta \varphi}{\Delta t}\right)^2}$$

Where δ -values denominate total uncertainties for velocities (u,v), measured angular differences (λ, φ) and distance from Venus center to the cloud top (R_C). $\Delta \lambda$ and $\Delta \varphi$ are measured longitude and latitude differences. In the first equation, the latitude is treated as a constant since the effect on u from latitudinal uncertainty is negligible.

For equatorial latitudes the first term, assuming a 1 pixel error and 40 minutes between images further away and 20 minutes when closing in, ranges from about 36 ms^{-1} at apocenter to roughly 10 ms^{-1} at 30,000 km distance from the planet, being $\sim 20 \text{ ms}^{-1}$ on average. This accuracy limit poses a great problem for deriving reliable meridional speeds, since they are supposed to be of the order of $1\text{-}10 \text{ ms}^{-1}$. Of course this source of uncertainty could be further suppressed through choice of image pairs with further increased time intervals. But the early tracking sequences were too short to allow for reasonable statistics with image pairs separated by more than one hour, thus the chosen time intervals represent a trade-off between statistics and precision of the measurements. The second term, assuming 3-5 pixels between images and 10 km uncertainty in cloud deck height, remains well below 1 ms^{-1} in any case and can therefore be neglected.

Possible sources for uncertainty of an individual measurement could arise from:

(2) **Pointing and mapping inaccuracies** are considered to be negligible since both have proven to be extremely accurate and stable. A very conservative estimate would be an inaccuracy amounting to one pixel.

(3) **Pixelation and noise** are assumed to amount to an error of one pixel if physical feature boundaries lie close to the edge of a pixel. Depending on flat field quality, which is varying from orbit to orbit since images of nearly featureless cloud areas are needed, the uncertainty by noise can reach up to two pixels.

(4) **Morphological evolution of features** also influence the measurement accuracy. Since cloud features seldom have clear boundaries, there is always some possible (and variable) inaccuracy in determining the center or exact boundary line of a tracked feature. Furthermore, evolution of cloud features is observed, but due to time intervals between images being always smaller than 4 hours, no significant inaccuracy should arise from them. This has been discussed already for the Pioneer Venus OCPP dataset (Rossow et al. 1990). These issues are especially valid for higher latitudes, since the low contrasts there make identification of the feature boundaries more difficult. It is difficult to quantify the influence of these morphological uncertainties, since they vary significantly with latitude and feature type. As a rule of thumb, the corresponding uncertainty varies between one pixel for small, sharply pronounced features in low latitudes and approximately three pixels for fuzzy low-contrast features in high latitudes.

(5) **Systematic and random errors from measurement methods** are likely to have some effect, as mentioned above. To minimize the effects of erroneous wind speeds from faulty measurements, we decided to reject all vectors outside the interval of -160 ms^{-1} to 0 ms^{-1} for zonal components. These boundaries are based on average wind speeds, ranging approximately between -60 to -100 ms^{-1} , and the assumption of a 2-3 pixel error in the measurements. The constraints for meridional wind components were -60 ms^{-1} to $+60 \text{ ms}^{-1}$, also equivalent to a 2-3 pixel position error of the marker. These selection criteria lead to rejection of about 1.4% of all originally measured vectors.

As in previous works about cloud top winds inferred from the cloud feature tracking, we find that the variability in the derived and the averaged wind speed profiles, including measurements from multiple orbits, are larger than the expected statistical uncertainties from individual measurement errors. Therefore we chose to apply the standard deviation of wind speeds in one latitude bin as a measure of uncertainty for the derived averaged wind speed profiles.

3.2.5 Averaged Zonal wind profiles

The zonal wind component is the observable physical quantity directly connected to the mysterious super-rotation of the Venus atmosphere. Studying its dependence with latitude, local solar time and variability over time is the main tool to acquire information about this ongoing enigma. Figure 3.23, left shows the zonally averaged latitude profiles of zonal wind speed components for the aggregate visual and digital tracking datasets, binned in latitude bins of 5° width. Also shown in the figures is the profile obtained from the VIRTIS 380 nm channel data (Sanchez-Lavega et al. 2008) and the corresponding rotation period derived from the digital and visual profiles. The visually tracked winds in UV from both experiments are in good agreement although VIRTIS tends to show sys-

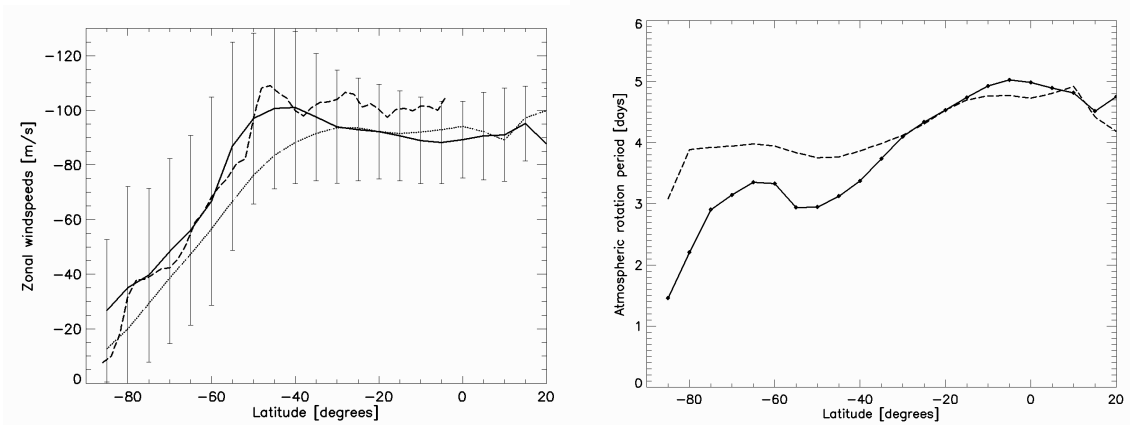


Figure 3.23: Zonally averaged latitudinal wind profiles of the zonal wind component. *Left:* Wind speed profiles from VMC visual tracking (solid line) and digital tracking (dotted line). A latitudinal profile from VIRTIS UV wind measurements is given as comparison (dashed line, profile from Sanchez-Lavega et al. (2008)). Error bars represent standard variation of all measurements in one 5° latitude bin. *Right:* Rotation period as function of latitude from VMC visual (solid line) and digital (dashed line) wind tracking.

tematically stronger winds by $\sim 10 \text{ ms}^{-1}$. A planned re-tracking of the VIRTIS and the VMC results between our wind tracking teams is planned for the future to decide whether this difference is owed to observer or method bias.

At equatorial latitudes zonal wind speed reach $85\text{-}90 \text{ ms}^{-1}$ remaining almost constant with latitude. South of about 20° the latitude profile shows a gradual increase to $\sim 100 \text{ ms}^{-1}$, peaked at about 45° S . This is indicating the presence of a weak mid-latitude jet which is also seen in the inferences from the VIRTIS thermal wind analysis (Picialli et al. 2008) and clearly visible in the compared VIRTIS UV wind profile. Further south, the wind speeds steadily decrease toward the pole. Although the profile is close to a solid body rotation curve at first glance, a closer look at the rotation period in 3.23 (right) reveals significant differences, where solid body rotation profiles would show up as horizontal lines. The pronounced local maximum in rotation period length between $60\text{-}70^\circ$ indicates the transition from the mid latitude to the polar dynamic regime, and is in agreement with the observation of the same effect in the low-accuracy rotation speed measurements from apocentric images. The kink at $\sim 10^\circ \text{ N}$ in the zonal wind profile is very likely an artifact, due to the rather poor sampling as it is at the very edge of VMC coverage of Venus in the tracking image sequences.

The error bars represent standard deviation of the zonal wind speed in each latitude bin. Obviously the deviation increases toward higher latitudes, mostly due to the changes in morphology and difficulties in finding well defined UV markings there, as discussed earlier. The standard deviations significantly exceed the uncertainties of individual measurements (compare to error bars in figure 3.22), indicating a rather strong orbit to orbit variability of the latitudinal profiles of the zonal wind component. Also variability with local time is likely to be present due to influences from planetary scale waves and thermal tides (del Genio and Rossow 1990, Schubert 1983).

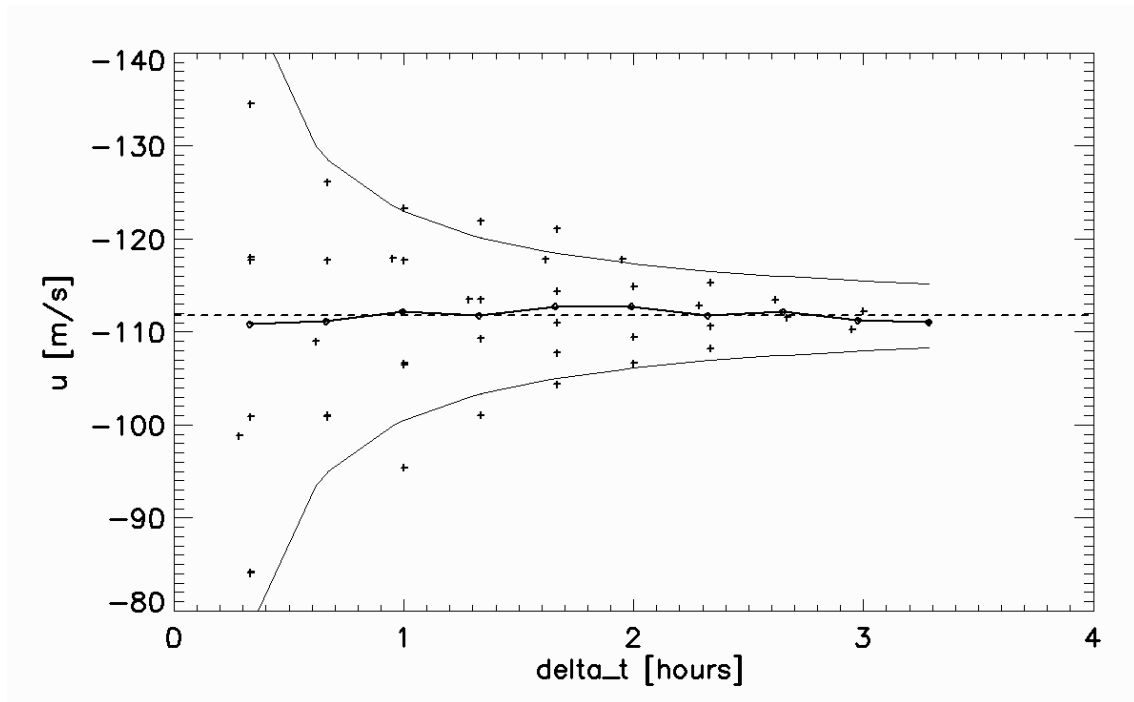


Figure 3.24: Individual zonal wind speed values derived from tracking an individual cloud feature over a period of 3.3 hours in images with a constant time interval of 20 minutes between images. The thick solid line shows average values sorted by time intervals, the dashed line shows the total average value. The thin solid curves denote the spread range resulting from a 2-pixel inaccuracy in the measurements.

3.2.6 Temporal variability of Zonal wind profiles

The first analysis for temporal variability of the zonal winds was to look for potential “in-orbit” variability of the wind speeds on very short timescales. Recent direct wind measurements from observations of Doppler shifts of non-LTE O_2 and CO_2 emission lines have reported strong variability of zonal wind speeds in excess of 20 ms^{-1} on time scales of hours (Widemann et al. 2006).

In order to check for systematic wind speed variations I analyzed the derived wind speeds for individual tracked cloud features and their variability as a function of time between images. Since spatial and temporal resolution change between images, a certain spread in derived wind speeds has to be expected for individual measurements. Figure 3.24 shows all zonal wind speed component values derived for a single cloud feature during a 3.3 hour tracking sequence with time intervals of 20 minutes between each of the 12 images in the sequence. The wind speed values are plotted as a function of time between images and are derived for all possible image pairs in the sequence. An average speed was computed for all wind speed values with the same time interval between measurements (connected by the thick solid line in the figure) and in parallel the average speed for all included measurements was derived (indicated by the dashed line). The two thin solid curves are the spread range resulting from a 2-pixel measurement inaccuracy, as a function of image resolution and time between images. As can be seen from the figure, the measured average speeds for each time interval are in agreement with the total average

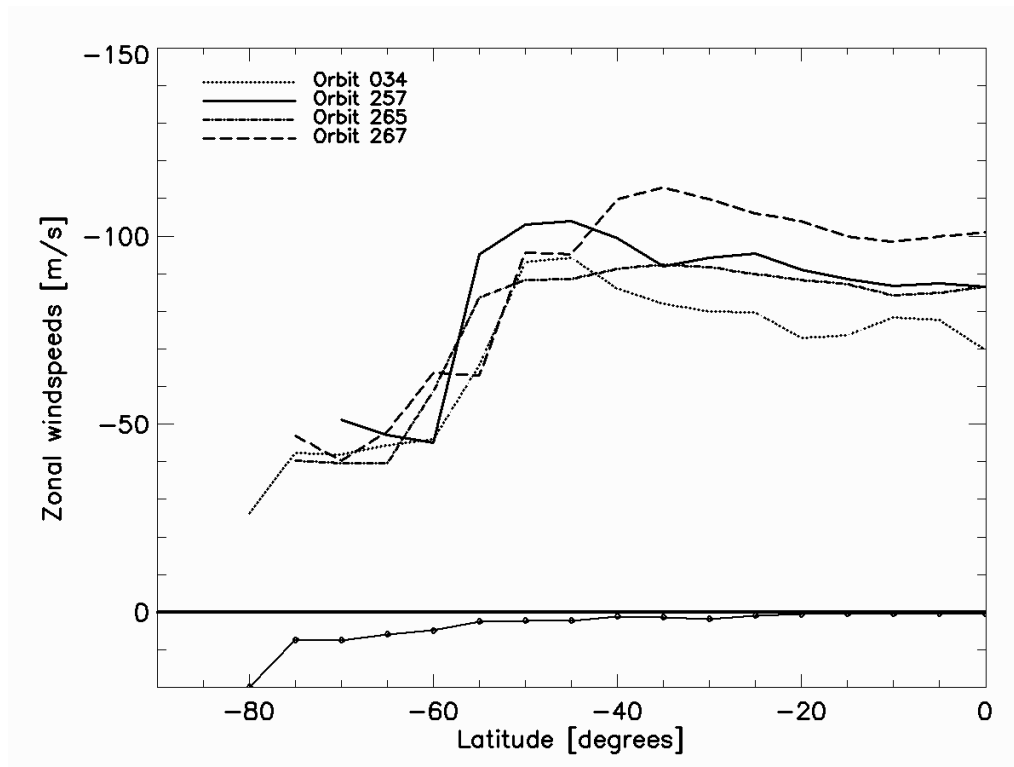


Figure 3.25: Latitudinal zonal wind component profiles for selected individual orbits. The curve at the bottom shows standard deviations divided by the square root of the number of measurements (=standard error of the means) in each 5° latitude bin.

within a spread of $\pm 2 \text{ ms}^{-1}$. Also, the vast majority of measurements is within the spread range introduced by a 2-pixel measurement inaccuracy. This procedure was repeated for the tracking results from all individual features that had been tracked over more than two hours, always showing agreement with the spread expected from a 2-3 pixel inaccuracy in the measurements. Therefore no significant variability in wind speeds on timescales of 2-3 hours was detected in VMC wind measurements.

The next question on the temporal variability of the zonal wind component was: are there really such strong orbit-to-orbit variations and, if yes, how strong are they and on which timescales and with which periodicities do they happen? The first step in order to resolve this question was to look at the variability among zonal wind speed profiles from individual orbits in which wind tracking was performed. Figure 3.25 shows a comparison of four individual orbit profiles with similar local time coverage. The selection includes two orbits with average low latitude speeds (orbits 257, 256), maximum speeds in observations (orbit 267) and minimum speeds in observations (orbit 034). Although the observed variations of zonal wind speeds are within the spread range of individual measurements, a look on the standard error of the mean (absolute values given in the bottom) shows that the mean values are well separated from each other. This implies that the variability of the low latitude zonal winds is about $\pm 15 \text{ ms}^{-1}$ among individual orbits. As only $\sim 10\%$ of all orbits have been used for wind tracking, the total variability might of course be even higher.

Another interesting detail seen in figure 3.25, is the varying position and strength (and

even occurrence) of the position of the wind speed maximum in the mid latitude region. In most of the individual zonal profiles the peak wind speed values are located between 45-50° latitude. But in some cases (like orbit 267) the position of the maximum speeds seems to be shifted to lower latitudes around 35° or no pronounced wind speed maxima have been detected at all. An analysis of the temporal variability of zonal wind speed profiles in high latitudes is extremely difficult, due to the large scatter of individual measurements and the low numbers of vectors retrieved in this regime. The erratic behavior of the wind speed profiles in these latitudes has shown no clear trends or periodicities so far. Occasionally the high latitude parts of the profiles, south of ~55°, show a tendency to behave anti proportional to the low latitude parts with respect to temporal variability of the mean speeds. This means that often speeds in high latitudes seem to be above average when low latitude speeds are below average, and vice versa. But this must remain a rather qualitative statement, since no statistical significance of this relation is apparent. I hope to settle this issue in the future, once we have a larger set of wind-tracked orbits available for further tests in this respect.

The next step was to search for periodicities over different timescales by computing a power spectrum of the variations among all wind-tracked orbits. One significant hindrance to analyzing the power spectrum of the mean zonal velocities over time are the unevenly spaced gaps in temporal coverage, irregular spatial coverage both in latitude and local time and the varying resolution of images in the tracking sequences. Still it should be possible, in principle, to reconstruct the power spectrum, as a large number of reconstruction methods for irregular time series exist (Vio et al. 2000).

Two major transient wave modes on timescales of several days are known to exist on Venus, discussed for example by del Genio and Rossow (1990). The 4-day Kelvin wave mode, especially present in the low latitudes and believed to be responsible for the formation of the Y-feature. And the 5-day Rossby-Haurwitz wave mode, mainly detected in mid latitudes. The influence of the 4-day Kelvin wave mode is most prominently present in latitudes up to ~20° latitude and the 5-day Rossby-Haurwitz mode has mainly been detected between 25-50° (del Genio and Rossow 1990).

Since the latitudinal coverage is varying among the individual wind-tracked orbits I decided to compute power spectra in two separate latitude bands. One between 0-20° latitude and one between 25-50° latitude with a sampling rate of one day. For each strip the average wind speed per orbit was derived. In order to overcome the irregular gaps between the orbits in which wind tracking was performed I used the simplest way to fill the observational gaps by substituting them with the combined average of all wind speeds in the according latitude strip. Figure 3.26 shows the periodograms for the two latitude strips. It displays the square of the wind speed amplitudes derived from digital Fourier transformation (DFT²) as a function of the according periods in days. In the 0-20° latitude strip a prominent peak was detected with a 4-day periodicity, indicating the 4-day Kelvin wave mode in the low latitudes. In the 30-40° strip the 5-day Rossby-Haurwitz wave mode is present. Additionally prominent peaks are present with a 100-day period and around 250 days. These peaks between 100-250 days are possibly artifacts, since they coincide with the time intervals of the largest data gaps.

In order to attempt a direct measurement of the influence of the transient wave modes I tried to search for variations of the mean zonal wind speeds in consecutive orbits. The longest “coherent” measurements in terms of consecutive wind-tracked orbits are present

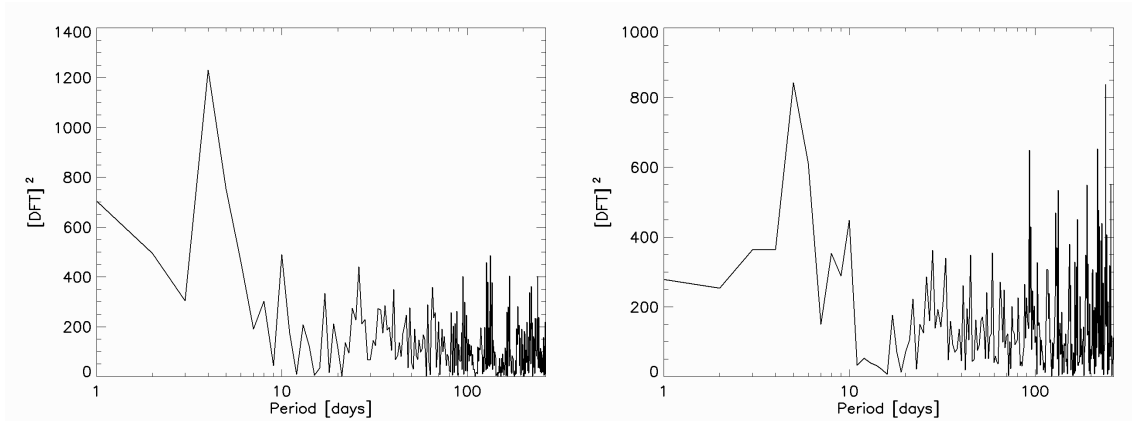


Figure 3.26: Periodograms of the daily average zonal wind speed variations. *Left:* In the latitude strip between $0\text{-}20^\circ$ a prominent peak is detected with a 4-day period. *Right:* In the $20\text{-}40^\circ$ latitude strip, a maximum peak is seen for the 5-day periodicity.

for orbits 281 to 284, and 460 to 463. Although four consecutive orbits are still not covering one complete cycle of both wave modes, I tried to see if the wind speeds at least show some agreement with the assumption of 4- or 5-day periodic variations. The wind-tracked orbit set between 460-463 did not produce any satisfactory correlations with both wave modes but eventually a very good agreement of the average zonal speeds in low latitudes between $0\text{-}25^\circ$ S with a 4-day period could be found. As shown in figure 3.27, a sinusoidal variation with a period of 4 days and an amplitude of 9 ms^{-1} around the mean zonal wind speeds is matching very well the observations. This result also matches those of del Genio and Rossow (1990) who have found a 4-day fluctuation around the zonal mean speed in the same latitude region with amplitudes of $5\text{-}10\text{ ms}^{-1}$. Attempts at identifying a 5-day fluctuation in higher latitudes did not lead to conclusive results. Of course a single measurement over such a short time frame does not permit any real conclusions, but at least the good agreement of this preliminary investigation gives hope that this approach will yield reliable results on the amplitude of the transient wave modes when studying longer sequences of consecutive wind-tracked orbits.

Another timescale on which fluctuations in the zonal wind profiles were detected is on the order of $\sim 100\text{-}200$ days. Figure 3.28 shows the averaged profiles for each of the three separate tracking periods. Period 1 contains all wind speeds tracked between orbits 29 to 72, period 2 contains tracking results from orbits 208 to 295 and period 3 those of orbits 439 to 530. Apparently the average zonal speeds in the low latitudes vary as much as $\pm 5\text{ ms}^{-1}$ among the different periods. In the mid latitude region the profiles of periods 1 and 3 show a pronounced maximum of zonal wind speeds around $\sim 40^\circ$ latitude, indicating the presence of mid latitude jets in this region. In contrast, period 2 (as most of the individual orbits in this period) does not show localized a maximum of wind speeds. A similar phenomenon is present in data from wind tracking of OCPP images on board Pioneer Venus (Limaye 2007), where the profile with data from 1980 does feature a wind speed maximum at $\sim 45^\circ$ S (and another maximum at $\sim 40^\circ$ N) whereas no localized maximum is present in data from 1982. Again, a qualitative correlation between higher average speeds in latitudes between $\sim 0\text{-}30^\circ$ S and simultaneously present lower average speeds

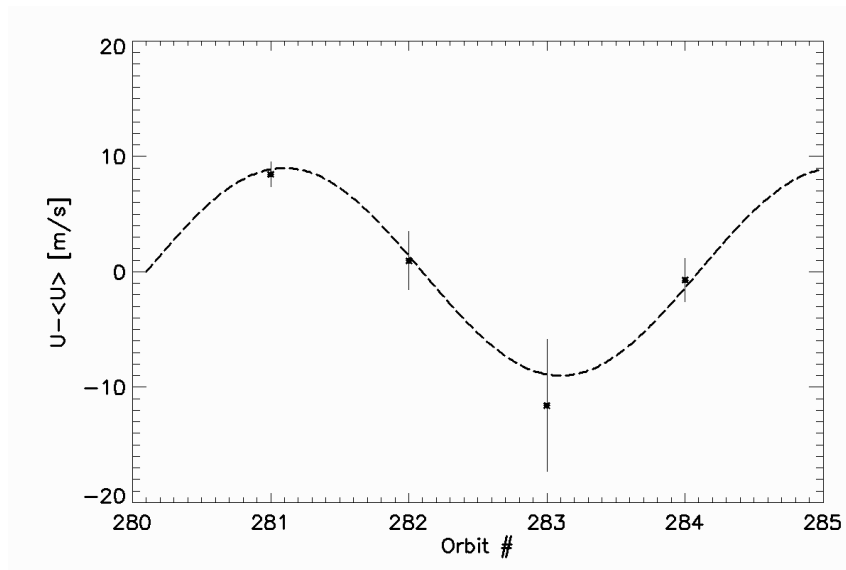


Figure 3.27: Deviations of average zonal wind speeds in four consecutive orbits from the common mean zonal velocities in the low latitude region from 0-35° southern latitude.

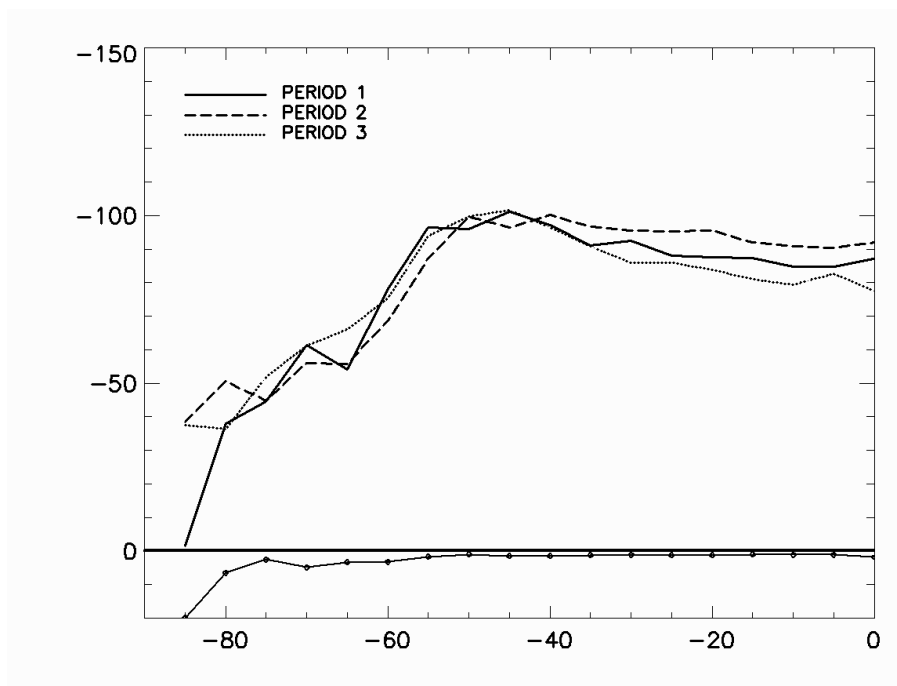


Figure 3.28: Average zonal wind speed profiles for the three separate periods in which wind tracking was performed. The curve on the bottom shows again the standard error of the mean values in each 5° latitude bin (cf. fig. 3.25).

in latitudes between 50-70° S (and vice versa) are observed in the profiles.

The first idea was that these apparent “intermediate”-term (with respect to known long-term variations of the zonal wind speeds on the order of 5-10 years) variations might be an artifact, caused by short term variations. The irregular sampling of orbits in all three periods provides a possibility of biased statistical subsets. Due to the known short term

variations it is thinkable that for example in period 3 more wind-tracked orbits were performed at the minimum zonal wind speed “point” of the 4-day Kelvin mode fluctuations in low latitudes and in period 2 more orbits were tracked at the maximum points of the fluctuations. This hypothesis can be rejected after a quick look at the spread of observed mean values. For period 1 the spread range in low latitudes is -70 to -95 ms^{-1} , for period two they range between -78 to -105 ms^{-1} and for period three this range is -70 to -90 ms^{-1} . Therefore all spread ranges seem to be in agreement with respective mean values being modulated by short term variations with amplitudes of about $\pm 10\text{-}13 \text{ ms}^{-1}$. Also a possible bias due to local solar time distribution was checked. A clear dependency of zonal wind speeds as a function of local solar time was found in each period (this will be addressed in the following subsection) and the distribution of average solar times differed in all three of them. Period 3 was found to be indeed biased toward local solar time regions that showed typically lower average zonal speeds. Because of this, the lower wind speeds in this period can not confidently be attributed to intermediate term variations of the zonal wind fields.

What remains is a not local solar time related difference of $\sim 5 \text{ ms}^{-1}$ in average zonal wind speeds in low latitudes in periods 1 and 2. A possible cause for variations of the zonal wind on these time scales is a “quasi-seasonal” effect introduced by surface topography. Recent VIRTIS temperature soundings have raised the suspicion that the thermal structure of the Venus atmosphere might possibly be influenced by underlying topography (Davide Grassi, private communication). An inhomogeneous thermal field could in principle introduce variations in the wind fields on the time scales in question, since they are comparable to a Venus day. Also here, more future observations are needed to investigate this topic further.

3.2.7 Local solar time dependency of the Zonal wind field

Studying the local solar time (LST) dependency of the zonal wind component, solar-locked phenomena like solar thermal tides can be detected in averaged wind fields. The solar tides have been suggested to play an important role in the maintenance of the super-rotation in Venus’ atmosphere (Newman and Leovy 1992). Figure 3.29 shows the averaged zonal wind field as a function of latitude and LST after binning the wind speed vectors in “boxes” of 0.5 hours local solar time by 5° latitude each. The most obvious feature in low latitudes in the zonal wind field is a pronounced minimum at $\sim 11.5\text{h}$ LST, slightly upstream of the sub-solar point. This is the region where the bow-like waves are most prominently observed. Downstream of the sub-solar region the zonal wind accelerates gradually during the afternoon hours in low latitudes. In the middle latitudes velocities are higher on average over the whole observed LST range, showing lower speeds between 11-13 h LST and maximum wind speeds in the morning and evening hours. In the high latitude region an increase in speed with local time is apparent north of 60° S . Toward the pole zonal speeds are decreasing steadily with increasing latitude. The two dimensional wind map shows clearly that latitudinal profiles with limited LST coverage will show significant correlation with their solar-relative position on the planet. A latitude profile with a LST range centered around noon for example, would show significantly lower speeds than a profile centered on the afternoon LST’s. Going back for a moment to the profiles of the three observation periods in 3.28, the orbits in period 3 did indeed show some bias

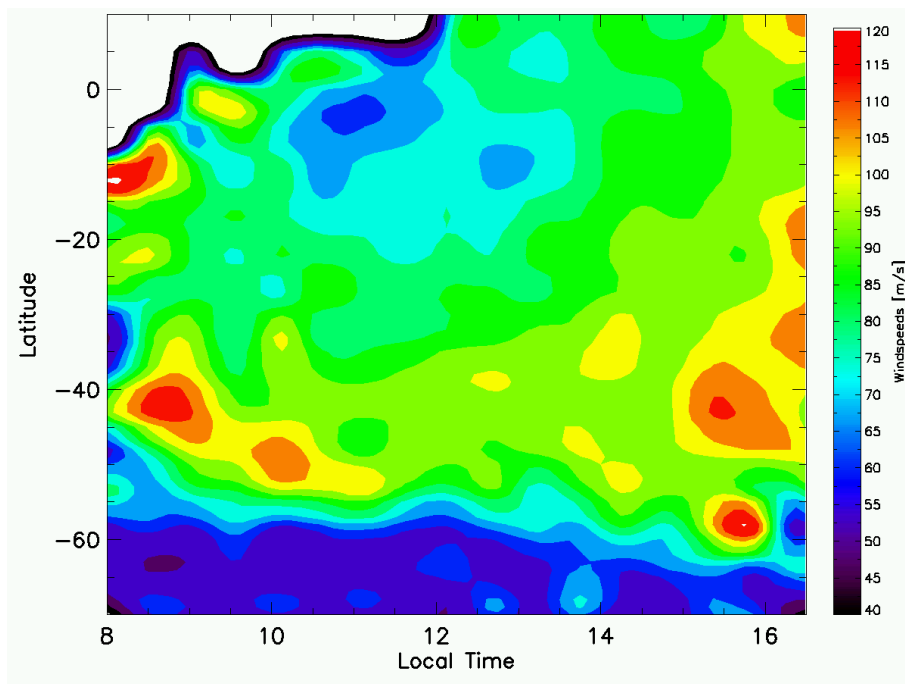


Figure 3.29: Local solar time versus latitude field of the zonal wind component in the southern hemisphere. Wind speeds are color coded in absolute values for westward (toward the right border) flow. Vectors are binned in 5° latitude by 0.5 h LST bins.

toward the noon hours.

The most probable cause for these LST variations in the zonal wind field are of course the solar tides. The main modes observed in the Venus atmosphere are the diurnal and the semidiurnal tide modes. Diurnal and semidiurnal in this respect refer to the global wave mode 1 (diurnal) and mode 2 (semidiurnal). Since VMC observations cover only local solar times between ~ 8 -17 h, the wind field fluctuations due to both the diurnal and semidiurnal component are observed over a phase angle range of 135° . This is unfortunately not enough to cover both the minimum and maximum of the diurnal tide or two maxima/minima of the semidiurnal component. Therefore all inferences on the solar tide influence remain quite limited in accuracy.

Since the influence of thermal tides is likely to be varying with latitude, the data displayed in figure 3.29 have been divided into three 20° wide latitude bands (0 - 20° S, 20 - 40° S, and 40 - 60° S) in order to evaluate tidal components in the zonal wind field in the different latitude regimes. In each of the latitude bands I compared the local time profiles to a simple tidal model that includes both diurnal and semidiurnal components:

$$u(\lambda) = u_0 + u_1 \sin(\lambda + \Phi_1) + u_2 \sin(2\lambda + \Phi_2)$$

Where u_0 is the zonal mean value (averaged over the covered LST range), λ is the longitude, u_1 and u_2 are the diurnal and semidiurnal velocity amplitudes and Φ_1 and Φ_2 are the diurnal and semidiurnal phase angles.

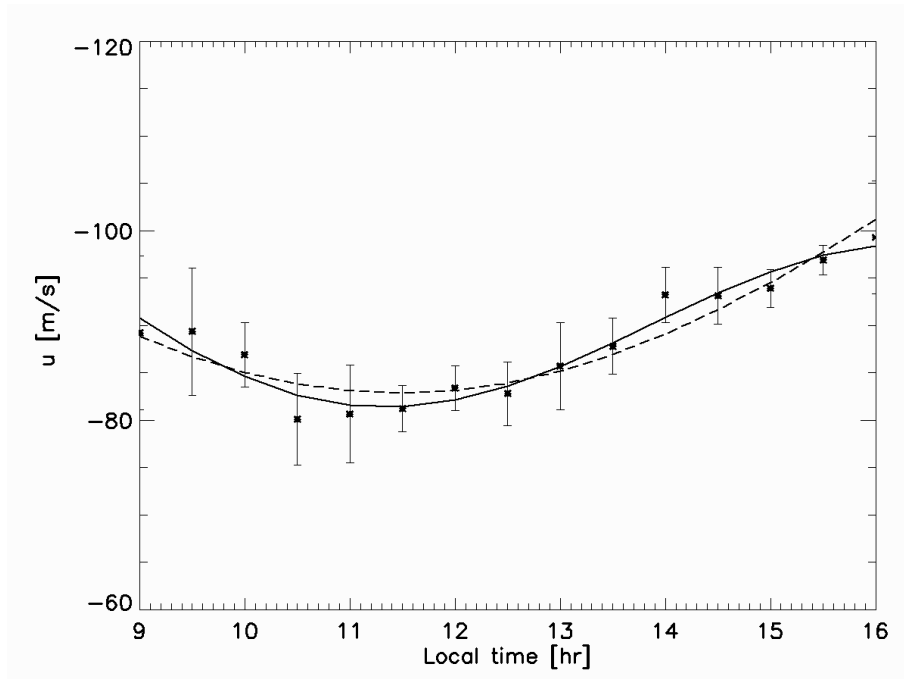


Figure 3.30: Local solar time profile of average zonal wind speeds between 0-20° S latitude in 0.5 h LST bins. The VMC measurements in comparison with best fits for diurnal tide component only (dashed line) and diurnal plus semidiurnal tides (solid line).

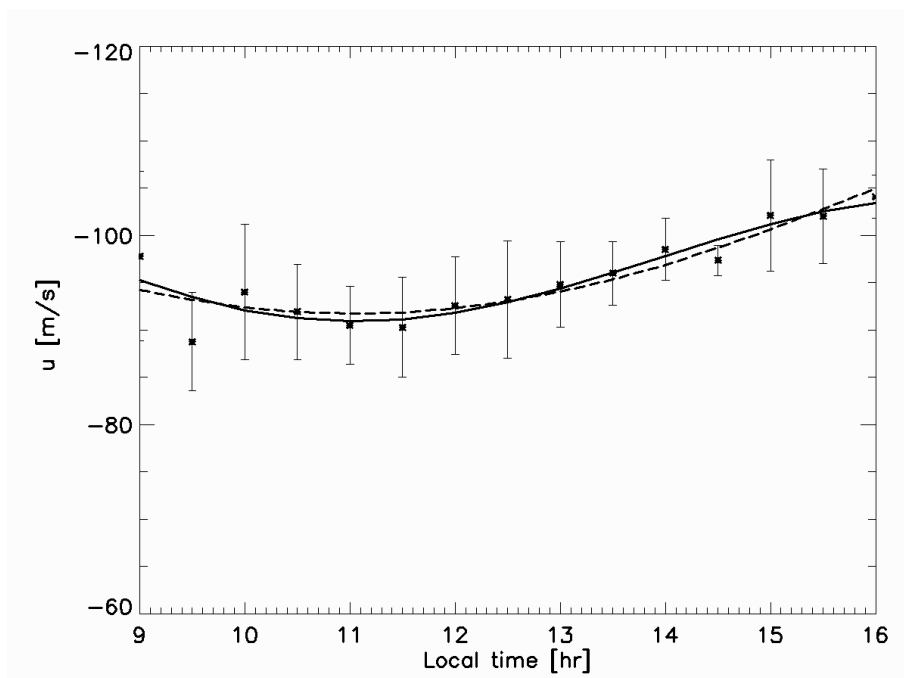


Figure 3.31: Local solar time profile of average zonal wind speeds between 20-40° S latitude in 0.5 h LST bins. The VMC measurements in comparison with best fits for diurnal tide component only (dashed line) and diurnal plus semidiurnal tides (solid line).

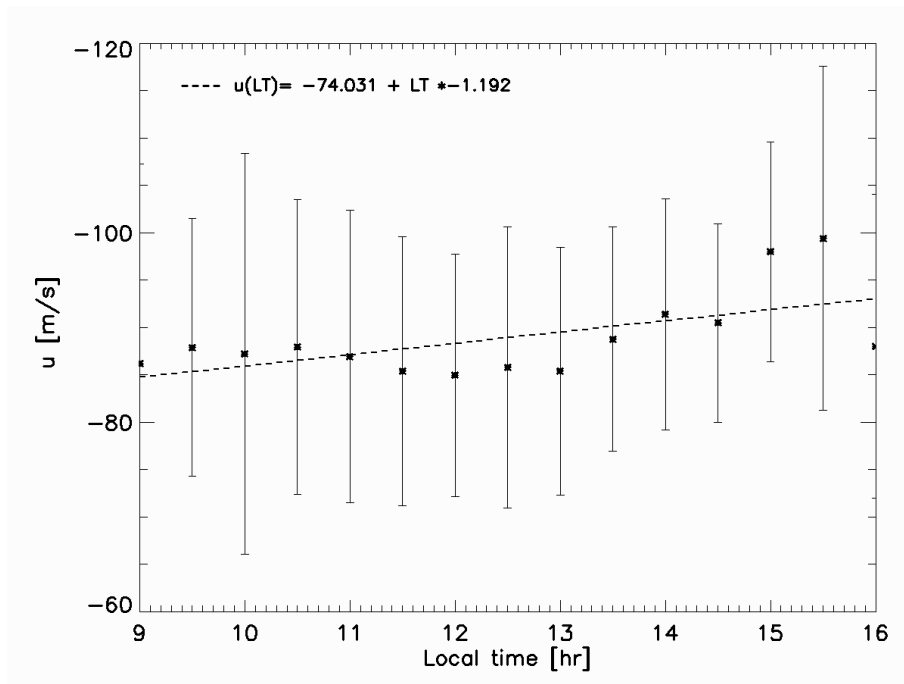


Figure 3.32: Local solar time profile of average zonal wind speeds between 40-60° S latitude in 0.5 h LST bins. No satisfactory tidal fit could be performed. But a general trend of increased wind speeds is present.

The results of this analysis are shown in figures 3.30 (0-20° S latitude), 3.31 (20-40° S latitude) and 3.32 (60-80° S latitude). Fits were performed for diurnal component only and for combined diurnal and semidiurnal components. As is obvious the fits including the semidiurnal component are in better agreement with the observed LST variations in both the 0-20° and the 20-40° latitude strips. No reliable fits have been achieved for the 40-60° latitude strip, but a general increase with LST over the covered range is seen there.

Best fit parameters for the average zonal wind speed and the amplitudes for the diurnal and semidiurnal components were: $u_0 = -95 \text{ ms}^{-1}$, $u_1 = 12 \text{ ms}^{-1}$ and $u_2 = 15 \text{ ms}^{-1}$ in the 0-20° strip and: $u_0 = -98 \text{ ms}^{-1}$, $u_1 = 2 \text{ ms}^{-1}$ and $u_2 = 7 \text{ ms}^{-1}$ in the 20-40° strip. As mentioned, interpretation of these values have to be approached with caution. The true zonal mean value, including the night side values, will most probably differ from the value for u_0 derived from these fits. Also the best-fit amplitudes derived for the tidal amplitudes are not very reliable. It remains the qualitative conclusion that the amplitudes of the semidiurnal tides are observed to be larger than those from the diurnal mode, especially in the mid latitude region.

3.2.8 Meridional wind component

The measuring of the meridional wind components was severely hampered by the relatively low accuracy of $\sim 10\text{-}15 \text{ ms}^{-1}$ of individual measurements in this direction. This leaves the error of a single measurement to be at least twice as large as the expected meridional wind speeds of $\sim 5 \text{ ms}^{-1}$. As can be seen in figure 3.33 the measurement scatter of $\sim 13 \text{ ms}^{-1}$ exceeds the observed variations of the meridional wind component.

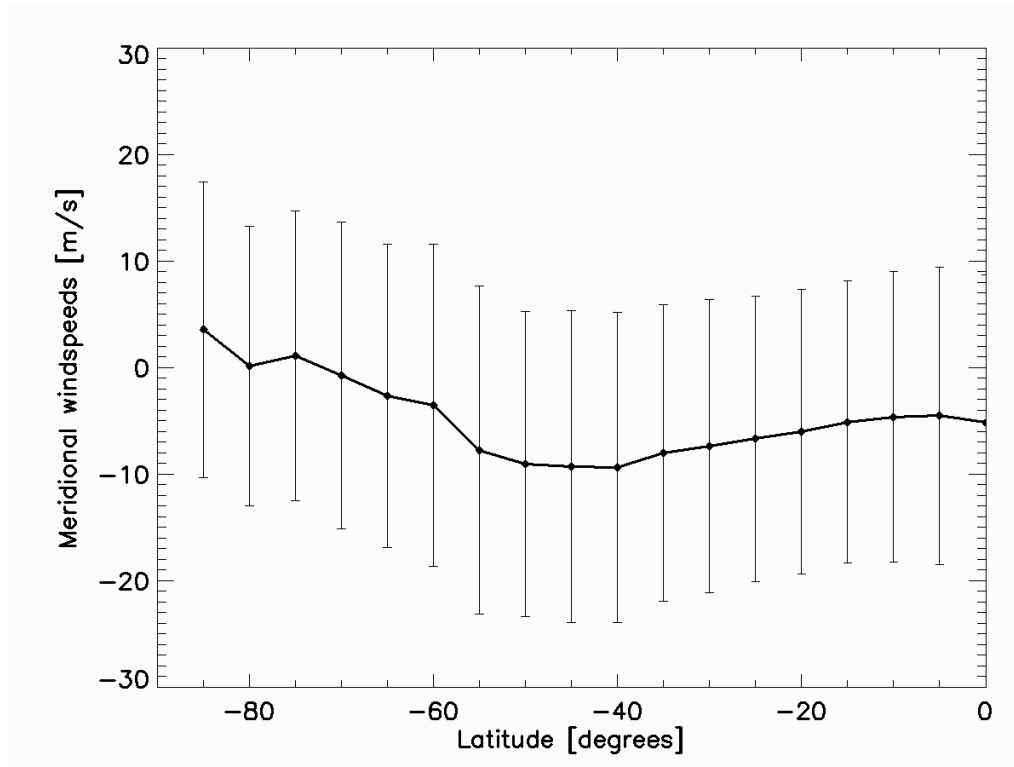


Figure 3.33: Zonally averaged latitudinal wind profiles of the meridional wind component, derived from the VMC visual cloud tracking.

Because of this large uncertainty of the measurements, meridional wind profiles in individual orbits show extreme variabilities on a scale that leaves any inferences from them very doubtful. As a consequence, no detailed investigations on temporal variability of the meridional component will be discussed here. This is especially grave with respect to the investigations on angular momentum transport across the planet, which is mainly driven by the meridional circulation and is certainly playing a key role in the maintenance of the super-rotation.

Nevertheless, the huge number of vectors per 5° latitude bin when deriving a zonally averaged latitudinal profile of the meridional wind speeds (as shown in figure 3.33) lends some level of confidence in the credibility of the profiles. Due to the large numbers of samples the standard error of the mean is suppressed below $\sim 2 \text{ ms}^{-1}$. Therefore at least a general interpretation of the latitudinal profile of the meridional wind component seems likely to give an idea of the meridional circulation profile in the southern hemisphere.

As one can see from figure 3.33 the average meridional wind component ranges from ~ 0 to -10 ms^{-1} , which is qualitatively consistent with previous results. Meridional speeds are slightly increasing from about -5 ms^{-1} near the equator to peak values of around -10 ms^{-1} in the mid latitudes between 40° - 55° S and decreasing again toward the polar region. The observed average profile is in agreement with the assumption of a Hadley type circulation between the equator and the mid latitudes (Schubert 1983, Gierasch et al. 1997). A smoothed wind field in both latitudinal and local solar time directions is given in figure 3.34. From this a general trend of increasing meridional wind speeds toward the afternoon can be deduced.

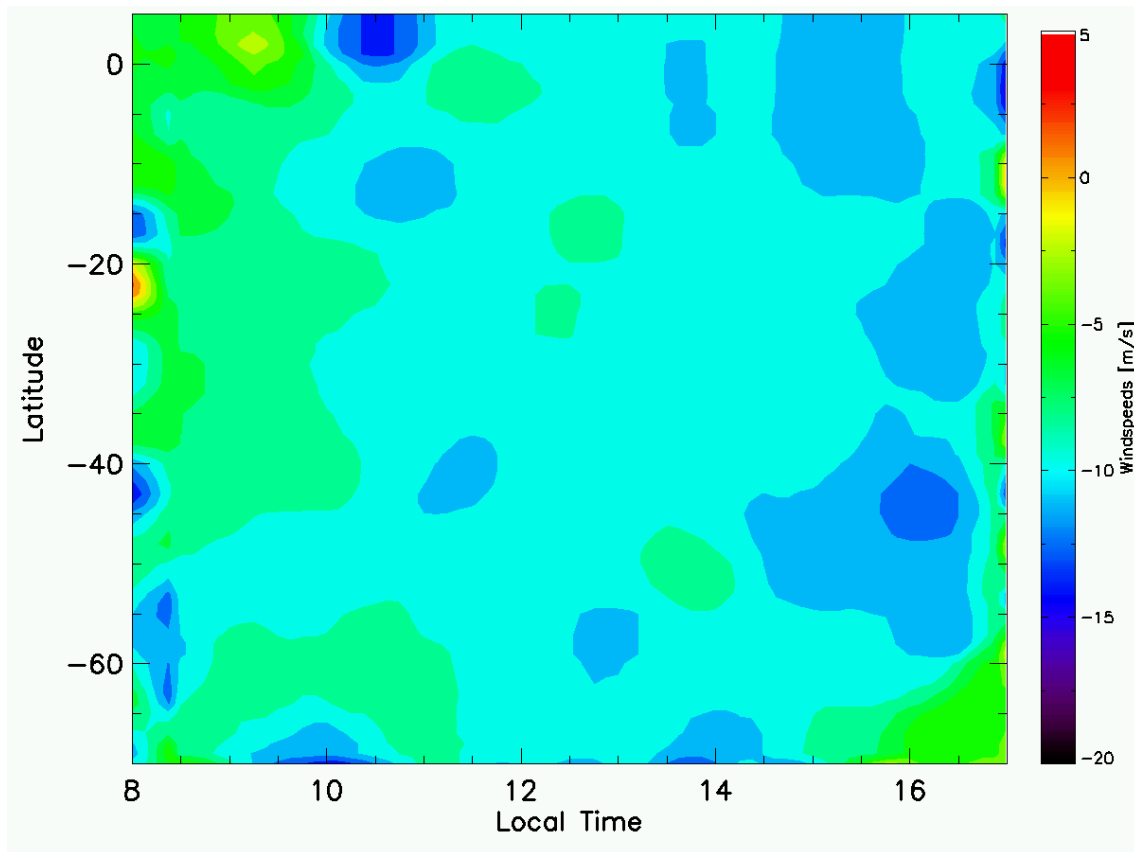


Figure 3.34: Local solar time versus latitude field of the meridional wind component in the southern hemisphere. Wind speeds are color coded in absolute values for westward (toward the right border) flow. Vectors are binned in 5° latitude by 0.5 h LST bins and averaged over 3×3 bins.

Future tracking sequences acquired at shorter distances from Venus will help to improve on accuracy of the meridional wind measurements by increasing image resolution which until now is not sufficient to satisfactorily resolve wind speeds on the order of $0\text{--}10 \text{ ms}^{-1}$. I hope to be able to investigate temporal variability once higher resolution tracking sequences have been evaluated.

4 Discussion and Outlook

4.1 Morphology

As was shown in the course of this thesis, the Venus Monitoring Camera experiment has not only re-identified basically all known morphological features in the cloud top region but also provided new insights into the cloud morphology on all scales. From the apocenter observations it was possible to study the dark and bright polar bands and streaks under a novel perspective for extended periods of time and with varying resolutions. This allows for a complete hemispheric overview at larger distances from Venus and for a close up view while closing in on the planet, virtually “zooming in” on large scale morphological features.

The global morphology has been observed to vary strongly with time. So far no clearly regular or periodic changes in the global-scale morphology could be satisfactorily shown. But as the VMC continues to monitor the south pole of Venus from apocenter and long-term coverage increases, this will likely become possible. Future plans include the systematic study of common properties such as average brightness of the Venus disc and search for possible long-term periodicities in the global distribution of the UV absorber.

Another future investigation will be the combined study of the VMC and VIRTIS observations in the polar region. Figure 4.1 shows a combination of simultaneously acquired images in the UV channel of the VMC and VIRTIS infrared observations. The VIRTIS IR observations are probing the upper cloud deck at an altitude of ~ 50 km, thus looking ~ 20 km deeper into the cloud than the VMC UV images. Several dark and bright spiral bands in the UV on the dayside correspond clearly with the spiral band structures in the IR image on the nightside. Such combined images show impressively that the vortex structure around the south pole of Venus is not only coherent on both the day and the night side but also within the cloud deck and therefore at altitudes between approximately 50-70 km of altitude. As more of such simultaneous observations are acquired, systematic studies combining the results of the polar region collected by the two instruments will be possible in the future.

In addition, the highest resolution images ever taken of the Venus clouds during the pericenter passes of Venus Express allow for more detailed insights on the fine structure of the known morphological features and lead to the discovery of some unusual configurations. Also entirely new features, like the gravity waves in high latitudes, have been discovered in the VMC image sequences.

The discovery of CEB-like structures in latitudes up to 70° indicates that these elongated gravity wave features are not confined to near-equatorial latitudes, but rather are a phenomenon present throughout the planet. Furthermore, the elongated gravity waves

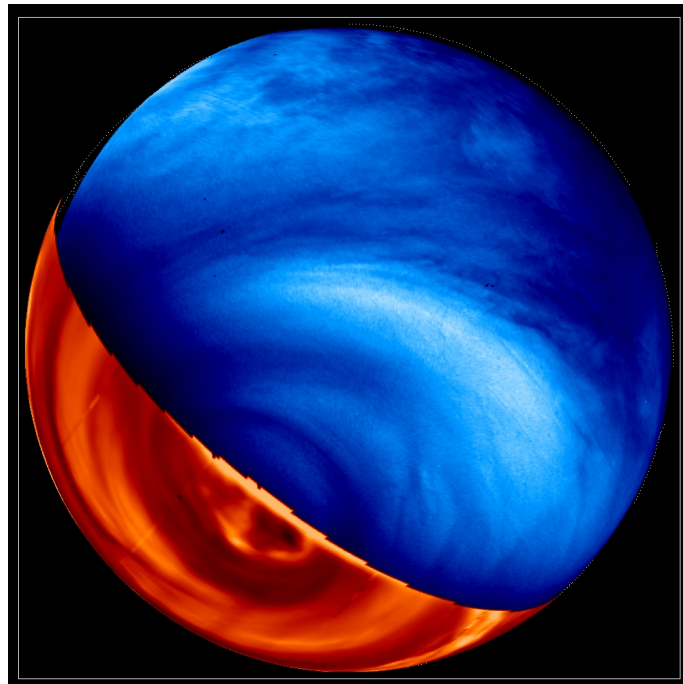


Figure 4.1: Synthetic combination of a VMC UV image (in blue false-color and a simultaneously acquired VIRTIS image (yellow and red false color) in the infrared range. Structures visible in the UV dayside image at an altitude of ~ 70 km show clear correspondence with features on the night side at altitudes around 50 km.

have been observed to occur approximately symmetrically about the equator in both hemispheres in at least one orbit. Figure 4.2 shows two images from orbit 443. The left image was taken in the off-pericenter branch and shows two bright streaks inside a dark mid latitude band at about $45\text{-}50^\circ$ southern latitude. The right image was taken later, during the pericenter pass, and shows elongated wave patterns (categorized as large-type waves earlier on page 54) at $\sim 50^\circ$ northern latitude with a tilt angle similar to those of the bright stripes (mirrored with respect to the equator).

The inferred minimum wavelengths of those elongated gravity waves of ~ 7 km are comparable to the results of an analysis of the CEB's by Belton et al. (1976b), who concluded a wavelength slightly above 5.7 km for them. Further Belton et al. (1976b) have speculated that the gravity waves are possibly triggered by underlying convection and/or oscillations, which is also the likely cause for the wave features discovered in the VMC images at higher latitudes. An interesting analogy to gravity waves of comparable dimensions in Earth's atmosphere is the seemingly exclusive southward progression, which was also observed to be the preferred direction of progression in imagery of terrestrial satellites (Thomas et al. 1975).

The usual co-appearance of the large-type and the small-type (see page 54) gravity waves suggests a link between the two phenomena. The most likely scenario is that the small-type waves are generated as secondary waves after breakdown of the large-type waves, in analogy to results obtained by simulation of secondary wave generation in the terrestrial atmosphere by Lane and Sharman (2006). The medium-type waves (also see page 54) however have only been observed on very few occasions and their interpretation

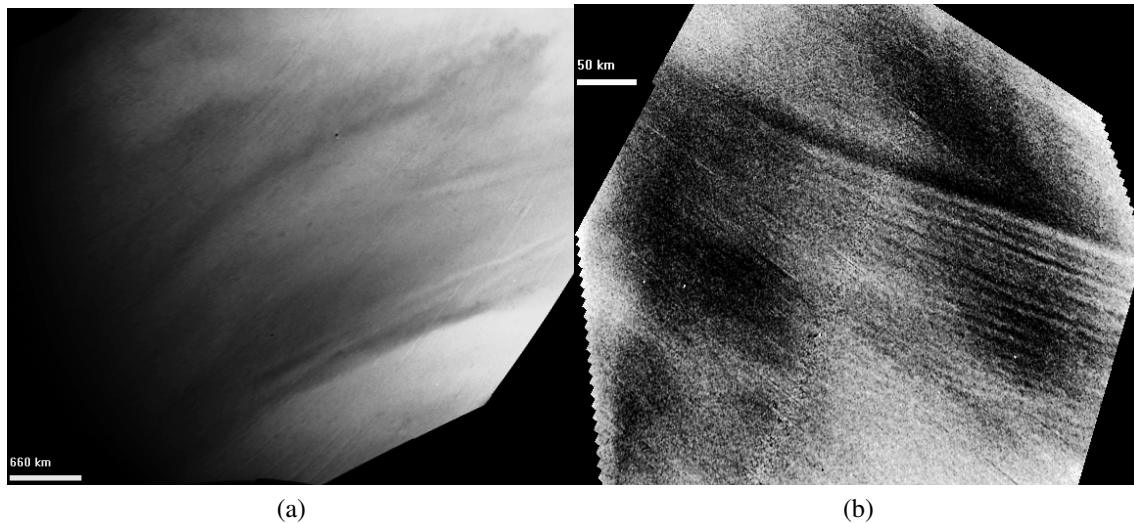


Figure 4.2: *Left:* Image from the off-pericenter part of orbit 443, showing two tilted white stripes inside a dark mid latitude band at $\sim 50^\circ$ S. The tilt angle with respect to the equator is 25° . *Right:* Image from the pericenter pass of the same orbit, showing a group or elongated wave fronts at 50° N with a tilt angle of $\sim 20^\circ$ with respect to the equator.

as oscillations generated by vertical wind-shear has to remain speculative until better statistics are available from future observations.

However, the tentative identification of Kelvin-Helmholtz instabilities at the transitions between dark and bright mid- and high latitude bands (see page 47) and the recurrent sightings of distinctively modified cell-like features near the equator (on page 51) remain hypothetical. A counter-indication for Kelvin-Helmholtz instabilities would be the low horizontal wind shear present in the latitudinal profiles of the zonal wind speed components (compare figure 3.23). Also no physical processes could be identified as a possible cause for the modified cell-like features. Therefore it is possible that both features are erroneously identified. Hopefully, continued investigations on small scale morphology in the VMC images will help to clarify these uncertainties.

The next mission to our neighbor planet will be the Japanese Venus Climate Orbiter (preliminarily named “Planet-C” until launch), scheduled for launch in 2010 (Nakamura et al. 2007). In contrast to the polar orbit of Venus Express, this mission will orbit Venus in an equatorial orbit, thus acquiring images again from a very different perspective. Combined observations from Venus Express and the Venus Climate Orbiter will allow to conduct long term studies of the morphology of the cloud deck simultaneously with two spacecrafts with different perspectives and phase angles for the first time ever.

4.2 Dynamics

The global winds at the cloud top have already been determined from data of previous missions, like Mariner 10, Pioneer Venus and Galileo. In order to investigate a possible long-term variation or evolution of the zonal super-rotation I compared some of those earlier results to the winds derived from tracking of UV cloud features in the VMC images.

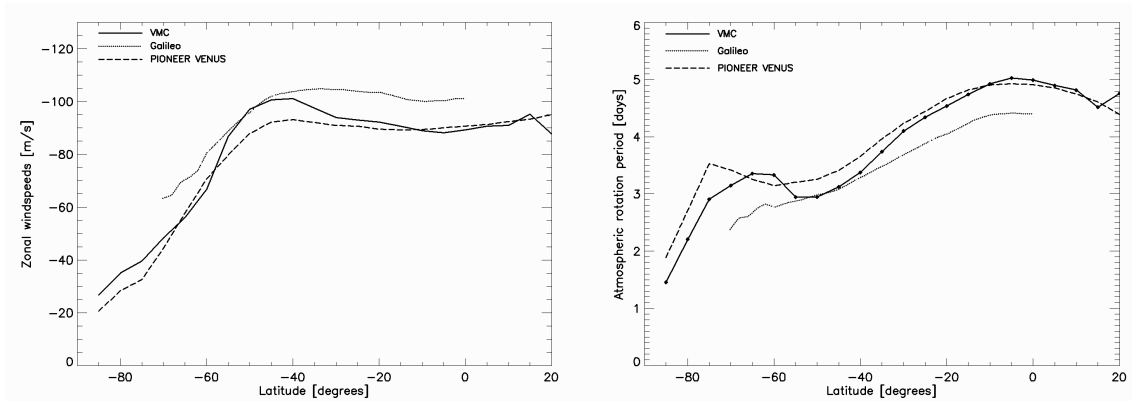


Figure 4.3: *Left*: Zonally averaged latitudinal wind profiles from VMC wind speed measurements (solid line), compared to results from Pioneer Venus (dashed line) and Galileo (dotted line) wind tracking. *Right*: Corresponding rotation periods.

During its flyby at Venus in 1974 Mariner 10 collected image data with resolutions down to 30 km/pixel during the 8 days around its closest approach to the planet. Although resolutions of Mariner 10 images lie within the same range as the VMC data, lack of sufficient overlap with required time interval prevented wind speed measurements from higher resolution images. Therefore I did not include results from Mariner 10 wind tracking in this comparison.

The most extensive dataset so far was obtained by the Pioneer Venus OCPP instrument between 1979 and 1986. The general shape of the Pioneer Venus orbit shared some similarities to the one of Venus Express but with a pericenter at about 15° N the planet was observed mainly from a near-equatorial perspective. In contrast to the Pioneer Venus orbit, the 80° N pericenter of Venus Express allows the VMC to deliver improved coverage of the southern hemisphere in nadir geometry. The average resolution of the OCPP images used for cloud tracking is also around 30 km/pixel. One significant limitation of the OCPP image data is the 4 hour time interval between images (Rossow et al. 1980, 1990). Whereas the instantaneous image acquisition of VMC allows for arbitrary intervals between images.

Figure 4.3 shows a comparison between zonal wind speed profiles from VMC with the previous results from Pioneer Venus and Galileo. The Pioneer Venus profile represents an average of the results from 1980 and 1982 imaging seasons of the OCPP polarimeter (Limaye 2007) which puts the VMC results in good agreement with those from Pioneer Venus. The strong agreement between the long term average profiles from the OCPP and the VMC observations leads to the conclusion that the general state of the super-rotation of the Venus atmosphere has remained stable at least during the last 28 years. Of course this result does not rule out long-term periodicities of the global wind fields on an order of several years but shows that no trends toward acceleration or deceleration of the cloud-level atmospheric dynamics are apparent on a timescale of several decades. Therefore the super-rotation is either in a quasi steady-state or evolving only on very long timescales on the order of 10^2 years or more.

The results from winds tracked in VMC data are also in good general agreement with

the findings from the high resolution cloud tracking in Galileo images . The Galileo probe, which performed a flyby in 1990, acquired data during the 16 hours around closest approach to Venus, and the UV filter was centered at a slightly different wavelength (400 nm). Prior to the VMC observations the Galileo images comprised the best resolved (down to 15 km/pixel) sequences used for cloud tracking, which have recently been reused for high resolution wind tracking (Toigo et al. 1994, Peralta et al. 2007). Time intervals between Galileo images range from 15 min to 2 hr, thus having in principle the same temporal resolution as the VMC sequences. One difference between the average VMC zonal wind profile and the one derived from Galileo data are seen in the low latitudes, where the winds inferred from Galileo images are about 10 ms^{-1} faster than those derived from the VMC cloud tracking. Given the short observation time of only 16 hours, the Galileo data represents the state of the atmosphere over a time period comparable to one single Venus Express orbit. The observed difference from the averaged VMC profile is within the range of day-to-day variability in the VMC data set (compare to figure 3.25). Therefore the wind speeds derived from the VMC and Galileo wind tracking can be considered to be in complete agreement with each other.

One feature that is present to a variable extent or even completely absent in some observations is the existence of a local maximum in zonal wind speed profiles in the middle latitudes (around 45° latitude). As already known from data collected during previous observations, the occurrence of such maxima, their position and the deviation from the mean speeds in low latitudes vary strongly over time in wind speed profiles derived from the VMC data. It is still not known how much of the observed variations are due to the mid-latitude jets in the global wind field. Another possibility would be that the clouds are situated on a different level than the actual mid-latitude jets and therefore provide only very indirect tracers of this phenomenon. A third, but rather unlikely, possible explanation would be that the UV cloud markings in the region of the mid latitude jets simply become, in parts or in total, shielded from view by higher H_2SO_4 haze layers for varying time intervals.

In some cases significant variations in the zonal wind properties were observed especially in the mid latitude regions on an orbit to orbit basis, indicating influences from global scale wave modes. In other cases, more constant conditions were observed over one atmospheric revolution or even longer periods, at cloud top level. These short term variations between results from individual orbit tracking sequences appear to have an impact on the average zonal wind component profiles over longer term observation periods. The 4-day Kelvin wave mode in low latitudes and the 5-day Rossby-Haurwitz wave mode have been detected in the power spectra of the whole available set of wind-tracked orbits (see fig. 3.26). Direct measurements of the amplitudes have been achieved in a single case only, in which the inferred amplitude is in good qualitative agreement with previous measurements (see fig. 3.27). However, longer sequences of coherent tracking data will be required for a detailed study of these global wave modes in the VMC data.

Winds at latitudes higher than 60° south are still difficult to track, due to low contrast and scarcity of features, but increasing data is being collected. Over all, it was possible to extend latitudinal coverage of the cloud top winds with the VMC observations to latitudes around 85° S.

The analysis of the variation of the zonal wind profile with local solar time indicates that diurnal and semidiurnal thermal tides appear to be present in the data from the VMC

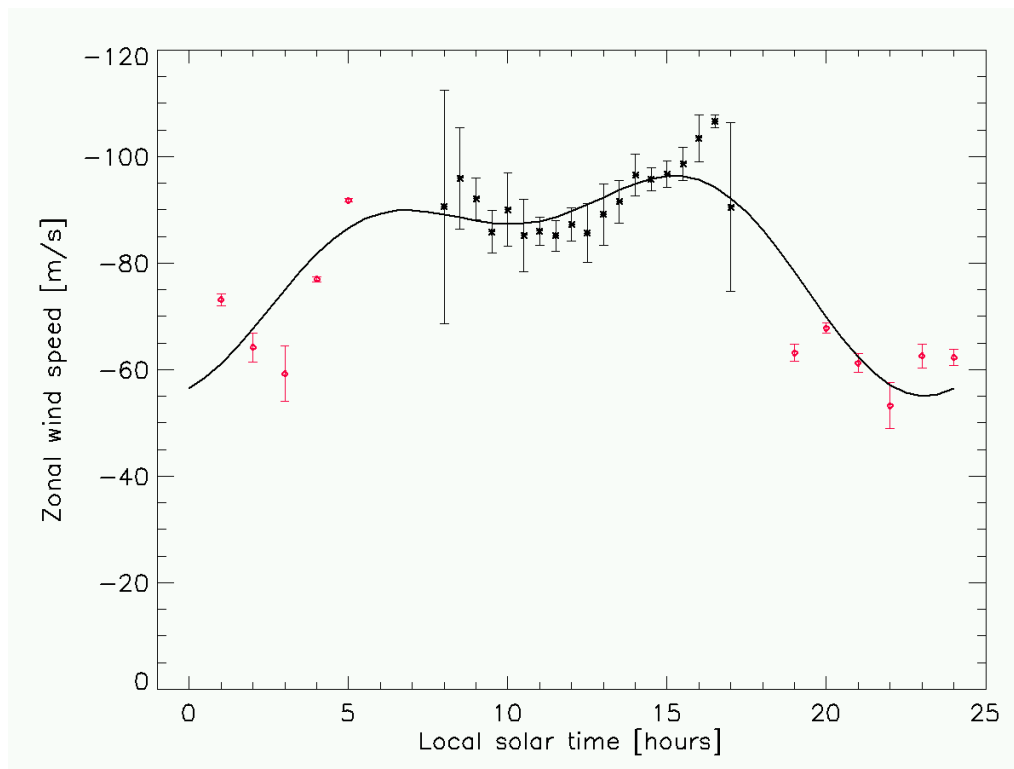


Figure 4.4: Local time profile for latitudes between 20-40° with wind speeds from tracking of UV features in the VMC images in black and night-side winds at the cloud tops derived by Piccialli et al. (2008) from the VIRTIS temperature profiles in red. The curve represents the best fit result from a tidal model with diurnal and semidiurnal components.

wind tracking (compare figures 3.30 and 3.31). The derived best fit values differ considerably from a similar analysis by Limaye (2007) for data from Pioneer Venus observations. The main difference being that the analysis from the VMC data shows a stronger semidiurnal component compared to the diurnal component, whereas the studies by Limaye (2007) concluded a dominant diurnal and a weaker semidiurnal component. But the tidal analysis from the VMC measurements is in qualitative agreement with the results derived from the Pioneer Orbiter Infrared Radiometer (OIR) observations by Schofield and Taylor (1983) and Pechmann and Ingersoll (1984), who determined a dominant semidiurnal component. A more profound confirmation still depends on synthesis of the VIRTIS and VMC observations on night and dayside in order to bridge the large data gap in local time coverage of the VMC UV data between 17h to 9h local solar time.

So far I did one, preliminary, attempt to combine wind tracking from the VMC UV images and winds inferred from the VIRTIS thermal profiles on the night side (Piccialli et al. 2008). The result is shown in figure 4.4. Here I combined the local time profile on the dayside between 20-40° S latitude from the VMC wind tracking with winds inferred for the 40 mbar pressure level between 18-6 h local solar time and between 35-45° of latitude. Then I performed a fit with the same simple tidal model as described on page 78, including the data from both sources. Although the fit result shows a surprising compatibility between the cloud tracked wind speeds and those inferred from the temperature profiles, this comparison should be approached with great caution. The night side winds

are derived under the assumption of cyclostrophic balance, which has been proven to be a good approximation of the wind fields. But since the cyclostrophic balance is by definition based on a global average (see Appendix B), the application to individual zonal sectors does not necessarily provide reliable results for the derived local time profile of the zonal wind speed component. One indication showing the fragility of the fit results for both the VMC local time profile only and the combined day and night side values, are the differences in the derived best fit values. The derived best fit value for the global average for the zonal wind speed in this case is $u_0 = -80 \text{ ms}^{-1}$ (which was -98 ms^{-1} for the best fit from VMC values only). This lower value of the global average wind speed was to be expected, since both peak wind speeds are located on the dayside and one additional minimum of the zonal wind speed is located on the nightside, shortly before midnight. But the best fit values for the diurnal and semidiurnal amplitudes disagree with the finds from the dayside-only analysis. In the combined fit they were found to be $u_1 = 16 \text{ ms}^{-1}$ and $u_2 = 9 \text{ ms}^{-1}$, leaving the diurnal tide the dominant wave mode (in contrast to $u_1 = 2 \text{ ms}^{-1}$ and $u_2 = 7 \text{ ms}^{-1}$ for the dayside-only fit).

Although poorly resolved, results on average meridional wind speed components are in general agreement with previous observations and with the presence of a Hadley cell spanning over the equatorial region and up to about 45° southern latitude. Since measurement accuracy in the analyzed wind tracking sequences is too low to reliably resolve the meridional wind speeds no detailed investigations on this component of the global wind field have been possible so far. Future imaging sequences at higher spatial resolutions will hopefully improve the accuracy up to a degree that allows for more reliable meridional profiles fit for being used to draw more conclusions.

As the VMC continues to acquire data, more and higher resolved UV imaging sequences will become available for dayside cloud-top level tracking. This will improve statistics and achieve a more equal coverage of the day-side local times (compare fig. 3.21). In addition we are investigating whether data from the two IR channels of the instrument could be used for tracking lower level features on the day side and extend cloud tracking to the night side. Although contrasts range in the single percentile range for the IR and VIS features in day side images, it might be feasible to improve contrasts through carefully applied filtering processes to a level which allows for cloud feature tracking. Cloud tracking of IR image sequences would further allow to expand the VMC dynamics investigations to lower altitude levels within the cloud deck. Efforts for both tracking possibilities are in progress at the moment and will be the subject of future investigations. Tracking on the night side would prove even more difficult, since the VMC is registering signals from the surface simultaneously with those from the lower cloud levels.

Meanwhile operations are increasingly adapted and custom fitted for wind tracking in the UV channel, improving steadily on sequence length and also on timing between individual images. Furthermore wind tracking sequences are extended down to lower altitudes of the spacecraft above the planet to allow for higher resolutions and more accurate tracking.

One method for acquiring image sequences for higher resolution cloud tracking is to follow cloud features with the instrument boresight to compensate for the small area covered by pericenter observations. Currently, the VMC imaging sequences are planned and commanded such that the spacecraft is re-pointed between images in a way that the instrument axis follows the approximate track of a cloud feature moving with the average

determined wind speeds on the cloud deck, in order to compensate for the relatively small coverage on the planet in pericenter observations. Although such tracking sequences are limited to time frames of about 30-40 minutes, the very high spatial resolutions during pericenter observations still allow to improve the resolvable velocities in the tracking sequences. It is hoped to achieve tracking sequences with spatial resolutions as high as about 7 km/pixel and velocity resolutions of down to $\sim 5 \text{ ms}^{-1}$. A beneficial side-effect of these high resolution tracking sequences will be that during the relatively short time periods of the tracking cloud features do not evolve as much as during longer observation times, thus diminishing one source of measurement uncertainty.

It should be mentioned that cloud feature tracking is not the only method that has been employed to derive information about the atmospheric dynamics at the Venus cloud top. Another method that has been used to determine global wind fields is the analysis of cloud streak orientations (Smith and Gierasch 1996). This method is based on the assumption that cloud features are produced in the convective lower latitudes and get subsequently advected by zonal and meridional flows, allowing to derive average wind speeds from the cloud streak orientations. Since the cloud feature shape provides a record of the influence of the surrounding winds on it, integrated over the whole time since the start of its formation, this method theoretically provides a tool to derive information on the night side winds even from dayside observations of the cloud deck. The limited time frame for this thesis did, however, only allow for one approach to be followed and I decided to focus on the more widely used cloud tracking approach. Future studies of the cloud top winds will therefore also include evaluation of the wind streak orientations in order to achieve complementary information about the global wind field.

For the future, it is planned that the Japanese Planet-C climate orbiter will observe the Venus atmosphere in concert with the Venus Express, providing valuable data on the atmospheric dynamics and further improving our understanding of the numerous riddles posed to us by the atmosphere of Venus. But ultimately, in order to resolve the key mysteries of the Venusian atmosphere, long term in-situ measurements are needed. One possible scenario would be to deploy several balloons in the Venus atmosphere at varying or variable altitudes, which get transported around the planet by the zonal super-rotation and slowly drift poleward in the meridional flow. With such direct measurements of global wind fields it might finally be possible to unveil the fascinating secrets of our permanently veiled twin sister planet.

A Artifacts in VMC images (extended)

All throughout the mission two distinctive types of artifacts are present in the VMC raw images. Figure A.1 gives an example of the artifact patterns for all four channels in an early orbit. Most prominent and only occurring in the UV channel one can see a dark stripe across the middle of the image, ending in a circular feature. Present in all four channels, but with varying appearance is a pattern of bright polygonal filaments and bright and dark spots.

A.1 Dark UV strip

This feature is produced by discoloration (“yellowing”) of the polymeric micro lens layer due to UV radiation from the sun. During cruise phase The +Z-axis (and therefore the optical axis of VMC) has been pointed in the vicinity of the sun, producing an image of it onto the CCD. During the total duration of approximately 500 hours the position of the Sun on the CCD changed slowly along the path marked by the darkened stripe. Titov and Markiewicz (2006) have reconstructed the pointing during the the cruise phase. They

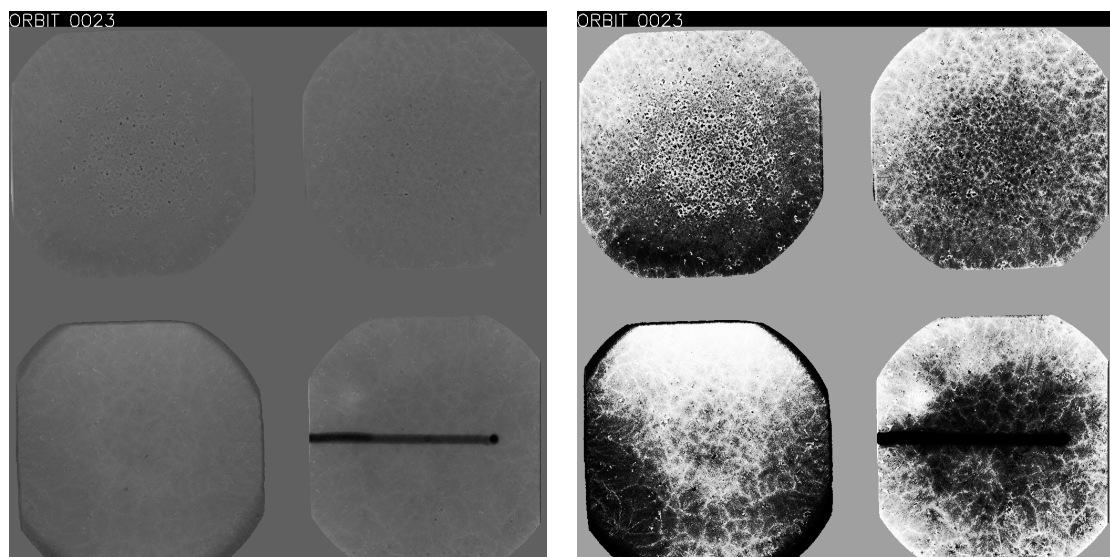


Figure A.1: Full CCD flat field patterns. Order of channels in both versions from top left in clockwise direction : Visible, IR1, UV, IR2. *Left*: Unenhanced flat field showing dark UV stripe. *Right*: Contrast-enhanced version showing filament and spot patterns in all four channels.

successfully correlated the sojourn time of the sun's image on each CCD pixel inside the dark strip to the level of degradation (see fig. A.2). The yellowing of the micro lens layer and resultant attenuation of UV signal is caused by chemical reactions in the polymer, triggered by sun UV radiation.

In the dark stripe signal levels are lowered by about 40% with respect to their surroundings. It has a mean width of ≈ 17 pixels (corresponding to ≈ 13 mrad) and is oriented perpendicular to the CCD columns (in the XY plane of the spacecraft).

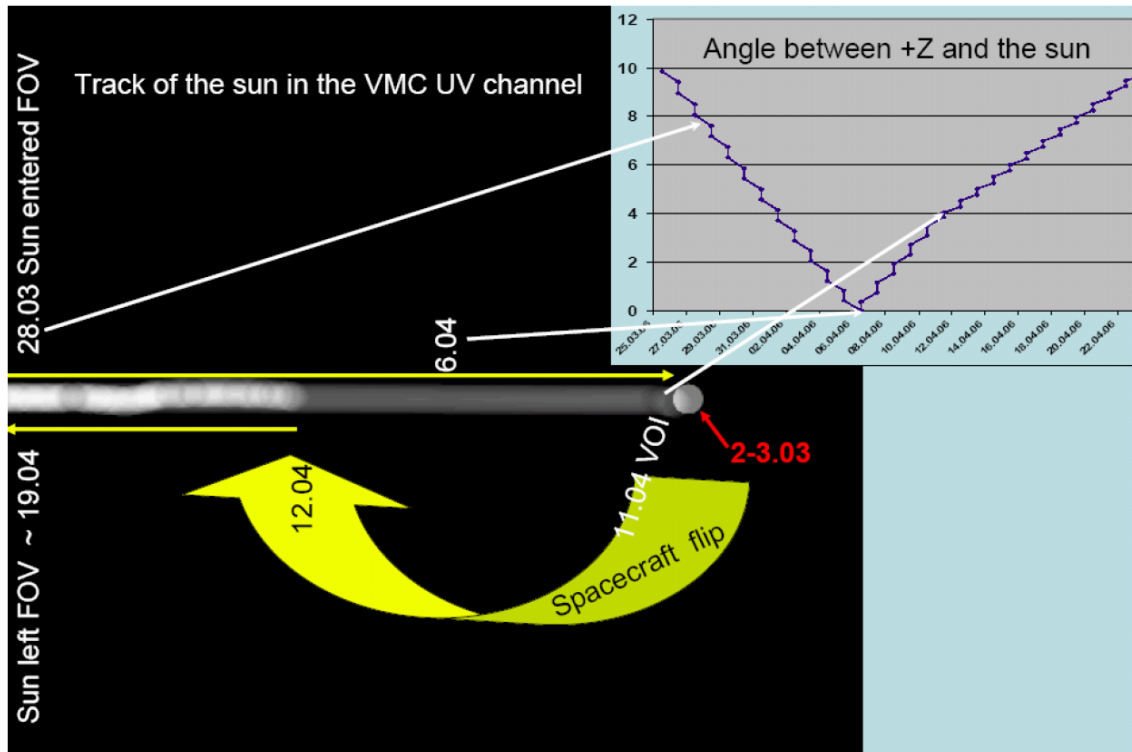


Figure A.2: Track of the Sun image on one quadrant of the CCD reconstructed from SPICE kernels. Brightness of the strip marks total illumination load.

The fact that direct UV radiation from the sun is darkening the micro lens layer led to the suspicion that UV radiation in general might lead to yellowing of the utilized polymer. In particular the relatively high flux of UV radiation reflected by the Venus upper cloud deck could possibly lead to progressive degradation of the UV channel. In order to investigate on a possible progressive degradation of the UV channel, I checked maximum, minimum and mean UV flux into the detector as a function of time throughout the first 670 Orbits. Figure A.3 shows mean flux (in $\text{DN} \cdot \text{s} \cdot 10^{-3}$) per image onto the CCD in the UV channel for dayside pericenter images versus orbit number. The periodic orbit-to-orbit variations are caused by brightness variations across the Venus disc due to the change of the orbital plane with respect to sun incidence angle. The higher fluxes in early orbits are to be attributed to non-linear response of the CCD in overexposed images. Ongoing adjustment of exposure times in later orbits prevented further overexposed images. The large variability of mean brightness per image inside most orbits is governed by the sun aspect angle of the boresight intersection point on the cloud deck.

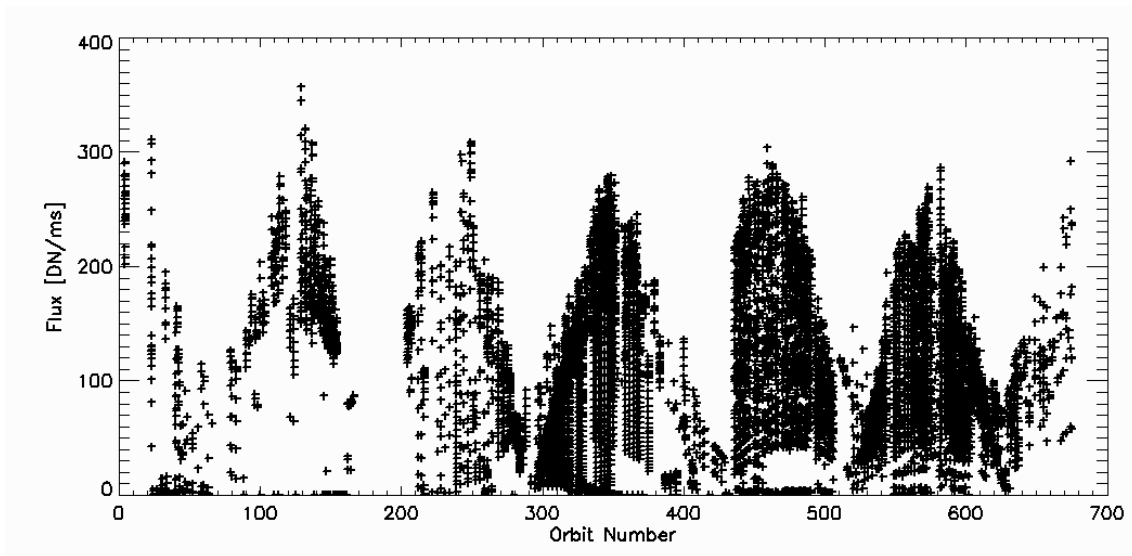


Figure A.3: Mean brightness per (pericenter) image as function of orbit number.

A.2 Filament-spot patterns

Contrary to the dark stripe, which apparently stays constant over time, the filament-spot patterns (further referred to as “FSP”) in all four channels keep evolving over time, displaying mainly erratic but partly cyclical behavior. Examples of the appearance of the FSP at different times during the mission are shown in figure A.4. Detailed study of the FSP showed a number of properties summarized as follows:

1. The FSP include bright filaments, organized in polygonal shapes. Mainly hexagonal shapes are observed.
2. They also include dark spots of varying intensity and size. Smaller sized dark spots are characteristically darker than the larger variants.
3. The dark spots appear to be centered within the hexagonal filaments, giving a cell-like appearance to the FSP.
4. The FSP evolve over time. A widely observed behavior is shrinking size of dark spots and simultaneous darkening thereof.
5. Evolution of the FSP displays cyclic behavior. After dark spots have contracted completely, the cycle of shrinking starts again, usually with irregularly shifted “cells”.
6. Timescales of periodic changes seem to be not completely constant over time, but are on the order of 100-200 orbits
7. Some bright filaments and more spread out dark spots seem to be slightly out of focus, but the small dark spots appear to be nearly always completely in focus

8. Patterns are different in each channel, but general properties are common to all four channels. The IR1 and visible channels sometimes show symmetry about the image center, giving a rosette-like appearance.

This set of properties is strongly reminiscent of convective processes which tend to produce polygonal patterns. Keeping in mind that the observations are conducted in a space environment (vacuum, microgravity), the everyday observable Rayleigh-Bénard convection is very unlikely to be the cause of the FSP, since it is usually driven by density/buoyancy variations in liquids and gases (e.g. boiling water, heating in rooms). The Marangoni convection on the other side seems to be quite a promising candidate to explain the observed symptoms.

Marangoni instabilities arise from surface tension gradients on a gas-gas, liquid-liquid or gas-liquid interface in the presence of thermal gradients. Further no external gravity field nor constraints from aspect ratios between cell diameter and cell depth are required to trigger Marangoni convection.

One possible scenario is therefore that a thin polymeric layer close to the focal plane of the instrument either underwent a thermally induced phase change to a highly viscous film (not necessarily implying complete melting, for which temperatures have not been high enough at any time) or is reaching this state periodically during instrument operations. In both cases the CCD temperature, which varies roughly between 253K and 300K in the course of one orbit due to heat generated from the electronics, would provide a temperature gradient perpendicular to the CCD surface. Since evaporation processes can cause local inhomogeneities in surface tension, outgassing of compounds from a polymer film could provide the necessary random surface tension gradients to produce Marangoni instabilities. Some examples of patterns observed in laboratory experiments by Weh (2005) and Müller-Buschbaum (2003) are shown in figure A.5.

One important piece left in the puzzle is the question whether the polymeric micro lens layer can be identified to be the necessary highly viscous film where the Marangoni convection would be located. One indication against this hypothesis is the dark UV stripe, which is superimposed with the FSP and does not change in appearance at any time. If the micro lens layer would be the location of the Marangoni convection at least some deformation of the borders of the UV stripe should be expected. Since this is not the case, I studied the technical specification Manual for the Kodak KAI-1010M CCD chip used in the VMC. Figure A.6 shows a series of detailed sketches of the chip. In addition to the micro lens layer, an epoxy layer with a thickness of 0.05mm-0.18mm is located 2mm away from the CCD surface. This epoxy layer would be another possible location for the FSP.

In conclusion I propose with some confidence, that the FSP in VMC images are being caused by Marangoni convection either in parts of the micro lens layer or in the epoxy film on the cover glass on top of the CCD. Unfortunately the limited time available precluded further analysis of this interesting topic.

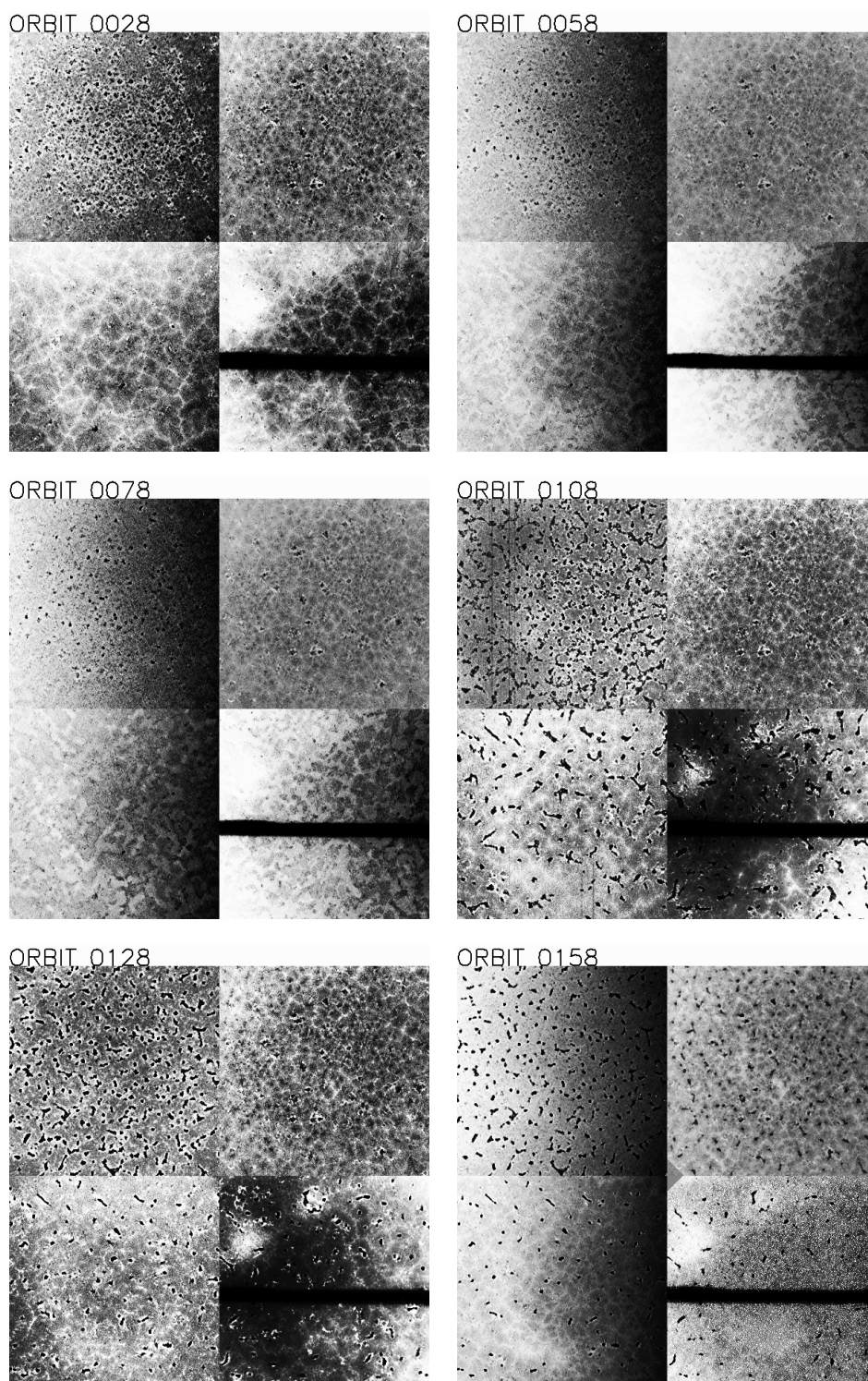


Figure A.4: Excerpts of flat fields from all four channels in different orbits.

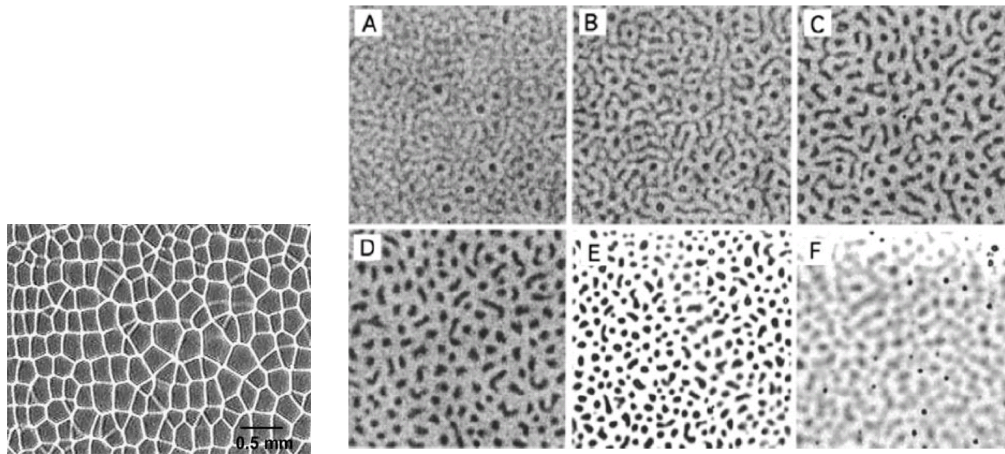


Figure A.5: Examples of patterns resulting from Marangoni convection in thin polymer layers. *Left:* Marangoni convection pattern from Weh (2005). *Right:* Time series of developing Marangoni convection from Müller-Buschbaum (2003).

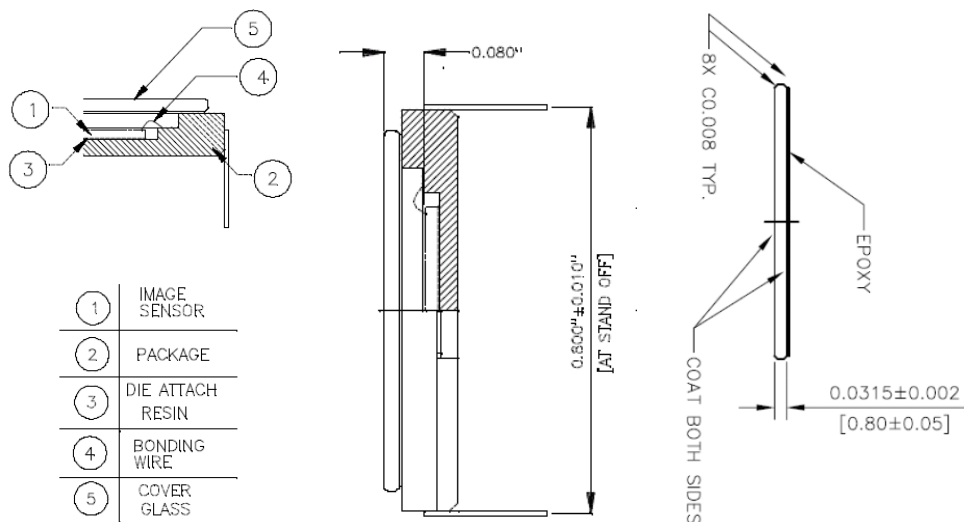


Figure A.6: Detail sketches of Kodak KAI-1010M. *Left:* Description of chip structure. *Middle:* Dimensions. *Right:* Detail sketch of the cover glass, mentioning a thin epoxy layer.

B Cyclostrophic Balance and cyclostrophic winds

Venus's non-equatorial atmosphere between ~ 10 km and the cloud tops can be assumed to be in approximate cyclostrophic balance. This denominates a dynamical state in which the equatorward component of the centrifugal force on a zonally rotating atmospheric parcel is balanced by a poleward meridional pressure gradient force (see B.1).

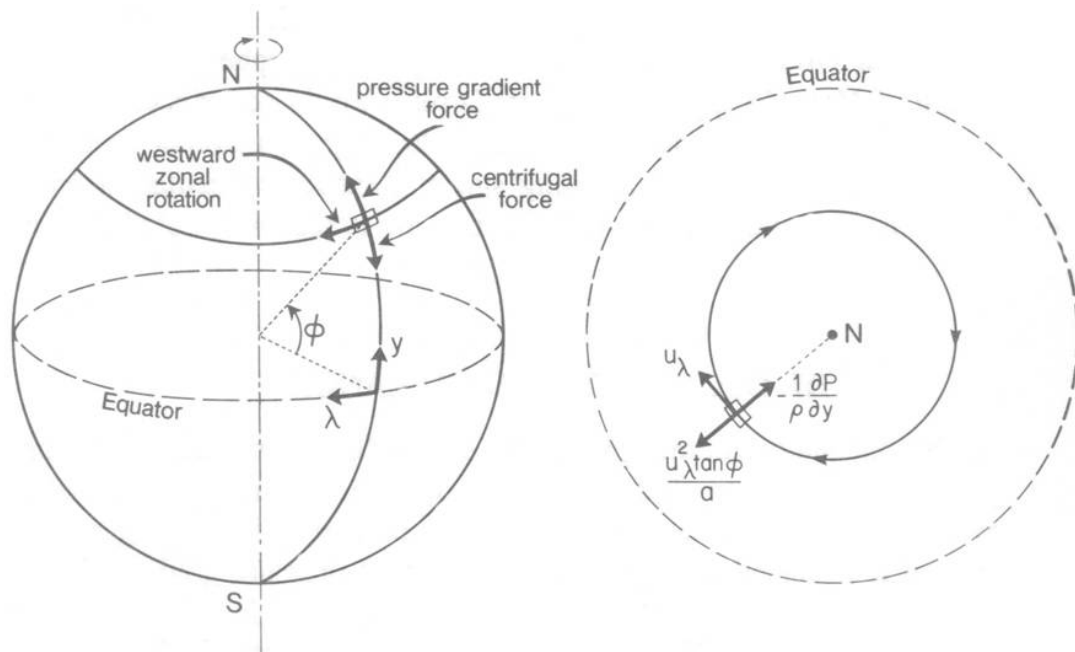


Figure B.1: Sketch of the forces acting on a zonally rotating atmospheric parcel in cyclostrophic balance.

Leovy (1973) first suggested that cyclostrophic balance might occur in the rapidly rotating Venus atmosphere. Measurements of wind speeds and horizontal temperature and pressure contrasts, for example by the Pioneer Venus probes, have since provided qualitative evidence for this balance (Seiff et al. 1980, Schubert et al. 1980). The equatorward latitudinal component of the centrifugal force per unit mass due to zonal motion with westward velocity u_λ is $u_\lambda^2 \tan \phi / a$. The poleward meridional pressure gradient force per unit mass is $-(\partial p / \partial y) / \rho$, where y is a locally northward cartesian coordinate.

[The following derivations are an excerpt from Schubert (1983)] Cyclostrophic balance thus takes the form:

$$\frac{u_\lambda^2 \tan \phi}{a} = -\frac{1}{\rho} \frac{\partial p}{\partial y} \quad (\text{B.1})$$

With the introduction of the geopotential Φ as a product of gravity acceleration g and altitude z and the hydrostatic approximation:

$$\frac{\partial p}{\partial z} = -\rho g \quad (\text{B.2})$$

the cyclostrophic balance equation (B.1) can be written as:

$$\frac{u_\lambda^2 \tan \phi}{a} = -\frac{1}{\rho} \left(\frac{\partial p}{\partial y} \right)_z = -g \left(\frac{\partial z}{\partial y} \right)_p = -\left(\frac{\partial \Phi}{\partial y} \right)_p = -\frac{1}{a} \frac{\partial \Phi}{\partial \phi} \quad (\text{B.3})$$

In terms of the logarithmic pressure coordinate ζ :

$$\zeta = -\ln \frac{p}{p_{ref}} \quad (\text{B.4})$$

where p_{ref} is a reference pressure, the hydrostatic equation become

$$\frac{1}{g} \frac{\partial p}{\partial z} = -\rho = \frac{\partial p}{\partial \Phi} \quad (\text{B.5})$$

$$p \frac{\partial \Phi}{\partial p} = -\frac{p}{\rho} = -RT = -\frac{\partial \Phi}{\partial \zeta} \quad (\text{B.6})$$

$$\frac{\partial \Phi}{\partial \zeta} = RT. \quad (\text{B.7})$$

The perfect gas law $p = \rho RT$ was used in equation B.6. By differentiating equation B.3 with respect to ζ and substituting equation B.7 we obtain:

$$2u_\lambda \frac{\partial u_\lambda}{\partial \zeta} = \frac{R}{\tan \phi} \frac{\partial T}{\partial \phi} \quad (\text{B.8})$$

Equation B.8 is the thermal wind equation for cyclostrophic balance. The vertical derivative of the zonal kinetic energy per unit mass is directly proportional to the latitudinal temperature gradient on a constant pressure surface. If T increases poleward then u_λ increases with height. Note that ζ increases with altitude z according to equation B.4.

Altitude profiles of zonal wind velocity can be inferred from measurements of T as function of latitude by height by integrating equation B.8 over ζ . Derived cyclostrophic wind speeds can be compared with measured zonal wind speeds to test the validity of the cyclostrophic balance approximation. Recent studies on this topic using data from the VIRTIS temperature retrievals are reported by Piccialli et al. (2008).

Bibliography

- Agee, E., 1987, Mesoscale cellular convection over the oceans, *Dynamics of Atmospheres and Oceans*, 10, 317–341
- Allen, D. A., Crawford, J. W., 1984, Cloud structure on the dark side of Venus, *Nature*, 307, 222–224
- Baker, R. D., Schubert, G., Jones, P. W., 1998, Cloud-level penetrative compressible convection in the Venus atmosphere, *Journal of Atmospheric Sciences*, 55, 3–18
- Baker, II, R. D., Schubert, G., 1992, Cellular convection in the atmosphere of Venus, *Nature*, 355, 710–712
- Barabash, S., Sauvaud, J.-A., Gunell, H., Andersson, H., Grigoriev, A., Brinkfeldt, K., Holmström, M., Lundin, R., Yamauchi, M., Asamura, K., Baumjohann, W., Zhang, T. L., Coates, A. J., Linder, D. R., Kataria, D. O., Curtis, C. C., Hsieh, K. C., Sandel, B. R., Fedorov, A., Mazelle, C., Thocaven, J.-J., Grande, M., Koskinen, H. E. J., Kallio, E., Säles, T., Riihela, P., Kozyra, J., Krupp, N., Woch, J., Luhmann, J., McKenna-Lawlor, S., Orsini, S., Cerulli-Irelli, R., Mura, M., Milillo, M., Maggi, M., Roelof, E., Brandt, P., Russell, C. T., Szego, K., Winningham, J. D., Frahm, R. A., Scherrer, J., Sharber, J. R., Wurz, P., Bochsler, P., 2007, The Analyser of Space Plasmas and Energetic Atoms (ASPERA-4) for the Venus Express mission, *Planetary and Space Science*, 55, 1772–1792
- Basilevsky, A., et. al., 2008, VMC images of the surface, submitted, *J. Geophys. Res.*
- Belton, M. J. S., Smith, G. R., Elliott, D. A., Klaasen, K., Danielson, G. E., 1976a, Space-time relationships in the UV markings on Venus, *Journal of Atmospheric Sciences*, 33, 1383–1393
- Belton, M. J. S., Smith, G. R., Schubert, G., del Genio, A. D., 1976b, Cloud patterns, waves and convection in the Venus atmosphere, *Journal of Atmospheric Sciences*, 33, 1394–1417
- Belton, M. J. S., Gierasch, P. J., Smith, M. D., Helfenstein, P., Schinder, P. J., Pollack, J. B., Rages, K. A., Morrison, D., Klaasen, K. P., Pilcher, C. B., 1991, Images from Galileo of the Venus cloud deck, *Science*, 253, 1531–1536
- Bertaux, J. L., Nevejans, D., Korablev, O., Villard, E., Quémerais, E., Fedorova, A., Dubois, J. P., Neefs, E., Muller, C., Leblanc, F., The Spicav Team, 2006, SPI-CAV/SOIR: a suite of three spectrometers to study the global structure and composition

- of the Venus atmosphere, in 36th COSPAR Scientific Assembly, vol. 36 of COSPAR, Plenary Meeting, pp. 2900–+
- Boyer, C., 1961, Recherches sur la rotation de Vénus, *L'Astronomie*, 79, 223
- Boyer, C., Carmichel, H., 1961, Observations photographiques de la planète Vénus, *Annales d'Astrophysique*, 24, 531
- Carlson, R. W., Baines, K. H., Kamp, L. W., Weissman, P. R., Smythe, W. D., Ocampo, A. C., Johnson, T. V., Matson, D. L., Pollack, J. B., Grinspoon, D., 1991, Galileo infrared imaging spectroscopy measurements at Venus, *Science*, 253, 1541–1548
- Counselman, C. C., Gourevitch, S. A., King, R. W., Lorient, G. B., Ginsberg, E. S., 1980, Zonal and meridional circulation of the lower atmosphere of Venus determined by radio interferometry, *J. Geophys. Res.*, 85, 8026–8030
- Covey, C. C., Schubert, G., 1981, Mesoscale convection in the clouds of Venus, *Nature*, 290, 17–20
- Cruikshank, D. P., 1983, The development of studies of Venus, *Venus*
- del Genio, A. D., Rossow, W. B., 1982, Temporal variability of ultraviolet cloud features in the Venus stratosphere, *Icarus*, 51, 391–415
- del Genio, A. D., Rossow, W. B., 1990, Planetary-scale waves and the cyclic nature of cloud top dynamics on Venus, *Journal of Atmospheric Sciences*, 47, 293–318
- Dollfus, A., Camichel, H., Boyer, C., Auriere, M., Bowell, E., Nikander, J., 1975, Photometry of Venus. I - Observation of the brightness distribution over the disk, *Icarus*, 26, 53–72
- Drossart, P., Piccioni, G., Adriani, A., Angrilli, F., Arnold, G., Baines, K. H., Bellucci, G., Benkhoff, J., Bézard, B., Bibring, J.-P., Blanco, A., Blecka, M. I., Carlson, R. W., Coradini, A., di Lellis, A., Encrenaz, T., Erard, S., Fonti, S., Formisano, V., Fouchet, T., Garcia, R., Haus, R., Helbert, J., Ignatiev, N. I., Irwin, P. G. J., Langevin, Y., Lebonnois, S., Lopez-Valverde, M. A., Luz, D., Marinangeli, L., Orofino, V., Rodin, A. V., Roos-Serote, M. C., Saggin, B., Sanchez-Lavega, A., Stam, D. M., Taylor, F. W., Titov, D., Visconti, G., Zambelli, M., Hueso, R., Tsang, C. C. C., Wilson, C. F., Afanasenko, T. Z., 2007, Scientific goals for the observation of Venus by VIRTIS on ESA/Venus express mission, *Planetary and Space Science*, 55, 1653–1672
- Esposito, L. W., 1980, Ultraviolet contrasts and the absorbers near the Venus cloud tops, *J. Geophys. Res.*, 85, 8151–8157
- Esposito, L. W., Knollenberg, R. G., Marov, M. I., Toon, O. B., Turco, R. P., 1983, The clouds are hazes of Venus, pp. 484–564, *Venus*
- Formisano, V., Angrilli, F., Arnold, G., Atreya, S., Baines, K. H., Bellucci, G., Bézard, B., Billebaud, F., Biondi, D., Blecka, M. I., Colangeli, L., Comolli, L., Crisp, D., D'Amore, M., Encrenaz, T., Ekonomov, A., Esposito, F., Fiorenza, C., Fonti, S., Giuranna, M.,

- Grassi, D., Grieger, B., Grigoriev, A., Helbert, J., Hirsch, H., Ignatiev, N., Jurewicz, A., Khatuntsev, I., Lebonnois, S., Lellouch, E., Mattana, A., Maturilli, A., Mencarelli, E., Michalska, M., Lopez Moreno, J., Moshkin, B., Nespoli, F., Nikolsky, Y., Nuccilli, F., Orleanski, P., Palomba, E., Piccioni, G., Rataj, M., Rinaldi, G., Rossi, M., Saggini, B., Stam, D., Titov, D., Visconti, G., Zasova, L., 2006, The planetary fourier spectrometer (PFS) onboard the European Venus Express mission, *Planetary and Space Science*, 54, 1298–1314
- Fritts, D. C., Alexander, M. J., 2003, Gravity wave dynamics and effects in the middle atmosphere, *Reviews of Geophysics*, 41, 1–64
- Galilei, G., 1610, *Le Opere de Galileo Galilei*, Vol.19
- Gierasch, P. J., Goody, R. M., Young, R. E., Crisp, D., Edwards, C., Kahn, R., Rider, D., del Genio, A., Greeley, R., Hou, A., Leovy, C. B., McCleese, D., Newman, M., 1997, The General Circulation of the Venus Atmosphere: an Assessment, in *Venus II: Geology, Geophysics, Atmosphere, and Solar Wind Environment*, (Eds.) S. W. Bougher, D. M. Hunten, R. J. Philips, pp. 459–+
- Häusler, B., Pätzold, M., Tyler, G. L., Simpson, R. A., Bird, M. K., Dehant, V., Barriot, J.-P., Eidel, W., Mattei, R., Remus, S., Selle, J., Tellmann, S., Imamura, T., 2006, Radio science investigations by VeRa onboard the Venus Express spacecraft, *Planetary and Space Science*, 54, 1315–1335
- Huber, P. J., 1977, Early Cuneiform Evidence for the Existence of the Planet Venus, *Scientists Confront Velikovsky*
- Ignatiev, N. I., 2003, Venus Monitoring Camera Sensitivity Study, VMC internal Report.
- Ignatiev, N. I., Moroz, V. i., Zasova, L. V., Khatuntsev, I. v., 1999, Water vapour in the middle atmosphere of Venus: An improved treatment of the Venera 15 ir spectra, *Plan. and Space Science*, 47, 1061–1075
- Ignatiev, N. I., Titov, D. V., Piccioni, G., Drossart, P., Roatsch, T., Manoel, N., 2008, Altimetry of the Venus cloud tops from the Venus Express observations, *J. Geophys. Res.*, submitted
- Kawabata, K., Coffeen, D. L., Hansen, J. E., Lane, W. A., Sato, M., Travis, L. D., 1980, Cloud and haze properties from Pioneer Venus polarimetry, *J. of Geophys. Research*, 85, 8129–8140
- Koukouli, M. E., 2002, Remote sensing of water vapour in Venus' middle atmosphere, Ph.D.thesis, Oxford University
- Krasnopolskii, V. A., 1983, Venus spectroscopy in the 3000-8000 Å region by Veneras 9 and 10, pp. 459–483, *Venus*
- Lane, T. P., Sharman, R. D., 2006, Gravity wave breaking, secondary wave generation, and mixing above deep convection in a three-dimensional cloud model, *Geophys. Res. Letters*, 33, 23 813–+

- Lebonnois, S., Hueso, R., Luz, D., Wilson, C. F., Drossart, P., Piccioni, G., Sanchez-Lavega, A., Titov, D., Baines, K. H., Taylor, F., the VIRTIS/Venus Express Team, 2006, Venus Atmospheric Dynamics From VIRTIS On Venus Express - Preliminary Results, in *Bulletin of the American Astronomical Society*, vol. 38 of *Bulletin of the American Astronomical Society*, pp. 511–+
- Leovy, C. B., 1973, Rotation of the upper atmosphere of Venus., *Journal of Atmospheric Sciences*, 30, 1218–1220
- Limaye, S. S., 1985, Venus atmospheric circulation - Observations and implications of the thermal structure, *Advances in Space Research*, 5, 51–62
- Limaye, S. S., 1988, Venus: Cloud level circulation during 1982 as determined from Pioneer cloud photopolarimeter images. II - Solar longitude dependent circulation, *Icarus*, 73, 212–226
- Limaye, S. S., 2007, Venus atmospheric circulation: Known and unknown, *Journal of Geophysical Research*, 112, 4–+
- Limaye, S. S., Suomi, V. E., 1981, Cloud motions on Venus - Global structure and organization, *Journal of Atmospheric Sciences*, 38, 1220–1235
- Limaye, S. S., Grund, C. J., Burre, S. P., 1982, Zonal mean circulation at the cloud level on venus - spring and fall 1979 occp observations, *Icarus*, 51, 416–439
- Limaye, S. S., Grassotti, C., Kuetemeyer, M. J., 1988, Venus: Cloud level circulation during 1982 as determined from Pioneer cloud photopolarimeter images. I - Time and zonally averaged circulation, *Icarus*, 73, 193–211
- Markiewicz, W. J., Titov, D. V., Ignatiev, N., Keller, H. U., Crisp, D., Limaye, S. S., Jaumann, R., Moissl, R., Thomas, N., Esposito, L., Watanabe, S., Fiethe, B., Behnke, T., Szemerey, I., Michalik, H., Perplies, H., Wedemeier, M., Sebastian, I., Boogaerts, W., Hviid, S. F., Dierker, C., Osterloh, B., Böker, W., Koch, M., Michaelis, H., Belyaev, D., Dannenberg, A., Tschimmel, M., Russo, P., Roatsch, T., Matz, K. D., 2007a, Venus Monitoring Camera for Venus Express, *Planetary and Space Science*, 55, 1701–1711
- Markiewicz, W. J., Titov, D. V., Limaye, S. S., Keller, H. U., Ignatiev, N., Jaumann, R., Thomas, N., Michalik, H., Moissl, R., Russo, P., 2007b, Morphology and dynamics of the upper cloud layer of Venus, *Nature*, 450, 633–636
- McGouldrick, K., Toon, O. B., 2007, An investigation of possible causes of the holes in the condensational Venus cloud using a microphysical cloud model with a radiative-dynamical feedback, *Icarus*, 191, 1–24
- McGouldrick, K., Toon, O. B., 2008, Observable effects of convection and gravity waves on the Venus condensational cloud, *Planetary and Space Science*, submitted
- Müller-Buschbaum, P., 2003, Dewetting and pattern formation in thin polymer films as investigated in real and reciprocal space, *J. Phys.: Condens. Matter*, 15, R1549–R1582

- Moroz, V. I., 2002, Estimates of visibility of the surface of Venus from descent probes and balloons, *Plan. Space Sci.*, 50, 287–297
- Murray, B. C., Belton, J. S., Danielson, G. E., Davies, M. E., Gault, D., Hapke, B., O’Leary, B., Strom, R. G., Suomi, V., Trask, N., 1974, Venus: Atmospheric motion and structure from Mariner 10 pictures, *Science*, 183, 1307–1315
- Nakamura, M., Imamura, T., Ueno, M., Iwagami, N., Satoh, T., Watanabe, S., Taguchi, M., Takahashi, Y., Suzuki, M., Abe, T., Hashimoto, G. L., Sakanoi, T., Okano, S., Kasaba, Y., Yoshida, J., Yamada, M., Ishii, N., Yamada, T., Uemizu, K., Fukuhara, T., Oyama, K.-I., 2007, Planet-C: Venus Climate Orbiter mission of Japan, *Planetary and Space Science*, 55, 1831–1842
- Newman, M., Leovy, C., 1992, Maintenance of strong rotational winds in Venus’ middle atmosphere by thermal tides, *Science*, 257, 647–650
- Pechmann, J. B., Ingersoll, A. P., 1984, Thermal tides in the atmosphere of Venus - Comparison of model results with observations, *Journal of Atmospheric Sciences*, 41, 3290–3313
- Peralta, J., Hueso, R., Sánchez-Lavega, A., 2007, A reanalysis of Venus winds at two cloud levels from Galileo SSI images, *Icarus*, 190, 469–477
- Piccialli, A., Titov, D. V., Grassi, D., Khatuntsev, I., Drossart, P., Piccioni, G., 2008, Cyclostrophic winds from the VIRTIS temperature sounding: a preliminary analysis, *J. Geophys. Res.*, submitted
- Pollack, J. B., Toon, O. B., Whitten, R. C., Boese, R., Ragent, B., Tomasko, M., Eposito, L., Travis, L., Wiedman, D., 1980, Distribution and source of the UV absorption in Venus’ atmosphere, *J. Geophys. Res.*, 85, 8141–8150
- Ross, F. E., 1928, Photographs of Venus, *Astrophysics. J.*, 68, 57–92
- Rossow, W. B., del Genio, A. D., Limaye, S. S., Travis, L. D., 1980, Cloud morphology and motions from Pioneer Venus images, *Journal of Geophysical Research*, 85, 8107–8128
- Rossow, W. B., del Genio, A. D., Eichler, T., 1990, Cloud-tracked winds from Pioneer Venus OCPP images, *Journal of Atmospheric Sciences*, 47, 2053–2084
- Sanchez-Lavega, A. R., Hueso, G., Piccioni, G., Peralta, J., Perez-Hoyos, S., Wilson, C. F., Taylor, F. W., Baines, K. H., Luz, D., Erard, S., Lebonnois, S., 2008, Variable winds on Venus mapped in three dimensions, *Icarus*, submitted
- Schofield, J. T., Taylor, F. W., 1983, Measurements of the mean, solar-fixed temperature and cloud structure of the middle atmosphere of Venus, *Quarterly Journal of the Royal Meteorological Society*, 109, 57–80
- Schofield, J. T., Taylor, F. W., McCleese, D. J., 1982, The global distribution of water vapor in the middle atmosphere of Venus, *Icarus*, 52, 263–278

- Schubert, G., 1983, General circulation and the dynamical state of the Venus atmosphere, pp. 681–765, *Venus*
- Schubert, G., Covey, C., del Genio, A., Elson, L. S., Keating, G., Seiff, A., Young, R. E., Apt, J., Counselman, C. C., Kliore, A. J., Limaye, S. S., Revercomb, H. E., Sromovsky, L. A., Suomi, V. E., Taylor, F., Woo, R., von Zahn, U., 1980, Structure and circulation of the Venus atmosphere, *Journal of Geophysical Research*, 85, 8007–8025
- Seiff, A., Kirk, D. B., Young, R. E., Blanchard, R. C., Findlay, J. T., Kelly, G. M., Sommer, S. C., 1980, Measurements of thermal structure and thermal contrasts in the atmosphere of Venus and related dynamical observations - Results from the four Pioneer Venus probes, *Journal of Geophys. Res.*, 85, 7903–7933
- Smith, B. A., 1967, Rotation of Venus: Continuing Contradictions, *Science*, 158, 114–116
- Smith, M. D., Gierasch, P. J., 1996, Global-Scale Winds at the Venus Cloud-Top Inferred from Cloud Streak Orientations, *Icarus*, 123, 313–323
- Smith, M. D., Gierasch, P. J., Schinder, P. J., 1992, A global traveling wave on Venus, *Science*, 256, 652–655
- Suomi, V., 1975, Cloud Motions on Venus, in *The Atmosphere of Venus*, (Ed.) J. E. Hansen, pp. 42–+
- Suomi, V. E., Limaye, S. S., 1978, Venus - Further evidence of vortex circulation, *Science*, 201, 1009–1011
- Svedhem, H., Titov, D. V., McCoy, D., Lembreton, J.-P., Barabash, S., Bertaux, J.-L., Drossart, P., Formisano, V., Häusler, B., Korablev, O., Markiewicz, W. J., Nevejans, D., Pätzold, M., Piccioni, G., Zhang, T. L., Taylor, F. W., Lellouch, E., Koschny, D., Witasse, O., Eggel, H., Warhaut, M., Accomazzo, A., Rodriguez-Canabal, J., Fabrega, J., Schirmann, T., Clochet, A., Coradini, M., 2007, Venus Express – The first European mission to Venus, *Planetary and Space Science*, 55, 1636–1652
- Taylor, F. W., 2006a, Climate Variability on Venus and Titan, *Space Science Reviews*, 125, 445–455
- Taylor, F. W., 2006b, Venus before Venus Express, *Planetary and Space Science*, 54, 1249–1262
- Taylor, F. W., Beer, R., Chahine, M. T., Diner, D. J., Elson, L. S., Haskins, R. D., McCleese, D. J., Martonchik, J. V., Reichley, P. E., Bradley, S. P., Delderfield, J., Schofield, J. T., Farmer, C. B., Froidevaux, L., Leung, J., Coffey, M. T., Gille, J. C., 1980, Structure and meteorology of the middle atmosphere of Venus Infrared remote sensing from the Pioneer orbiter, *J. Geophys. Res.*, 85, 7963–8006
- Taylor, F. W., Kamp, L. W., Calcutt, S. B., 1990, High latitude phenomena, deep cloud structure, and water vapour on Venus, *Advances in Space Research*, 10, 47–56

- Thomas, J. E., Kays, M. D., Horn, J. D., Moore, R. L., 1975, Visual Observation of Propagating Gravity Waves on ATS III Satellite Film Loops, Technical Report ECOM-5553. U.S. Army Electronics Command
- Titov, D. V., Markiewicz, W. J., 2006, Technical Note: Anomalous features in the VMC images, VMC-MPAE-TN-SS010-001, pp. 1–31
- Titov, D. V., Svedhem, H., Koschny, D., Hoofs, R., Barabash, S., Bertaux, J.-L., Drossart, P., Formisano, V., Häusler, B., Korablev, O., Markiewicz, W. J., Nevejans, D., Pätzold, M., Piccioni, G., Zhang, T. L., Merritt, D., Witasse, O., Zender, J., Accomazzo, A., Sweeney, M., Trillard, D., Janvier, M., Clochet, A., 2006, Venus Express science planning, *Planetary and Space Science*, 54, 1279–1297
- Toigo, A., Gierasch, P. J., Smith, M. D., 1994, High resolution cloud feature tracking on Venus by Galileo, *Icarus*, 109, 318–336
- Travis, L. D., Coffeen, D. L., del Genio, A. D., Hansen, J. E., Kawabata, K., Lacis, A. A., Lane, W. A., Limaye, S. S., Rossow, W. B., Stone, P. H., 1979, Cloud images from the Pioneer Venus Orbiter, *Science*, 205, 74–76
- Vio, R., Strohmer, T., Wamsteker, W., 2000, On the Reconstruction of Irregularly Sampled Time Series, *Publications of the Astronomical Society of the Pacific*, 112, 74–90
- Weh, L., 2005, Surface Structures in Thin Polymer Layers Caused by Coupling of Diffusion-Controlled Marangoni Instability and Local Horizontal Temperature Gradient, *Macromolecular Materials and Engineering*, 290, 976–986
- Widemann, T., Lellouch, E., Luz, D., Moreno, R., 2006, Dynamical Structure of Venus' Middle Atmosphere Constrained by Direct Wind Measurements, in *Bulletin of the American Astronomical Society*, vol. 38 of *Bulletin of the American Astronomical Society*, pp. 515–+
- Wright, W. H., 1927, Photographs of Venus made by Infra-red and by Violet Light, *Publ. Astron. Soc. Pacific*, 39, 220–221
- Zasova, L. V., Ignatiev, N., Khatuntsev, I., Linkin, V., 2007, Structure of the Venus atmosphere, *Planetary and Space Science*, 55, 1712–1728
- Zhang, T. L., Baumjohann, W., Delva, M., Auster, H.-U., Balogh, A., Russell, C. T., Barabash, S., Balikhin, M., Berghofer, G., Biernat, H. K., Lammer, H., Lichtenegger, H., Magnes, W., Nakamura, R., Penz, T., Schwingenschuh, K., Vörös, Z., Zambelli, W., Fornacon, K.-H., Glassmeier, K.-H., Richter, I., Carr, C., Kudela, K., Shi, J. K., Zhao, H., Motschmann, U., Lebreton, J.-P., 2006, Magnetic field investigation of the Venus plasma environment: Expected new results from Venus Express, *Planetary and Space Science*, 54, 1336–1343

Publications

Refereed contributions

Markiewicz, W. J., Titov, D. V., Ignatiev, N., Keller, H.-U., Crisp, D., Limaye, S. S., Jaumann, R., **Moissl, R.**, Thomas, N., Esposito, L., Watanabe, S., Fiethe, B., Behnke, T., Szemerey, I., Michalik, H., Perplies, H., Wedemeier, M., Sebastian, I., Boogaerts, W., Hviid, S. F., Dierker, C., Osterloh, B., Böker, W., Koch, M., Michaelis, H., Belyaev, D., Dannenberg, A., Tschimmel, M., Russo, P., Roatsch, T. and Matz, K. D., *Venus Monitoring Camera for Venus Express*, Plan. Space Sci., Vol. 55, Iss. 12, 1701–1711, 2007

Markiewicz, W. J., Titov, D. V., Limaye, S. S., Keller, H.-U., Ignatiev, N., Jaumann, R., Thomas, N., Michalik, H., **Moissl, R.** and Russo, P., *Morphology and dynamics of the upper cloud layer of Venus*, Nature, Vol. 450. Iss. 7170, 633–636, 2007

Moissl, R., Khatuntsev, I., Limaye, S. S., Titov, D. V., Markiewicz, W. J., Ignatiev, N. I., Roatsch, T., Matz, K.-D., Jaumann, R., Almeida, M., Portyankina, G. and Behnke, T., *Cloud top winds from tracking UV features in VMC images*, Jour. Geophys. Res, *submitted*

Posters and Presentations

Moissl, R., Khatuntsev, I. and Limaye S. S., *Wind measurements in the middle atmosphere of Venus and their interpretation*, Venus Express Science Workshop, La Thuile, Italy, March 2–8 2008. (Oral)

Moissl, R., Markiewicz, W. J., and D. V. Titov, *The upper cloud deck of Venus as seen by VMC*, Venus Express Science Workshop, La Thuile, Italy, March 2–8 2008. (Oral)

Moissl, R., Markiewicz, W. J., Titov, D. V., Limaye, S. S., Russo, P., Keller, H.-U. and Ignatiev, N. I., *First cloud-tracked winds from the Venus Express VMC images*, European Geosciences Union general Assembly, Vienna, Austria April 15–20, 2007. (Poster)

Moissl, R., Markiewicz, W. J. and D. V. Titov, *Cloud-tracked winds from VMC Images*, Venus Express Science Workshop, La Thuile, Italy, March 18–24 2007. (Oral)

Markiewicz, W. J., Titov, D. V., Ignatiev, N., Keller, H.-U., Crisp, D., Esposito, L., Jaumann, R., Limaye, S. S., Michalik, H., Thomas, N., Watanabe, S., **Moissl, R.**, Hviid, S. and Russo, P., *First Results from Venus Monitoring Camera on Venus Express*, American Astronomical Society, DPS meeting #38, Pasadena (USA), Bulletin of the American Astronomical Society, Vol. 38, p.511, September 2006 (Oral, in proxy for first author)

Moissl, R., Markiewicz, W. J., Titov, D. V., Russo, P. and Keller, H.-U., *Observations of global dynamics in the Venus upper cloud deck by the Venus Monitoring Camera*, European Planetary Science Congress 2006. Berlin, Germany, 18–22 September 2006., p.240 (Oral)

Moissl, R., Markiewicz, W. J., Titov, D. V., Russo, P., Keller, H.-U., Ignatiev, N. I. and Limaye, S. S., *Observations of the global dynamics in the Venus upper cloud deck by the Venus Monitoring Camera onboard Venus Express*, European Planetary Science Congress 2006. Berlin, Germany, 18–22 September 2006., p.634 (Poster)

Acknowledgements

During the three years of the work for this thesis there have been a lot of people who have helped to make this time more than just a period of research in my life, but rather an unforgettable experience in many respects.

First of all I would like to thank my supervisors and colleagues who introduced me to the wonders of the “Planet of Storms” and stood by my side with lifetimes of experience on the mysteries of the Venus atmosphere. Thank you Dima and Wojtek for providing me with lots of advice and being available for my questions, even in times when each of you was busy with about as much workload as one person can possibly have time to handle. And thank you also a lot for making a childhood dream come true and let me travel to the launch of the Venus Express mission from the Bajkonur Cosmodrome! I will never forget the day when that rocket thundered off to the sky and beyond. Thank you Sanjay for your always productive and helpful counsel (even over nearly half a planet of distance), your invitations to Madison and all the extra hours at work you spent with me for the cloud tracking. I really enjoyed my visits to Madison and wished I could have spent more time working there. Further I want to thank my esteemed colleague Dr. Igor Khatuntsev for sharing his wind tracking results with me, collected in countless hours of work.

This work would not have been possible without the great support from all the other VMC team members who each contributed to the success of the instrument and the overcoming of lots of difficulties. The colleagues at IDA in Braunschweig and DLR in Berlin are doing a wonderful job in collecting and archiving the huge amounts of data produced by VMC and maintaining the instrument. I feel honored to work with all of you who make the team work! And I am sure I would have drowned in the tedious tasks of planning and implementing the observation sequences, were it not for Anya and Miguel and Wojtek.

Thanks also go to all the people at the MPS who provided the necessary framework and environment needed to do any research in general, and realize a dissertation in particular. I cannot imagine what the International Max Planck Research School for the Solar System and Beyond would be without Dr. Dieter Schmitt who does a great job as the school’s supervisor and is always there to help us students not only with formalities but also on a personal level and with lots of patience and understanding.

Those three years would have been far less enjoyable without all the nice people that have accompanied me as fellow students and friends. I always enjoyed the interesting and funny conversations among the “italian coffee group” after lunch, those espressi really helped me staying awake and motivated during long hours of work. Thank you guys! I will never forget all the nice game evenings with Anya, Michael, Cleme, Luca, Sanja, Manuela and Maya!

Thank you, Cleme and Gennaro and Anya and Michael that you have shared that very special moment in your life with Lena and me, your weddings will always be treasured

memories when I look back at the time in Lindau. Thank you also Dennis, Luca and Sanja for always having an open ear for my blathering about everything and nothing. Martin, thanks a lot for not destroying the VMC during the calibrations, guiding me through the urban jungle of Moscow and many entertaining and enlightening conversations.

It would never have been possible to even start with a Ph.D. thesis, were it not for all the support I have received from my friends and family during my whole life. Especially my parents who have given lots of sacrifices to help me follow my dreams. I simply cannot thank you all enough for all you have done for me in all those years and for being there at all.

A very special thanks goes to my wife Anna-Lena. I am deeply grateful that you decided to spend a lifetime with me. Kei te aroha au i a koe!

I dedicate this thesis to the memory of Dr. Gerhard Knissel, who taught me (and many others) that physics and mathematics can be exciting after all.

Curriculum Vitae

Name: Richard Moissl
Geburtsdatum: 14. August 1977
Geburtsort: Grünstadt, Deutschland
Staatsangehörigkeit: deutsch

Schulische Ausbildung

1984–1988 Dekan Ernst Grundschule, Grünstadt
1988–1997 Leininger Gymnasium, Grünstadt, Abschluss: Abitur

Studium

1997–2005 Diplom in Physik, Ruprecht-Karls-Universität Heidelberg
2001–2002 Austauschstudium im Rahmen des ERASMUS Programms
Università di Roma “La Sapienza”, Italien

Berufserfahrung

1999–2004 Studentische Hilfskraft zur Auswertung von Daten des DDS Instruments
an Bord der NASA Raumsonde Galileo
Max-Planck-Institut für Kernphysik, Heidelberg
2004–2005 Hilfsoperateur am Heidelberg High Current Injector (HCI) Beschleuniger
Max-Planck-Institut für Kernphysik, Heidelberg